Dynamic Braking Control for Accurate Train Braking Distance Estimation under Different Operating Conditions

Husain Abdulrahman Ahmad

Dissertation submitted to the faculty of the Virginia Polytechnic Institute and State University in partial fulfillment of the requirements for the degree
of
Doctor of Philosophy
In
Mechanical Engineering

Mehdi Ahmadian (Chair)
Muhammad R. Hajj
Daniel J. Inman
Corina Sandu
Saied Taheri

February 20, 2013
Blacksburg, VA, USA

Keywords: Dynamic Braking, Traction Motors, Wheel/Rail Adhesion, Train Braking Distance, Longitudinal Train Dynamics, Model Reference Adaptive Control, Creep, Kalker's Theory.

Dynamic Braking Control for Accurate Train Braking Distance Estimation under Different Operating Conditions

Husain Abdulrahman Ahmad

ABSTRACT

The application of Model Reference Adaptive Control (MRAC) for train dynamic braking is investigated in order to control dynamic braking forces while remaining within the allowable adhesion and coupler forces. This control method can accurately determine the train braking distance. One of the critical factors in Positive Train Control (PTC) is accurately estimating train braking distance under different operating conditions. Accurate estimation of the braking distance will allow trains to be spaced closer together, with reasonable confidence that they will stop without causing a collision. This study develops a dynamic model of a train consist based on a multibody formulation of railcars, trucks (bogies), and suspensions. The study includes the derivation of the mathematical model and the results of a numerical study in Matlab. A three-railcar model is used for performing a parametric study to evaluate how various elements will affect the train stopping distance from an initial speed. Parameters that can be varied in the model include initial train speed, railcar weight, wheel-rail interface condition, and dynamic braking force. Other parameters included in the model are aerodynamic drag forces and air brake forces.

An MRAC system is developed to control the amount of current through traction motors under various wheel/rail adhesion conditions while braking. Minimizing the braking distance of a train requires the dynamic braking forces to be maximized within the available wheel/rail adhesion. Excessively large dynamic braking can cause wheel lockup that can damage the wheels and rail. Excessive braking forces can also cause large buff loads at the couplers. For DC traction motors, an MRAC system is used to control the current supplied to the traction motors. This motor current is directly proportional to the dynamic braking force. In addition, the MRAC system is also used to control the train speed by controlling the synchronous speed of the AC traction motors. The goal of both control systems for DC and AC traction motors is to apply maximum available dynamic braking while avoiding wheel lockup and high coupler forces. The results of the study indicate that the MRAC system significantly improves braking distance while maintaining better wheel/rail adhesion and coupler dynamics during braking. Furthermore, according to this study, the braking distance can be accurately estimated when MRAC is used. The robustness of the MRAC system with respect to different parameters is investigated, and the results show an acceptable robust response behavior.

Acknowledgements

In the Name of Allah, the Most Beneficent, the Most Merciful. All thanks and praise to Allah, the Lord of the worlds. Prayers and peace be upon His prophet Mohammed, the last prophet and messenger of Allah.

First of all, I thank Allah for giving me health, support, guidance, knowledge, and strength to complete this study. I would like to express my gratitude to my wonderful wife and children for their constant love, patience, and support to complete my PhD dissertation. I would also like to express my gratitude towards my parents for encouraging me and praying for me all my life.

I would like to express my sincere gratitude to the Saudi Ministry of Higher Education for granting me a fully-funded scholarship to complete my Ph.D. degree.

I would like to express my sincere appreciation to my committee chair, Dr. Mehdi Ahmadian, for all his support, advice, help, and guidance. I would not have accomplished my work without his vision and encouragement.

I would also like to thank Dr. Corina Sandu, Dr. Saied Taheri, Dr. Muhammad Hajj, and Dr. Daniel Inman for serving on my committee.

Contents

List of Tables

List of Figures

Nomenclature

ω_{ws}	wheelset rotational speed (rad/sec)
ω_r	rotor rotational speed (rad/sec)
ω_s	motor synchronous speed (rad/sec)
ω_e	electrical excitation speed of AC traction motor (rad/sec)
f_e	electrical excitation frequency of AC traction motor (Hz)
F_{cp}	coupler force (N)
F_{cr}	creep force (N)
F_{fb}	front bogie horizontal suspension force (N)
R_{fb}	front bogie vertical suspension force (N)
F_{rb}	rear bogie horizontal suspension force (N)
R_{rb}	rear bogie vertical suspension force (N)
F_{ws}	wheelset horizontal suspension force (N)
R_{ws}	wheelset vertical suspension force (N)
F_{crv}	curve resistance (N/tonnes)
R_{crv}	track radius of curvature (m)
M_{rr}	rolling resistance moment (N.m)
k_s	secondary suspension stiffness (N/m)
C_s	secondary suspension damping (N.s/m)
k_{ps}	primary suspension stiffness (N/m)
C_{ps}	primary suspension damping (N.s/m)
k_{cp}	coupler stiffness (N/m)
C_{cp}	coupler damping (N.s/m)
sk	coupler slack length (m)
m_i	carbody mass (kg)

m_b bogie mass (kg)

m_{ws} wheelset mass (kg)

I_i mass inertia of the carbody (kg.m^2)

I_b mass inertia of the bogie (kg.m^2)

I_{ws} mass inertia of the wheelset (kg.m^2)

x_i horizontal position of the carbody (m)

x_b horizontal position of the bogie (m)

x_{ws} horizontal position of the wheelset (m)

z_i vertical position of the carbody (m)

z_b vertical position of the bogie (m)

V_{ws} actual forward speed of the wheelset (m/s)

Rr propulsion resistance (N/tonne)

R_{rr} rolling resistance (N/tonne)

R_{drag} aerodynamic drag resistance (N/tonne)

F_{rr} rolling resistance force (N)

F_{drag} aerodynamic drag (N)

W total weight of the car in (tons or tonnes)

A cross sectional area of the car (f^2 or m^2)

n number of axles

$\dot{x}$ train speed (miles/hr or m/s)

ξ_x longitudinal creepage

ξ_y lateral creepage

ξ_{sp} spin creepage

a, b semi-axes of the wheel-rail contact ellipse (m)

E_w Young's modulus of elasticity of the wheel (N/m^2)

E_r Young's modulus of elasticity of the rail (N/m^2)

ν_w Poisson's ratio for the wheel

ν_r	Poisson's ratio for the rail
R_1^w	principal rolling radius of the wheel (m)
R_2^w	transverse radius of curvature of the wheel profile at the contact point (m)
R_1^r	principal rolling radius of the rail (m)
R_2^r	transverse radius of curvature of the rail profile at the contact point (m)
G	shear modulus of rigidity (N/m^2)
μ	coefficient of adhesion
N	wheel normal load (N)
τ_{db}	dynamic braking torque (N.m)
τ_{ab}	air braking torque (N.m)
i	DC motor current (Amps)
k_t	DC motor constant (N.m/Amps)
s	AC motor speed slip ratio
u_c	reference input
y_m	reference model output
y_p	system output
γ	adaptation gain
J	cost function
φ	control parameter
e	error between reference model output and system output
S_T	torque-creep ratio (N.m)
N/S_T	normal-load-torque-creep ratio (m^{-1})
$\frac{F_{cr}}{\mu N}$	normalized creep force
C_{11}	Kalker's creep coefficient
ξ	normalized longitudinal creep
η	normalized lateral creep
ϕ	Kalker's normalized longitudinal coefficient

ψ_1	Kalker's normalized lateral coefficient
e_b	back emf generated at the armature (volt)
k_e	back emf constant (volt.sec/rad)
R_a	armature resistance (Ω)
L_a	armature inductance (H)
P_{max}	maximum power provided by AC traction motor at wheelset (Watt)
h_1	vertical distance between carbody center of gravity and center of secondary suspension (m)
h_2	vertical distance between bogie center of gravity and center of secondary suspension (m)
h_3	vertical distance between bogie center of gravity and center of primary suspension (m)
h_4	vertical distance between carbody center of gravity and coupler position (m)
l_1	horizontal distance between centers of gravity of carbody and bogie (m)
l_2	horizontal distance between centers of gravity of bogie and wheelset (m)
C	aerodynamic drag coefficient

Chapter 1

Introduction

1.1 Overview

Railway vehicle systems have been gaining more interest over the past few decades. However, the study of the dynamics of railway vehicles is complicated, and it can be conducted from different points of view depending on the research interest. Railway vehicle braking is one of the most critical subjects that contributes to human safety, equipment design and cost effectiveness. There are numerous research projects that are related to train braking. The study of railway vehicle braking is important to investigate in-train forces, ride comfort, safe operation, braking distance and time, and vehicle speed. Modeling the longitudinal dynamics of trains is important to understand the behavior of rail vehicles while in operation. This can also help with better understanding the effects of braking forces and other forces and moments that resist the forward motion of the train. Improving dynamic braking forces results in shorter train stopping distance.

Train speed control and train braking distance estimation are required to prevent train-to-train accidents. This is one of the most important reasons for applying positive train control (PTC) technology to the railway network. PTC is a GPS-based technology that is designed to prevent train collisions and derailments, and to control train movements along the track. PTC systems were being voluntarily installed by some companies prior to October 2008. A recent act by Congress, called the Rail Safety Improvement Act of 2008 (RSIA), mandates the implementation of such systems. This act includes the widespread installation of PTC systems by December 2015 [9, 26]. The U.S. railroads are currently working on PTC system development, and some are adapting their individual PTC systems to increase interoperability [9]. PTC requires understanding the longitudinal train dynamics while operating on the railway network. Modeling and investigating the longitudinal train dynamics and the train motion resistance are some of the key factors for successfully implementing PTC.

1.2 Objectives

The primary objectives of this research are

1. to model longitudinal train dynamics using multibody dynamics formulation, including train braking dynamics;
2. to perform a parametric study to better understand how various elements affect the train braking distance;
3. to use the train model for closed-loop control of the dynamic braking forces by controlling DC traction motor current; and
4. to use the train model for closed-loop control of the dynamic braking forces by controlling the synchronous speed of the AC traction motor.

1.3 Research Approach

The approach of this research is described as follows. First, a two-dimensional train model is developed using multibody dynamics formulation. The model includes all forces and moments that resist the train motion, beyond braking forces, and the general equations of motion are applied to each railcar within the train. The model is then verified by comparing the simulation results with a model developed in SIMPACK, which is a toolbox that can be used to perform a multibody simulations. Next, a parametric study is performed to investigate the train braking distance under different operating conditions. For each operating condition, the train braking distance and time needed to stop the train are estimated. The dynamic model is used to develop a closed-loop control of the dynamic braking forces. The Model Reference Adaptive Control method is used to enable adapting the dynamic braking forces for minimizing the braking distance. The MRAC method actually adjusts the current supplied to the DC traction motors which directly adjusts the dynamic braking force. Then the same control method is used to control the dynamic braking force by controlling the synchronous frequency of the AC traction motor.

1.4 Main Contribution

This research focuses on the application of MRAC for better controlling wheel-rail interface dynamics and longitudinal train forces in order to bring a moving train to stop without exceeding the maximum wheel longitudinal creep forces or the allowable inter-train dynamics.

The main contributions of this study are:

1. to provide an extensive study of MRAC for controlling longitudinal train dynamics;
2. to develop a first study of its kind (to the best of our knowledge) of a relationship between creep forces, creepages, and the braking torque for different weights of the locomotive using the longitudinal train dynamic model; and
3. to extensively study the interaction between dynamic braking control and dynamic braking provided by the traction motors.

1.5 Document Outline

The document is organized as follows. Chapter 2 presents a background of wheel/rail mechanics and adhesion dynamics, train motion resistances, and train braking, as well as a brief background about Model Reference Adaptive Control method. It also includes a literature survey of past studies related to longitudinal train dynamics and train braking control. In Chapter 3, a model that represents the longitudinal train dynamics is developed, and the equations of motion are written for each railcar within the train. Chapter 4 presents the simulation results of the developed dynamic model, including a parametric study on the effects of different parameters on the train braking distance. Chapters 5 and 6 present the use of the Model Reference Adaptive System developed to control the dynamic braking forces using DC and AC traction motors, respectively.

Chapter 2

Background

2.1 Introduction

Modeling of railway vehicle dynamics is a complicated problem in engineering and research, and it depends on the research goals and the objective of the study. For instance, if ride comfort is the main objective of the research, then mechanical components that cause vibrations should be studied. Also, if the bogie and wheelset design needs improvement, detailed modeling of these components will be needed. In this study, the longitudinal train dynamics will be studied to estimate and minimize the braking distance of the train. Because studying the braking forces, the coupler forces, and the braking distance is our main objective, only train motion along the track is considered. All motion resistances, wheel/rail mechanics, and railway vehicle components that are needed to study the longitudinal train dynamics will be discussed in this chapter, along with wheel/rail mechanics that include creepages and creep forces. All forces that affect the longitudinal train dynamics will be included in our discussions, including coupler forces, braking forces, propulsion resistance, grade resistance, and curving resistance. Additionally, this chapter includes a review of a Model Reference Adaptive Control method that will be used to control train braking. Finally, a review of past research related to longitudinal train dynamics will be presented.

2.2 Wheel/Rail Mechanics

The interaction forces between the wheel and the rail have a significant effect on the dynamic behavior of the railway vehicle. Adhesion, creep, and wear can significantly affect the railway vehicle dynamics. The adhesion depends on the surface roughness and environmental conditions. Creep forces depend on the dimensions of the wheel and the rail profile, as well as the materials of the wheel and the rail. In order to calculate the creep forces, wheel/rail contact mechanics must be studied. When two bodies are rolled over each other while pressing against each other, the contact area is elliptical in shape, with semiaxes (a, b), as proven by Hertz's static theory. The semiaxes (a, b) depend on the geometry and the materials of the two bodies [1].

In addition, when the two bodies do not have the exact same velocities, the term *creepage* or *creep* is used to define the difference ratio. Two creepages are defined: the longitudinal creepage (ξ_x), and the lateral creepage (ξ_y). Another term, *spin creepage* ξ_{sp}, is also defined as the two bodies rotate about an axis perpendicular to the contact area [2]. For a wheel and rail, the terms are defined as:

$$\begin{aligned}\xi_x &= \frac{actual\ forward\ wheel\ speed - pure\ rolling\ forward\ wheel\ speed}{pure\ rolling\ forward\ wheel\ speed} \\ \xi_y &= \frac{actual\ lateral\ wheel\ speed - pure\ rolling\ lateral\ wheel\ speed}{pure\ rolling\ forward\ wheel\ speed} \\ \xi_{sp} &= \frac{angular\ speed\ of\ the\ wheel - angular\ speed\ of\ the\ rail}{pure\ rolling\ forward\ wheel\ speed}\end{aligned} \tag{2.1}$$

Figure 2.1 shows a sketch of the creep, creep forces, and creep moments. Since the wheel and rail are elastic bodies, the contact ellipse has a slip region and adhesion region. Sliding occurs when the contact ellipse entirely becomes a slip region. In other words, when there is not enough adhesion between the two bodies, they will slip with respect to each other [2].

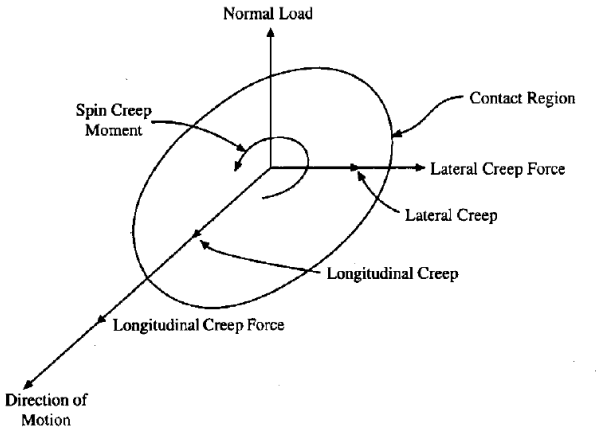

Figure 2.1 Creep forces and moments [2].

2.2.1 Wheel/Rail Contact Ellipse

The semiaxes (*a, b*) of the contact ellipse depend on the geometry of the wheel and the rail profile. According to Hertz's theory [1], the semiaxes can be calculated as

$$a = m\left[\frac{3\pi N(K_1 + K_2)}{4K_3}\right]^{1/3}$$
$$b = n\left[\frac{3\pi N(K_1 + K_2)}{4K_3}\right]^{1/3} \tag{2.2}$$

where N is the normal load at the wheel/rail contact. K_1, K_2 and K_3 are defined as

$$K_1 = \frac{1 - \nu_w^2}{\pi E_w}\ , \quad K_2 = \frac{1 - \nu_r^2}{\pi E_r}$$
$$K_3 = \frac{1}{2}\left[\frac{1}{R_1^w} + \frac{1}{R_2^w} + \frac{1}{R_1^r} + \frac{1}{R_2^r}\right] \tag{2.3}$$

where

E_w, E_r = Young's modulus of elasticity of the wheel and the rail, respectively (N/m^2)

ν_w, ν_r = Poisson's ratio for the wheel and the rail, respectively

R_1^w = principal rolling radius of the wheel (m)

R_2^w = transverse radius of curvature of the wheel profile at the contact point (m)

R_1^r = principal rolling radius of the rail (m)

R_2^r = transverse radius of curvature of the rail profile at the contact point (m)

These radii are shown in Figure 2.2. K_4 is defined as

$$K_4 = \frac{1}{2}\left[\left(\frac{1}{R_1^w} + \frac{1}{R_2^w}\right)^2 + \left(\frac{1}{R_1^r} + \frac{1}{R_2^r}\right)^2 + 2\left(\frac{1}{R_1^w} - \frac{1}{R_2^w}\right)\left(\frac{1}{R_1^r} - \frac{1}{R_2^r}\right)\cos 2\psi\right]^{1/2} \tag{2.4}$$

where ψ is the angle between the normal planes that contain $\frac{1}{R_1^w}$ and $\frac{1}{R_1^r}$. Coefficients m and n depend on the ratio K_4/K_3. They are functions of θ and can be determined from Table 2.1. θ can be defined as

$$\theta = \cos^{-1}(K_4/K_3) \tag{2.5}$$

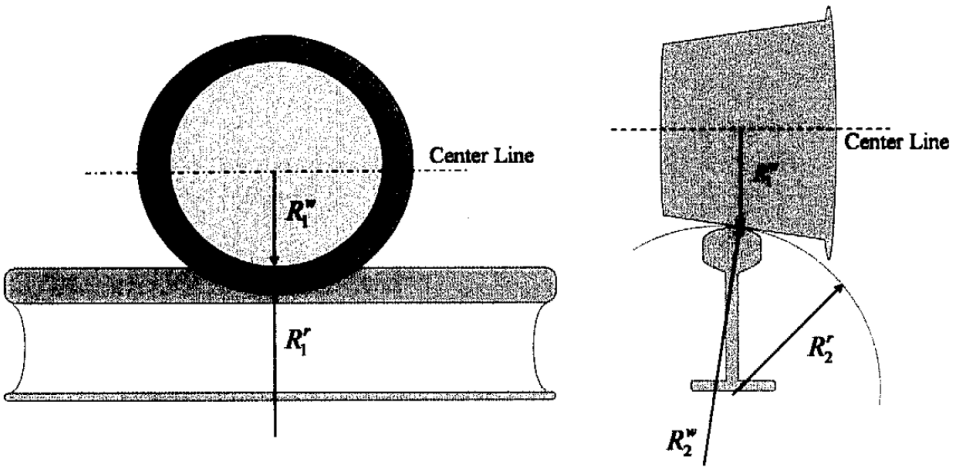

Figure 2.2 Principal radii of curvature for wheel and rail [3].

Table 2.1 Coefficients *m* and *n* for different values of θ [1].

θ(deg)	*m*	*n*	θ(deg)	*m*	*n*	θ(deg)	*m*	*n*
0.5	61.4	0.1018	10	6.604	0.3112	60	1.486	0.717
1.5	36.89	0.1314	20	3.813	0.4123	65	1.378	0.759
2	27.48	0.1522	30	2.731	0.493	70	1.284	0.802
3	22.26	0.1691	35	2.397	0.530	75	1.202	0.846
4	16.5	0.1964	40	2.136	0.567	80	1.128	0.893
6	13.31	0.2188	45	1.926	0.604	85	1.061	0.944
7	9.79	0.2552	50	1.754	0.641	90	1.000	1.000
8	7.86	0.285	55	1.611	0.678			

Because the wheel and rail are made out of steel, the Poisson's ratio and Young's modulus of elasticity are the same for both. For this study, it is assumed that the wheel profile is conical and the track is tangent, thus both R_2^w and R_1^r become ∞. Only longitudinal train dynamics is considered in the dynamic model. This means that it is reasonable to assume that $\psi = 0$. By using these assumptions, Equations (2.3) are reduced to:

$$K_1 = K_2 = \frac{1-\nu}{\pi E}$$
$$K_3 = \frac{1}{2}\left[\frac{1}{R_1^w} + \frac{1}{R_2^r}\right] \tag{2.6}$$

$$K_4 = \frac{1}{2}\left[\left(\frac{1}{R_1^w}\right)^2 + \left(\frac{1}{R_2^r}\right)^2 - 2\left(\frac{1}{R_1^w}\right)\left(\frac{1}{R_2^r}\right)\right]^{1/2} \tag{2.7}$$

2.2.2 Creep Forces

There are various rolling contact theories in the literature that calculate longitudinal and lateral creep forces at the wheel/rail interface. Some of the more useful theories are Kalker's linear theory, Kalker's empirical theory, Johnson and Vermeulen's model, and the Heuristic nonlinear model [2]. Kalker's theories are often used for rail dynamics studies. Johnson and Vermeulen's theory is less accurate but has greater simplicity [1]. Kalker has two main theories: Kalker's empirical theory and Kalker's linear theory. Kalker's empirical theory will be adopted in the study and will be explained later in this section. Kalker's linear theory is used to calculate the creep force and is mostly applicable for small creepages. For the longitudinal direction of a train model, Kalker's creep coefficient can be defined as

$$f_x = (ab)G\ C_{11} \tag{2.8}$$

where G is the shear modulus of rigidity, and C_{11} is the creepage coefficient that is dependent on Poisson's ratio and the ratio (a/b), as shown in Table 2.2. The longitudinal creep force can be caculated as

$$F_{cr} = f_x \xi_x \tag{2.9}$$

Table 2.2 Kalker creepage coefficient C_{11} for different *b/a* ratios and Poisson's ratios [1].

C_{11}		
g = b/a	*ν = 1/4*	*ν = 1/2*
1.0	4.12	5.20
0.9	4.22	5.30
0.8	4.36	5.42
0.7	4.54	5.58
0.6	4.78	5.80
0.5	5.10	6.11
0.4	5.57	6.57
0.3	6.34	7.34
0.2	7.78	8.82
0.1	11.7	12.9

Kalker's empirical formula gives the value of the normalized creep force as

$$\frac{|F_{cr}|}{\mu N} = \begin{cases} f_1(\tau)\boldsymbol{e_1} + f_2(\tau)\boldsymbol{e_2} & \tau \le 1 \\ \boldsymbol{e_2} & \tau > 1 \end{cases} \tag{2.10}$$

where

$$\begin{aligned} &f_1(\tau) = \tfrac{3}{2}\tau\, cos^{-1}\tau\ , \\ &f_2(\tau) = 1 - \left(1 + \tfrac{1}{2}\tau^2\right)\sqrt{1-\tau^2}\ , \\ &\boldsymbol{e_1} = (\xi \boldsymbol{i} + \eta \boldsymbol{j})/\tau\ \boldsymbol{,} \\ &\boldsymbol{e_2} = \left(\xi_x \boldsymbol{i} + \xi_y \boldsymbol{j}\right)/\sqrt{\xi_x^2 + \xi_y^2}\ \boldsymbol{,} \\ &\boldsymbol{i, j} = \text{unit vector in the } x \text{ and y directions, respectively,} \\ &\xi\ \ = \tfrac{\pi abG\xi_x}{3\mu N\phi}\ , \\ &\eta = \tfrac{\pi abG\xi_y}{3\mu N\psi_1}\ , \\ &\tau = \sqrt{\xi^2 + \eta^2}, \end{aligned} \tag{2.11}$$

G is the shear modulus of rigidity (N/m^2), ϕ and ψ_1 are Kalker's normalized longitudinal and lateral coefficients, respectively, which are dependent on Poisson's ratio and the ratio (a/b), N is the normal load, and μ is the wheel/rail adhesion coefficient. Table 2.3 shows the values of the coefficients ϕ and ψ_1 as functions of the ratio *a/b* and Poisson's ratio, ν. Figure 2.3 shows the normalized creep force versus τ. In this figure, Johnson and Vermeulen's experiments are compared with Kalker's empirical theory and show very close results.

Table 2.3 Normalized longitudinal and lateral Kalker's coefficients [1].

	$\phi = \psi_1$	ϕ		ψ_1	
	$\sigma = 0$	$\sigma = \frac{1}{4}$	$\sigma = \frac{1}{2}$	$\sigma = \frac{1}{4}$	$\sigma = \frac{1}{2}$
(a/b)					
0.2	0.9686	0.7377	0.5068	0.9574	0.9461
0.4	0.9205	0.7151	0.5096	0.8958	0.8711
0.6	0.8719	0.6893	0.5066	0.8366	0.8012
0.8	0.8267	0.6633	0.5000	0.7834	0.7401
1.0	0.7854	0.6381	0.4908	0.7363	0.6872
(b/a)					
0.2	0.4095	0.3633	0.3171	0.3533	0.2971
0.4	0.5755	0.4933	0.4112	0.5138	0.4521
0.6	0.6740	0.5645	0.4549	0.6151	0.5562
0.8	0.7393	0.6086	0.4779	0.6852	0.6301
1.0	$\pi/4$	$(4 - 3\sigma)\pi/16$		$(4 - \sigma)\pi/16$	

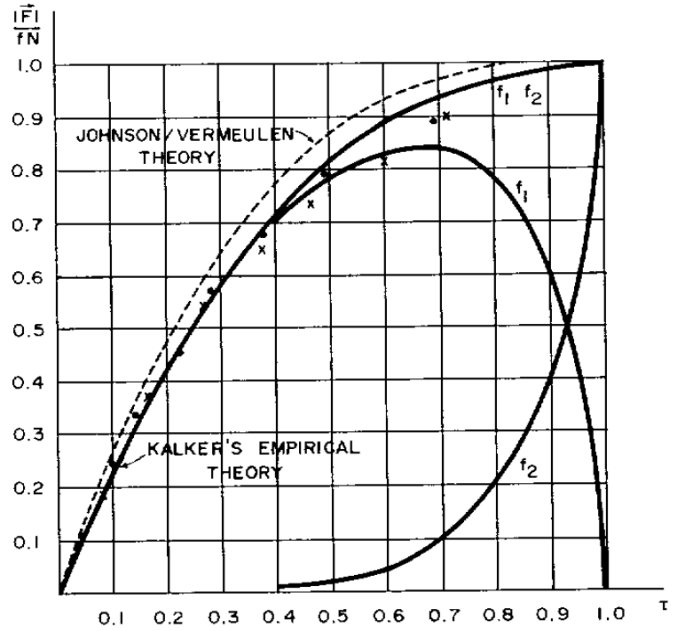

Figure 2.3 Kalker's empirical theory [1].

In the case of a two-dimensional analysis, vertical and longitudinal directions are considered. This means that lateral direction is neglected. Since only the longitudinal creep force will be

calculated, Kalker's empirical theory can be simplified. This simplification will give the same results as previously shown in Figure 2.3. The simplified expressions are

$$
\begin{aligned}
&f_1(\tau) = \frac{3}{2}\tau\, cos^{-1}\tau\,, \\
&f_2(\tau) = 1 - \left(1 + \frac{1}{2}\tau^2\right)\sqrt{1-\tau^2}\,, \\
&\boldsymbol{e_1 = i}\,, \\
&\boldsymbol{e_2 = i}\,, \\
&\tau = \xi = \frac{\pi abG\xi_x}{3\mu N\phi} \text{ since } \eta = \xi_y = 0.
\end{aligned}
\tag{2.12}
$$

2.2.3 Wheel/Rail Adhesion Coefficient

The wheel/rail adhesion coefficient is affected by various factors, which include (but are not limited to) speed, wheel and rail wear, rail surface condition, and track irregularities. The most significant factor is surface contamination by oil, water, and dirt. Wheel speed is also a critical factor [2]. Figure 2.4 shows an example of the adhesion coefficient as a function of train speed for different wheel/rail conditions. Figure 2.5 shows a comparison of true and average adhesion coefficients as a function of speed for EMD's SD-45 locomotive.

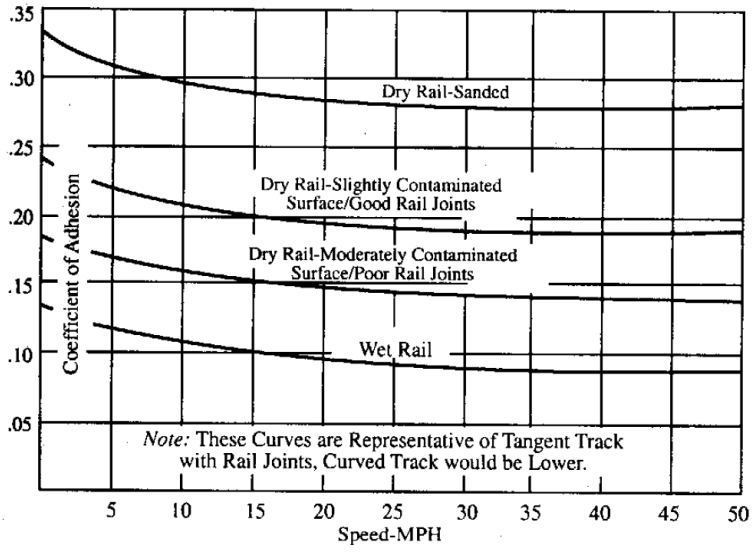

Figure 2.4 Adhesion coefficient versus speed for different wheel/rail conditions [2].

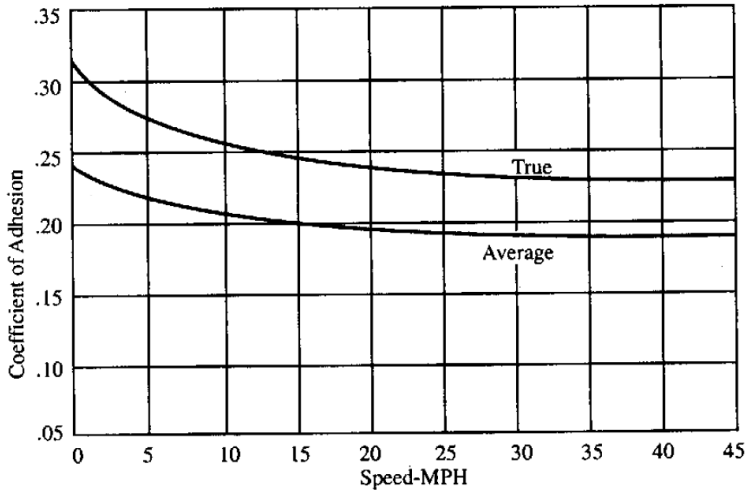

Figure 2.5 Adhesion coefficient versus speed for EMD's SD-45 locomotive [2].

2.2.4 Wheel Lockup

Wheel lockup is also known as wheel skid. Wheel lock-up can damage the wheelset and the rail. The normalized creep force can determine whether wheel lockup occurs or not. The normalized creep force is calculated as the creep force divided by the wheel normal (vertical) load. The conditions that identify wheel lockup can be written as

$$\begin{aligned} &\frac{F_{cr}}{\mu N} \geq 1 \quad \text{wheel lock-up} \\ &\frac{F_{cr}}{\mu N} < 1 \quad \text{wheel rolling condition} \end{aligned} \tag{2.13}$$

where N is the normal force (N) and μ is the wheel/rail adhesion coefficient [1, 10].

2.3 Longitudinal Train Dynamics

When longitudinal train dynamics are studied, the motion of the rolling stock along the track is considered. The study of longitudinal train dynamics includes the train motion as a whole and any relative motions between the railcars [4]. When the railcars are subjected to compressive forces, they are in the *buff load* condition. In contrast, when they are subjected to tensile forces, they are in the *draft load* condition [1]. Longitudinal train dynamics are important in investigating ride comfort, rolling stock design, coupler design, and braking control design [4].

In addition, a longitudinal dynamic model is able to study coupler forces, speed, distance, and time relationships [1]. Forces that are considered in the longitudinal direction include dynamic braking at the locomotives, train air braking, rolling resistance, aerodynamic drag, curve resistance, and grade resistance. Next, a brief background on coupler components will be covered. All forces that are included in longitudinal train dynamics will also be briefly discussed.

2.3.1 Coupling Components

2.3.1.1 Coupler

The coupler is a component that connects two railcars together. Several coupler designs are available in the industry. In Figure 2.6, a typical coupler is shown. The couplers between railcars have clearances, and the summations of these clearances are called *coupler slack*. The coupler slack is important to help the locomotives start to pull the train, and it develops compressive forces during braking. If the braking is applied excessively, it can lead to broken couplers, and consequently, train derailment [1].

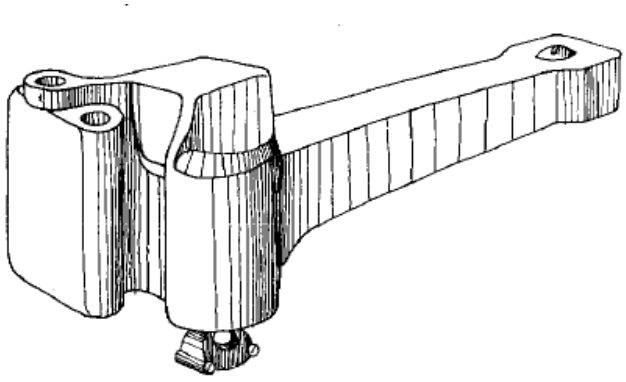

Figure 2.6 Typical design of the coupler [1].

2.3.1.2 Draft Gears

Draft gears function as longitudinal shock absorbers during train operations. They are generally installed on each railcar in series with the underframe. When the coupler forces are transmitted to the draft gears, they change the overall length of the draft gears. When the draft gears are subjected to excessively large coupler forces, they reach their maximum displacement and become solid. The coupler forces are then directly transmitted to the railcar underframe.

Generally, draft gears use dry friction to absorb shock energy [1]. Figure 2.7 shows a conventional draft gear that is connected to the wagon underframe.

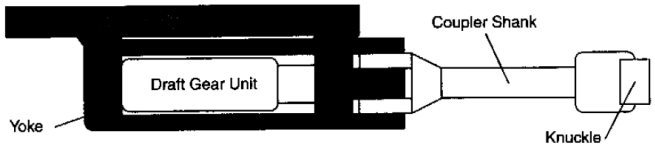

Figure 2.7 Conventional draft gear [4].

2.3.1.3 Cushioning Devices

A cushioning device is another type of longitudinal shock absorber. In this type of device, viscous damping is used to absorb shock energy. The shock energy that is caused by compressive coupler forces is converted into pressure and heat by forcing fluid into cylinders. There are several designs of cushioning devices currently being used in the industry [1].

2.3.2 Dynamic Braking

The traction motors at the locomotive axles are used to start and accelerate the train along the track, and they provide power to drive the wheelsets. The mechanical energy of the rotating wheelsets can be converted into electrical energy by using the traction motors to slow down the train. If the traction motors are electrically connected so they act as generators, they use the turning wheelsets to generate power, and consequently, reduce the speed of the train. This process is called *dynamic braking*. The generated current can be passed through a bank of resistors that dissipates the power as heat, commonly called *rheostatic braking*. The generated power can also be stored back into the railway power supply and is called *regenerative braking* [5]. Early locomotives used DC traction motors, in contrast to newer locomotives that have AC traction motors. Dynamic braking using DC and AC traction motors is discussed in the following sections.

2.3.2.1 DC Traction Motors

For DC traction motors, dynamic braking forces are directly related to train speed. They are limited by current supplied to the traction motors at low speeds, while at higher speeds, they are limited by motor voltage and commutator limits. Figure 2.8 shows an example of the dynamic

brake characteristics for a DC traction motor. Traction force is applied using throttle settings (notches) in the control cabin, while dynamic braking is usually applied using continuous control lever rather than notches [4]. An example of dynamic braking with four level positions using a DC traction motor is shown in Figure 2.9. In this study, a piecewise linear function is fitted to the curve to represent the amount of dynamic braking effort.

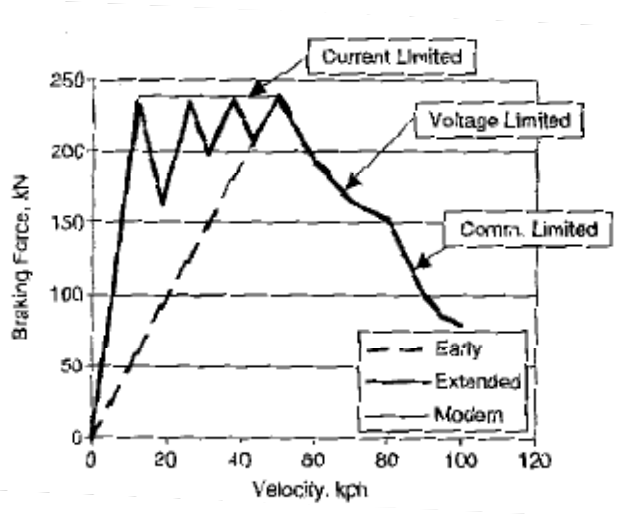

Figure 2.8 Example of dynamic braking versus speeds [4].

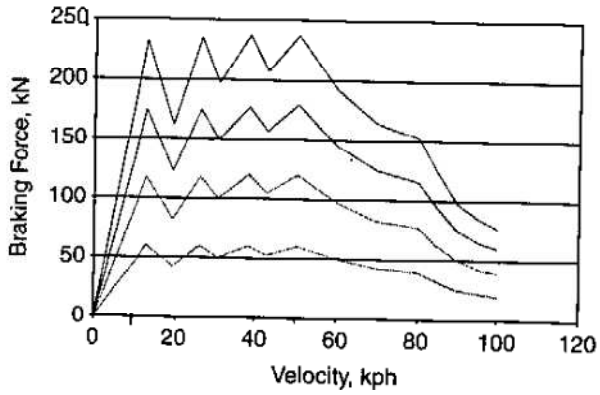

Figure 2.9 Dynamic braking forces for four control positions at a range of train speeds [4].

For DC motors, the braking torque is directly related to the armature current, i. This relationship can be expressed as

$$\tau_{db} = k_t i \tag{2.14}$$

where k_t is the motor torque constant. Figure 2.10 illustrates how a DC motor applies dynamic braking to the wheelset. The equation that governs the generated voltage can be written as

$$v_a = e_b + L_a \frac{di}{dt} + R_a i \tag{2.15}$$

where e_b is the back emf generated in the armature, expressed as

$$e_b = k_e \omega_r \tag{2.16}$$

k_e is the back emf constant, R_a and L_a are the armature resistance (Ω) and inductance (H), and ω_r is the angular velocity of the rotor [23]. The armature current can be controlled so that the desired dynamic braking torque can be achieved. The limitations on controlling the current depend on the traction motor characteristics, as shown earlier in Figure 2.8.

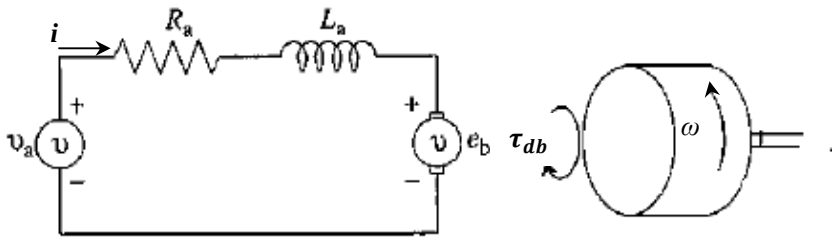

Figure 2.10 DC motor and applied dynamic braking torque to a wheelset [23].

2.3.2.2 AC Traction Motors

For AC traction motors, dynamic braking forces are related to train speed and motor power. They are limited by the motor voltage at low speeds, and by motor power at higher speeds. Induction motors are the most common type of AC traction motors in locomotives. The rotational speed of the wheelset can be controlled by changing the synchronous mechanical angular speed of the traction motor, which is controlled by varying the frequency of the applied armature voltage [27]. Figure 2.11 shows a simple mechanical illustration of how AC traction motors work while accelerating and braking. Motoring or accelerating occurs if ω_s, the

synchronous speed of the motor, is greater than ω_r, the rotor speed. On the other hand, dynamic braking occurs when ω_s is less than ω_r.

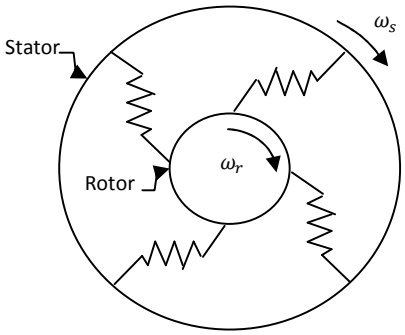

Figure 2.11 Simple sketch of an AC motor.

The electrical excitation frequency can be calculated as

$$\omega_e = \frac{poles}{2}\,\omega_s$$
$$f_e = \frac{\omega_e}{2\,\pi}\ (Hz) \tag{2.17}$$

where ω_e is the electrical excitation of the motor. The slip of the rotor, s, which defines the difference between the synchronous speed and the rotor speed can be expressed as

$$s = \frac{\omega_s - \omega_r}{\omega_s} \tag{2.18}$$

Figure 2.12 shows the induction motor torque-slip curve in motoring and generator regions. As mentioned earlier, dynamic braking is applied when ω_s is less than ω_r, implying negative slip, and consequently applying torque in the opposite direction of the rotor rotation. The continuous braking torque is applied at a very small slip ratio, where the torque-slip relationship is linear. Continuous braking torque cannot be applied at the peak torque or at high slip ratio. To control the applied torque, slip ratio is varied to have the desired amount of torque. This means that ω_s must be controlled by varying ω_e (or f_e). In this case, the slip can be expressed as:

$$s = \frac{\frac{2}{poles}\,\omega_e - \omega_r}{\frac{2}{poles}\,\omega_e} = \frac{\omega_e - \frac{poles}{2}\,\omega_r}{\omega_e} \tag{2.19}$$

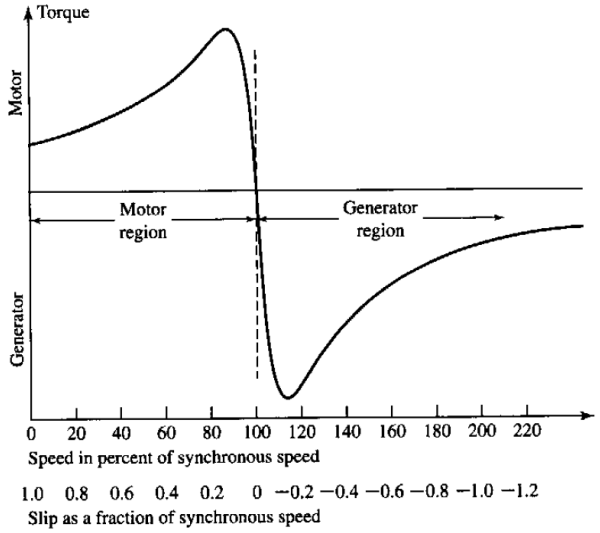

Figure 2.12 Induction motor torque-slip curve for motor and generator region [27].

Figure 2.13 shows the tractive and braking effort diagram for traction motors on EMD's SD90MAC locomotive with total 4300 hp. This diesel electric locomotive uses four-pole squirrel cage, three-phase induction motors [28]. The braking effort plot can be used to simulate the maximum dynamic braking force with the AC traction motor. Note that AC traction motors can apply dynamic braking at low speeds whereas DC motor braking fades quickly at low speeds [5].

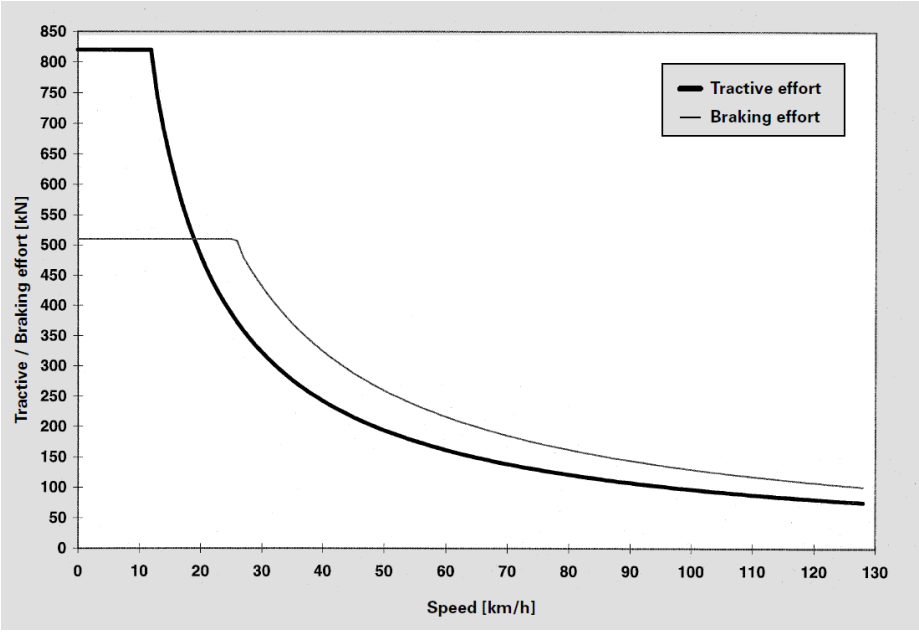

Figure 2.13 Tractive and braking effort diagrams for Siemens SD90MAC with 4300 hp [28].

2.3.3 Air Brake

An air brake is also known as a pneumatic brake, in which compressed air is used to apply brake shoes to the railcar wheels along the train. The air is compressed by a motor-driven compressor at the locomotive. The air brake is controlled using an actuator valve at the locomotive cabin, allowing air to be compressed in the brake pipe or released from the brake pipe. The brake pipe runs along the train and is connected by hoses between vehicles to provide flexibility. Reducing air pressure in the brake pipe causes spring force to apply brake shoes on the wheels while maintaining air pressure causes brake release [5]. For some types of trains, a distributor valve, sometimes called a triple valve, is located at each railcar, and it senses the brake pipe pressure. If the brake pipe pressure falls, the triple valve allows air to pass from the reservoir to the brake cylinders to apply the brake pads. If the brake pipe pressure increases, the triple valve releases the brake cylinder pressure and the brake pads are released from the wheels by a spring. More details on the function of air brake application can be found in [5].

Since an air brake system is basically a fluid dynamic system, there is a time delay in releasing pressure along the pressure pipe for long trains. For a train that is 700 m long, the brake application may start at the last railcar as much as 5 seconds after the initiation of the air brake application. In some cases, this causes severe slack action near the locomotive. Distributed locomotives are used to avoid such problems [4]. An air brake is not usually applied at high speed since it causes heat damage to the wheels.

2.3.4 Propulsion Resistance

Propulsion resistance includes rolling resistance and aerodynamic drag. It can be calculated using the Davis formula [6] which can be written as

$$R = A + B\dot{x} + C\dot{x}^2 \tag{2.20}$$

where

A = Journal resistance coefficient which depends on railcar weight and number of axles. It is independent of train speed.

B = Flanging resistance coefficient which depends on flanging friction and the train speed.

C = Aerodynamic drag coefficient which depends on the shape and the speed of the train.

The last term of the Davis formula represents the aerodynamic drag. Table 2.4 shows several versions of the Davis formula for calculating propulsion resistance in freight trains. Recent developments have been made to these coefficients according to high speed trains, modern equipment, and truck design. According to the American Railway Engineering and Maintenance-of-Way Association (AREMA), the Canadian National version of Davis formula has shown very good results [6], and it can be expressed as

$$\begin{aligned} Rr &= 1.5 + \frac{18n}{W} + 0.03\,\dot{x} + \frac{CA}{10000\,W}\dot{x}^2 \quad \text{(lb/ton)} \\ Rr &= 0.75 + \frac{9.02\,\text{n}}{W} + 0.0305\,\dot{x} + \frac{2.22\,CA}{1000\,W}\dot{x}^2 \quad \text{(N/tonnes)} \end{aligned} \tag{2.21}$$

where

W = total weight of the car (tons or tonnes).

A = cross sectional area of the car (f^2 or m^2).

n = number of axles.

$\dot{x}$ = train speed (miles/hr or m/s).

Rr = propulsion resistance (lb/ton or N/tonne).

Tonne is equal to 1000 kg or 2240 lb, and ton is equal to 2000 lb. The AREMA manual states Equation (2.21) in lb/ton. In this study, the equation that is stated in N/tonnes is developed so that all units are standardized according to the metric system. For example, if we have a 4-axle railcar that weighs 40 tons (36.288 tonnes) with the speed of 30 miles/hr (13.4112 m/s) and it has a cross-sectional area of 150 f^2 (13.935 m^2), the propulsion resistance can be calculated in both unit systems as follows:

Let $C = 5$,

$$Rr = 1.5 + \frac{18(4)}{40} + 0.03\,(30) + \frac{5(150)}{10000\,(40)}(30)^2 = 5.88 \text{ lb/ton}$$

$$Rr = 0.75 + \frac{9.02\,(4)}{36.288} + 0.0305\,(13.4112) + \frac{2.22\,(5)(13.935)}{1000\,(36.288)}(13.4112)^2 = 2.92 \text{ N/tonnes}$$

$$2.920 \text{ N/tonnes} = 2.92 \times \frac{2.2 \text{ lb/N}}{1.1023 \text{ ton/tones}} = 5.84 \text{ lb/ton}$$

This gives similar results with a negligible error. Note that the rolling resistance values are very small. The rolling resistance can be around 16 - 18 lb/axle (32 - 36 N/tonne) [6]. Table 2.5 gives the values of *C* coefficient and areas, *A*, that are used with the Canadian National train resistance formula.

Table 2.4 Different versions of the Davis formula for calculating propulsion resistance [4].

Modified Davis equation (U.S.A.)	$K_a[2.943 + 89.2/m_a + 0.0306V + 1.741k_{ad}V^2/(m_a n)]$ $K_a = 1.0$ for pre 1950, 0.85 for post 1950, 0.95 container on flat car, 1.05 trailer on flat car, 1.05 hopper cars, 1.2 empty covered auto racks, 1.3 for loaded covered auto racks, 1.9 empty, uncovered auto racks $k_{ad} = 0.07$ for conventional equipment, 0.0935 of containers and 0.16 for trailers on flatcars
French Locomotives	$0.65m_a n + 13n + 0.01m_a nV + 0.03V^2$
French Standard UIC vehicles	$9.81(1.25 + V^2/6300)$
French Express Freight	$9.81(1.5 + V^2/(2000...2400))$
French 10 tonne/axle	$9.81(1.5 + V^2/1600)$
French 18 tonne/axle	$9.81(1.2 + V^2/4000)$
German Strahl formula	$25 + k(V + \Delta V)/10$ $k = 0.05$ for mixed freight trains, 0.025 for block trains
Broad gauge (i.e., 1.676 m)	$9.81[0.87 + 0.0103V + 0.000056V^2]$
Broad gauge (i.e., ~1.0 m)	$9.81[2.6 + 0.0003V^2]$

Table 2.5 *C* coefficient and areas for use with the Canadian National train resistance formula [6].

Type of Equipment	C Coefficient	Area (Square Feet)
Box Car	4.9	140
Bulkhead Flat (loaded)	5.3	140
Bulkhead Flat (empty)	12.0	140
Coal Gondola (loaded)	4.2	105
Coal Gondola (empty)	12.0	105
Covered Hopper	7.1	125
Tank Car	5.5	95
Standard Flat Car (without trailers)	5.0	25
Standard Flat Car (with trailers)	5.0	125
Caboose	5.5	145
Conventional Passenger Coach	3.5	130
Modern Lightweight Passenger Equipment	2.0	110
Leading Freight Locomotive	24.0	160
Multi-level Auto Transporter (open)	12.3	150
Multi-level Auto Transporter (closed)	7.1	170

2.3.5 Grade Resistance

The grade resistance is also called gravitational resistance. If a train goes up a hill or down a hill on the track, the weight of each car should be considered in calculations of forces. The gravitational forces can affect the longitudinal train dynamics when the train goes up a hill or down a hill. Figure 2.14 shows how the grade resistance can be calculated. Only the component that is parallel to the car body is considered [4].

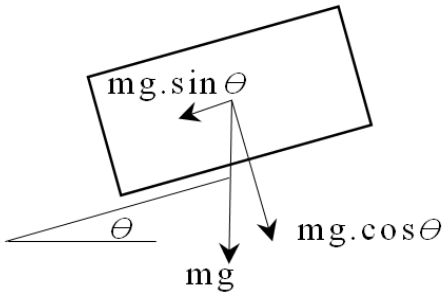

Figure 2.14 Car weight resolved parallel and normal to the car.

2.3.6 Curving Resistance

There is an additional train resistance caused by the train motion on a curved track. This resistance has been studied and approximately evaluated with and without wheel/rail lubrication. According to the AREMA manual, it is about 0.8 lb/ton per degree of curvature without lubrication. In other words, it is similar to a grade of 0.04% per degree. Rail lubrication reduces curve resistance by as much as 50%. All these assumptions can be applied for curves up to 9 degrees. The resistance is reduced by 7 lb/ton for curves that are above 9 degrees [6]. There is an equation provided in [4] that estimates the curving resistance and it given by

$$F_{crv} = 6116/R_{crv} \tag{2.22}$$

where F_{crv} is in Newtons per tonne of car mass, and R_{crv} is the curve radius of the track in meters.

2.4 Model Reference Adaptive Control

The purpose of Model Reference Adaptive Control (MRAC) is to develop a closed loop controller that can update its parameters to change the response of the system. In this study, Model Reference Adaptive Control is applied using the MIT rule, which is used to provide update rules for the adaptive parameters in the controller. The output of the system and the output of the reference model are compared, and the error is used to update the control parameters. The characteristics of the reference model can be chosen to have the desired response. Figure 2.15 gives a schematic diagram of how MRAC is applied. The feedback loop, which is composed of the process and the controller, is called the inner loop. The other feedback loop, which contains the controller parameters, is called the outer loop [7].

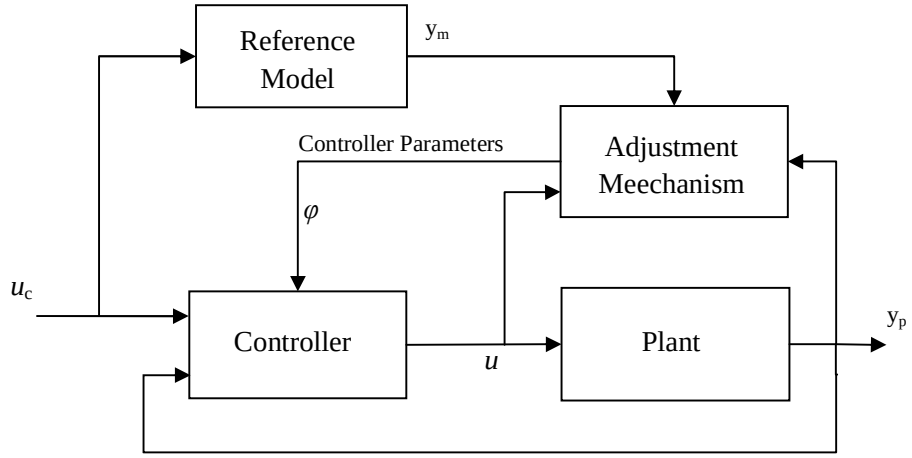

Figure 2.15 Model Reference Adaptive System (MRAS) [7].

There are two methods to apply the adaptive controller: the MIT rule and the Lyapunov theory. The MIT rule is the original approach to Model Reference Adaptive Control. The Lyaponov theory is applied in cases where there is no guarantee of a stable closed-loop system if the MIT rule is used [7]. In this study, the MIT rule is applied to the longitudinal train dynamic system and it gives stable responses. The MIT rule will be presented in the following discussion.

The difference between the system output and the reference model output is the tracking error, expressed as

$$e = y_p - y_m \tag{2.23}$$

Using this error, a cost function of the control parameters can be formed. These parameters are updated according to the choice of the cost function. A typical cost function can be written as

$$J(\varphi) = \frac{1}{2}e^2(\varphi) \tag{2.24}$$

where φ is the parameter that is updated inside the controller. This parameter is updated while minimizing the cost function that is related to the error. The change in J must be in the negative direction of its gradient. This means that the change in φ is proportional to the negative change of J.

$$\frac{d\varphi}{dt} = -\gamma \frac{dJ}{d\varphi} = -\gamma e \frac{de}{d\varphi} \tag{2.25}$$

This relationship is known as the MIT rule. The term $\frac{de}{d\varphi}$ is known as the sensitivity derivative [7]. The controller is assumed to have both an adaptive feedforward (φ_1) gain and an adaptive feedbackward (φ_2) gain. For this assumption, the error function must be rewritten to include both gains.

$$\begin{aligned} u &= \varphi_1 u_c - \varphi_2 y_p \\ e &= y_p - y_m = G_p u - G_m u_c \\ e &= G_p(\varphi_1 u_c - \varphi_2 y_p) - G_m u_c \\ e &= (\varphi_1 G_p - G_m) u_c - G_p \varphi_2 y_p \\ \frac{de}{d\varphi_1} &= G\, u_c, \qquad \frac{de}{d\varphi_2} = -G\, y_p \end{aligned} \tag{2.26}$$

G_p is the transfer function of the system plant, and G_m is the transfer function of the reference model. G is assumed in the above equations for the sensitivity derivatives since the plant transfer function is usually not known [8]. The closed-loop characteristics can be substituted for the plant characteristics. It can be assumed that

$$\begin{aligned} \frac{de}{d\varphi_1} &= \frac{(a_{1m}s + a_{0m})}{(s^2 + a_{1m}s + a_{0m})}\, u_c \\ \frac{de}{d\varphi_2} &= -\frac{(a_{1m}s + a_{0m})}{(s^2 + a_{1m}s + a_{0m})}\, y_p \end{aligned} \tag{2.27}$$

Then, applying the MIT rule,

$$\begin{aligned} \frac{d\varphi_1}{dt} &= -\gamma e \frac{de}{d\varphi_1} = -\gamma \frac{(a_{1m}s + a_{0m})\, u_c}{(s^2 + a_{1m}s + a_{0m})}\, e \\ \frac{d\varphi_2}{dt} &= -\gamma e \frac{de}{d\varphi_2} = \gamma \frac{(a_{1m}s + a_{0m})\, y_p}{(s^2 + a_{1m}s + a_{0m})}\, e \end{aligned} \tag{2.28}$$

where γ is a constant and is called adaptation gain. There are methods for determining the adaptation gain if the system transfer function is known [7], but in most cases, such as

longitudinal train dynamic system, the transfer function is difficult to obtain. Increasing γ results in faster adaptation and consequently quicker system response. However, this may cause system instability. Decreasing γ results in slower adaptation and consequently longer response time [8]. Figure 2.16 shows details of how MRAC is applied. The reference model characteristics can be chosen according to the assumptions that $b_m = a_{0m} = \omega^2$ and $a_{1m} = 2\xi\omega$. More information on the simulation of the adaptive systems using the MIT rule and the application of a PID controller using MRAC can be found in [31] and [32].

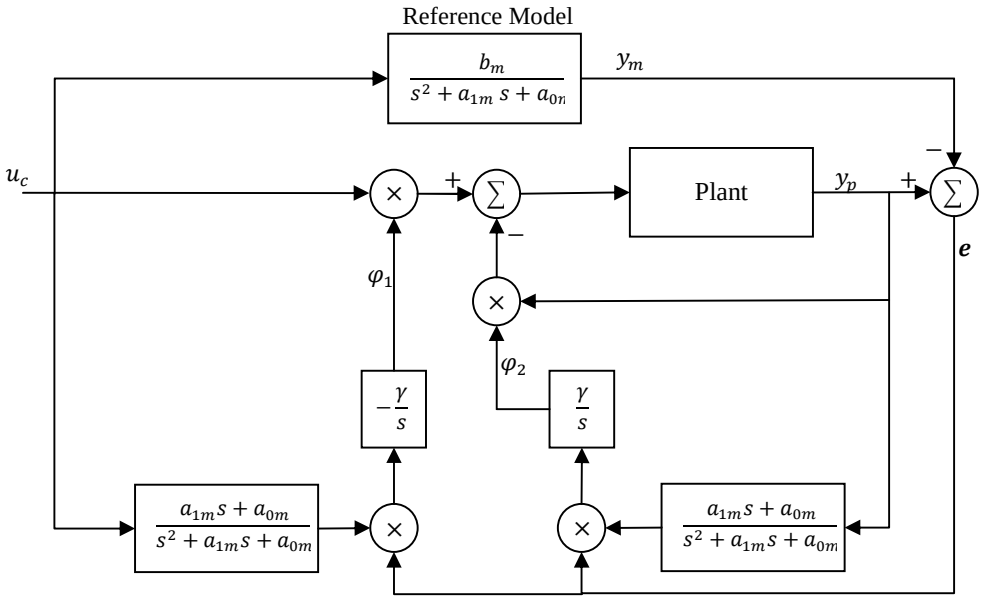

Figure 2.16 Block diagram of MRAC applied to a system [8].

2.5 Review of Past Research

Wheel/rail contact creepages and creep forces are important in understanding the railway vehicle dynamics. For safe train operations, wheel/rail adhesion conditions are very important to consider when studying creep forces in order to avoid wheel skid during braking. In [10], Polach studied an advanced creep force model for railway vehicle dynamics when running on adhesion limit. In his study, he considered the influence of longitudinal, lateral, spin creepages, and the shape of the contact ellipse on the railway vehicle dynamics. He also considered the friction coefficient for dry and wet conditions and it is assumed that it is fixed for each simulation.

Polach found that large creep forces mainly occur in the longitudinal direction at the time of traction or braking. Measurements were modeled for five types of locomotives under different weather and wheel/rail conditions. In [11], estimation of the wheel/rail adhesion coefficient was studied under different wet conditions using two kinds of twin-disc rolling contact machines. The boundary friction coefficient is estimated to be in the range of 0.20 – 0.45. The results roughly agreed with the field test results of the Japanese Shinkansen vehicle. Also, adhesion tests under various speeds and contamination conditions were carried out using a full-scale roller rig in [12]. The results conclude that the adhesion coefficient has high values for dry and clean surfaces and does not change much for all ranges of speeds. It also has low values for oil contamination conditions and does not change much for all ranges of speeds. In [13], rolling contact phenomena, creepages on wheel/rail contact, and creep force models for longitudinal train dynamics are presented. The models were validated with the tilting train, Hanvit-200. It is also shown in this paper that the proposed models are able to analyze the dynamic behavior of the brake and skid characteristics. Zhao, Liang, and Iwnicki [29] have proposed an approach to estimate the creep force and creepage between the wheel and rail using Kalman filter. Then, the friction coefficient is identified using the estimated creep force-creepage relationship. To simulate the system, the authors have developed a mathematical model that includes an AC motor, wheel, and roller. In [30], the authors have presented an estimation method for wheel-rail friction coefficient using values that include angular velocity of the wheel, the moment generated by the braking force and the moment generated by the wheel load. The proposed approach is based on an adaptive observer method that estimates the unknown parameter.

Freight trains have two types of braking methods: pneumatic braking and dynamic braking (discussed previously). There are several models on pneumatic brakes, and the study of pneumatic brake models requires modeling and design of brake pipe, triple valve systems, and other pneumatic brake elements. In addition, it requires the study of fluid flow dynamics. Research is still on going regarding pneumatic brake modeling and improvements. Tadeusz Piechowiak discussed and verified some pneumatic brake models [14]. Also, he developed a simulation method for pneumatic brakes that includes air viscosity, brake pipe branches, heat transfer, and pipe and cylinder pressures [15]. There is substantial research on wheel slip prevention through controlling pneumatic brake forces. Nankyo, Ishihara, and Inooka [33] have studied control performance of a pneumatic brake including its nonlinear property and dynamics.

They developed a mathematical model for the brake chamber, and used it to improve train deceleration by applying a feedback control method. Zhiwu, Haitao, and Yanfen [34] have developed a longitudinal dynamic model for a 20,000-ton heavy-haul train operating in the DaQunlink line to analyze the in-train forces while braking. They highlight the problems in using synchronous air brake control and propose using asynchronous brake control in further studies for eliminating these problems. Wu, Chen, Lu, and Cheng [35] have proposed a train simulation model that includes adhesion coefficient, pneumatic unit, and a simple longitudinal train model for heavy-haul freight trains. A deceleration-oriented control method is included in the model for an Electronically Controlled Pneumatic (ECP) brake in order to reduce high coupler forces between vehicles.

The function of anti-skid control in trains is different from the antilock braking system (ABS) used in automobiles. For passenger trains, all wheels along the train are equipped with pneumatic brakes. In-train forces must be considered while braking. Pneumatic brakes experience delays in the application at rear cars, especially for long trains. Additionally, the mechanism of the pneumatic brakes and the brake shoes are different. Some research has been done on improving anti-skid control of pneumatic brakes. More information on pneumatic brake control can be found in [36 – 38]. For freight trains, which were the main focus in this research, pneumatic brakes are applied only at low speeds, say less than 10 km/hr, and in emergency situations. For anti-skid control, dynamic braking forces must be controlled which do not depend on brake shoes like pneumatic brakes.

Less research has been done on wheel slip detection and prevention using traction motor control. Gissl, Glasl, and Ove have presented an approach for adhesion control in traction based on the input motor mechanical speed and motor torque for a three-mass model (motor and two wheels) [39]. The controller detects the difference between the motor torque and estimated load torque. This difference is limited to a certain pre-specified value. The torque load is estimated based on motor torque and the rotational speed of the motor. Four phases of controller operation are studied: increasing motor torque, motor torque exceeds load torque, motor torque is below a given threshold, and motor torque is below load torque. For example, the controller reduces motor torque when the observed load torque decreases below its allowable limit. The accuracy of the estimation of load torque is not efficient in this controller. Also, the developed dynamic

model is not realistic since there are no bogies or carbody included. In addition, the controller is based on a pre-determined threshold that uses an assumed peak adhesion coefficient.

Matsumoto, Eguchi, and Kawamura [40] have presented a re-adhesion control method for train traction. This control method was for a single-inverter-multiple-induction-motors drive system. It adjusts the accelerating torque according to the estimated adhesive forces between wheel and rail. Two models of adhesive force are assumed based on two wheel-rail conditions. These models are used in the control method in order to prevent wheelset slipping. The controller searches the peak adhesive force in one of the assumed models and adjusts the torque accordingly. The problem is that the unstable condition is very close to the peak adhesive force. This leads to problems in the controller robustness. Furthermore, the assumed adhesive force models did not include all wheel-rail conditions. The control method takes wheel speed measurement from one wheelset and uses a single inverter, which means that the currents that pass through the traction motors are identical. If there is a sudden reduction in the adhesion at one of the wheel-rail contacts, this may cause wheel lockup. The study was targeted toward the Shinkansen, the fastest bullet train in Japan.

For locomotives with DC traction motors, the conventional method of detecting wheelset slipping is by connecting two armature windings of the traction motors of the bogie. If a slipping occurs at one wheelset, the connection detects a difference in the potentials. In this case, a lamp or sound signal informs the train engineer. The engineer then interrupts the excitation of the DC traction motor to stop the slipping for a short time. If there is a low adhesion short section on the track (lubricated rail), the slipping is going to stop. If the slipping does not stop, sand is applied at the wheel-rail contact leading edge to increase adhesion. The train engineer has to continue interrupting the excitation of the DC traction motor if slipping continues, which usually happens. This may cause excessive in-train forces and lead to derailments [41]. To overcome this problem, the slipping can be determined by measuring the armature currents of all traction motors. The variation of the traction motor's armature current is the signal for the slipping control. The maximum current of all traction motors is determined and compared in a pulse gating unit with a signal from a separately excited generator's voltage sensor. This allows maintaining fixed voltage for a very short time in order to stabilize motor load characteristics during the dynamic process when the wheelset starts slipping [41]. A disadvantage in this

control method is that it does not put the wheel/rail contact mechanics into consideration. This means it works only when it detects slipping or when the wheel starts to slip, which may still cause damage to the wheels especially in freight trains where wheels are under heavy loads.

In [42 and 43], the authors have proposed a re-adhesion control scheme that blends two conventional methods: motor current control and slip speed control. If one fails the other is activated. If both fail (usually when all wheels are simultaneously slipping), the estimated acceleration criterion control is activated. This control scheme is based on the estimation of the reference speed of a bogie. The reference speed is estimated using speed sensors on two axles of a bogie and two axles on an adjacent bogie, and is then compared with an extra train speed indicator. If the reference speed is less than the wheel speed from the speed indicator, it is allowed to increase according to the estimated train acceleration. If the reference speed is greater than the wheel speed from the speed indicator, it is allowed to decrease according to the estimated train acceleration. The authors have verified the proposed control method using a downscaled simulator. The results show the performance of the control method with a lot of oscillations. Also, it takes time to regain adhesion. Based on these results, this control method may not be efficient in high-speed trains as proposed. In addition, it is mainly based on estimation of the train reference speed and train acceleration, using wheel speeds and a speed indicator.

Watanabe and Yamashita [44] have presented an anti-slip re-adhesion control method using vector control without speed sensor. Their method focuses on the current from each induction motor for multiple motor drive systems with one inverter, and it detects the torque current differences between two induction motors by setting a threshold. If the assumed threshold is reached, the controller reduces current to both traction motors uniformly since there is one inverter. A fixed threshold of 30 Amps is assumed for all simulations. This is not realistic however because the threshold should be a function of speed. Also, the study includes only a sudden drop of 10% of adhesion force that is not sufficient to prove the efficiency of the control method.

Mei, Yu, and Wilson have proposed a new approach for wheel slip control [45]. The study is based on the detection of torsional vibration of a wheelset when slipping. Considering the shaft elasticity, a simplified model that consists of dominant modes of the wheelset is developed to

investigate slip detection and re-adhesion scheme. The natural frequency for a wheelset is typically in the range of 60 Hz or higher. The simulation results show torsional vibrations when there is a sudden drop in the adhesion. The authors mentioned that the study provides an excellent wheel slip detection idea, but in practice it requires measurement of the motor torque. Furthermore, they state that mounting strain gauges on axles would have many challenges in terms of sensor reliability and signal transmission. The study develops a Kalman filter to estimate torsional vibration using speed of traction motors and a linear creep force-creepage curve. Simulation results show that the control approach can reduce motor torque when detecting the estimated torsional vibration. The re-adhesion is achieved in about 1 - 3 seconds depending on the operating conditions. The authors conclude that better estimation of torsional vibrations is needed for their proposed method, along with experimental verification.

A railway vehicle model can be developed using different multibody formulation methodologies, such as Newton-Euler formalism or Lagrange's formalism [48]. The formulation methodology used to model the train can be chosen based on the research objectives. A longitudinal train dynamics model is a two-dimensional model that is used to study the forward motion of the train. This model includes all forward motion resistances such as braking forces, and grade, curving, and propulsion resistances. Therefore, the multibody formulations of the longitudinal train model is usually developed using Newton's law and is applied to rigid bodies connected by springs and dampers. Since this study focuses on the train braking forces and the train stopping distance, only the longitudinal train dynamics model is considered.

Longitudinal bogie dynamics were studied in [16] using an experimental method to evaluate the effects of the braking torque. A 24 m long track was used with a maximum bogie speed of 4 m/s in the experiment. Two levels of pneumatic braking efforts were used to evaluate the braking torque and braking skid. In addition, acceleration, speed, and traveled distance were studied during braking. A simple model of the longitudinal dynamics of a long freight train was developed in [17]. The authors considered railcars as lumped parameters in the model, with only pneumatic braking included. The propagation of pressure signals along brake pipe was also included in the model. In [18], a railcar model was developed to study wagon body pitch, derailment, and wheelset skid during braking. This model showed that suddenly applying large braking or traction forces can cause wheel skid. Also, it is mentioned in the study that track

defects play an important role in increasing railcar pitch. On a defective track, large braking or traction torques exerted on the wheelset may cause wheel-unloading. Ansari, Esmailzadeh, and Younesian [19] conducted a comprehensive parametric study on longitudinal dynamics of freight trains. A non-linear model was developed for ten railway vehicles connected by automatic couplers. The parametric study investigates how different parameters affect the longitudinal train dynamics. Parameters that were varied included spring stiffness and damping coefficient of the automatic coupler, operational speed, and acceleration or deceleration. Also, effects of different load distribution patterns on longitudinal train dynamics were studied. Effects of an empty railcar location in a train and placement of a second locomotive were discussed. All types of retardation forces, including braking forces, were included in the model. This study can help with coupler design and safe train operations.

A PC-based tool was introduced in [20] to calculate the train braking distance for different train types. Train mass, braking effort, and grade resistance were considered. However, there are limitations to using this tool since it makes simplifying assumptions. This tool is a good concept to estimate the braking distance, but it needs significant improvements. A Hardware-In-Loop (HIL) system was built for the braking system of the Korean High-Speed Train in [21]. A DSP board was used in the HIL system to obtain real-time simulations. Two-dimensional dynamic equations of seven-railcar model were developed. Real-time simulations included several types of braking to investigate the adhesion limits, and braking distance and ride comfort were discussed in the paper. Real-time simulations were presented in [22] to analyze the braking performance of railway vehicles using an HIL system. The dynamic model of a railway vehicle was developed, including carbody, bogies, wheelsets, and creep forces. The HIL system is composed of a DSP board to run the dynamic model and real hardware components of an anti-skid control unit (ASCU). The ASCU estimates the required braking forces according to anti-skid logic. The validity of the HIL system was verified by comparing the HIL system results with the off-line simulation results that had constant brake forces.

We have seen that each group of researchers has focused on longitudinal train dynamics from different perspectives. The study of the longitudinal train model leads to a better understanding of the effects of various conditions and different retardation forces on the train dynamics. Once the behavior of the longitudinal train dynamics is analyzed and understood, the control design

can be applied. One of the recent developments in railway networks is using positive train control (PTC), which is a predictive collision avoidance technology that uses GPS to control the traffic on the U.S. railroad network. The spacing of trains in PTC is based on estimating the stopping distance of each train. Often, trains are spaced apart conservatively (farther than may be needed) in order to positively ensure that they will come to a stop without colliding. The Rail Safety Improvement Act (RSIA) has mandated the widespread installation of PTC systems by December 2015 [9]. In this study, estimation of train braking distance under different operating conditions is investigated. Traction and braking are the most critical reasons for wheel lockup and high coupler forces. It is reasonable to assume that maximizing the braking forces leads to minimizing the train braking distance. The problems that are associated with maximizing braking forces may include high creep forces that may cause wheel lockup, and high coupler forces that may lead to derailment of railcars.

2.6 Research Justification

Dynamic braking forces can be controlled such that maximum braking effort is achieved while avoiding wheel lockup and high coupler forces. If this control strategy is achieved, the train braking distance is minimized, allowing train spacing to be minimized and track line capacity maximized. The vast majority of past studies consider wheel slip detection and prevention *after* wheels start slipping. Such an approach does not necessarily take advantage of maximum available dynamic braking before wheel lock-up. MRAC is best suited for achieving maximum dynamic braking while eliminating wheel lock-up and other requirements, such as limiting coupler forces during braking. The reference model can be chosen based on the available braking effort and adhesion coefficient that can vary while maintaining acceptable coupler forces. In other words, the train braking behavior follows a reference model that is designed with train operating considerations to ensure improved train braking. In addition, since the reference model is known, train braking distance can be estimated a priori. Implementing MRAC in future collision avoidance systems, such as PTC, can further improve their performance during braking and most likely lead to closer spacing of trains with higher confidence.

Chapter 3

Longitudinal Train Model

3.1 Introduction

The longitudinal dynamic behavior of a train is a function of brake forces, track geometry, wheel/rail interaction forces, propulsion resistance, and railcar connection forces. A multibody formulation of the train longitudinal dynamics results in a set of differential equations for each carbody, truck, and wheelset. When considering longitudinal train dynamics, most researchers ignore the vertical and lateral movements, as well as the suspension forces, such as in references [1], [4], [18] and [19]. In this study, a two-dimensional analysis of the train will be performed that includes the vertical motion and all suspension forces in order to have a more realistic model. In this chapter, the kinematics of the train model will be presented. Then the equations of motion of the carbody, truck, and wheelset will be developed. General equations of motion for any carbody, truck, and wheelset will be stated so they can be applied to any train with different numbers of railcars.

3.2 Kinematics

A train model with several freight cars is shown in Figure 3.1. The first lead unit is considered as a locomotive with six wheelsets. The other units are freight railcars with four wheelsets each. Only the dynamics along the longitudinal (x) and vertical (z) directions are considered in this model. The dynamic equations for each railcar and locomotive are derived. Two adjacent car bodies are connected by a coupler that is modeled as a coupler slack, a spring and a damper. The car bodies' connections can also be modeled as a simple coupler without the coupler slack. Both coupler models will be considered and compared. The car bodies are connected to the trucks by springs and dampers in the x and z directions. Each truck is connected to the wheelsets by springs and dampers in the x and z directions. For the purpose of this study, two assumptions are made:

(1) the track is tangent, which means grade and curve resistances are ignored, and

(2) the wheelsets do not lose contact with the rail in the *z* direction, i.e., they do not lift off the rail vertically.

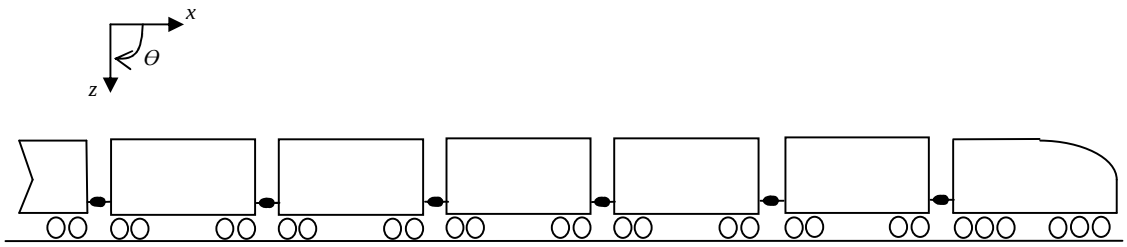

Figure 3.1 Longitudinal train model.

The first unit, which is the locomotive, can be modeled as a mass connected by springs and dampers as shown in Figure 3.2. The car body is connected to the front and rear bogies, and is also connected to the railcar behind it by a coupler. Each bogie is connected to three wheelsets. The suspensions connect the wheelsets and truck sideframes as shown in Figure 3.3. The car travels in the *x* direction, and the positive *z* direction is downward.

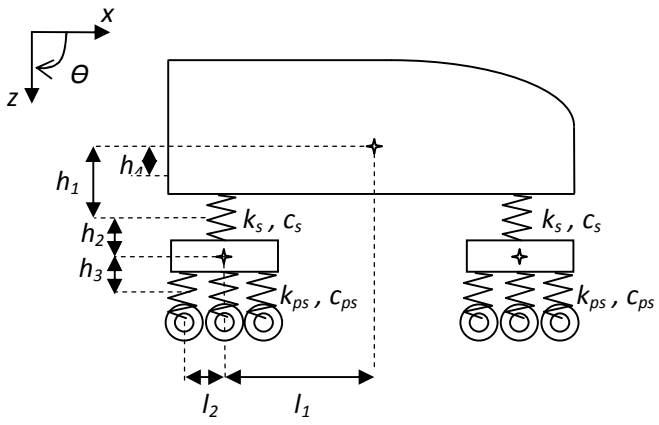

Figure 3.2 Simple sketch of a train single car model.

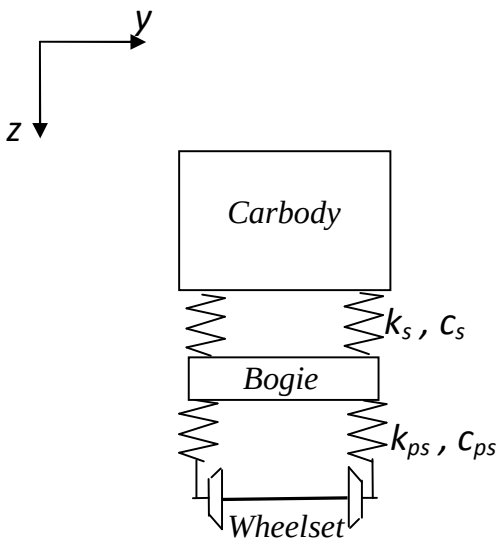

Figure 3.3 Front view of the train model.

3.3 Equations of Motion

3.3.1 Car Body Equations of Motion

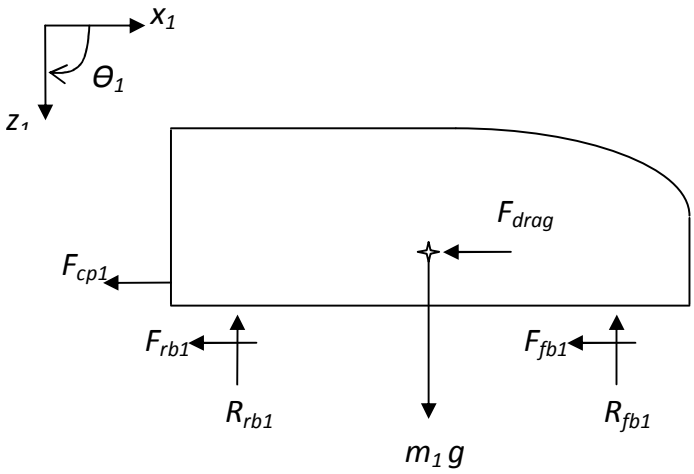

Figure 3.4 Free body diagram of the car body.

Using the free body diagram in Figure 3.4 in the *x*, *z*, and θ directions,

$$\begin{aligned} m_1\ddot{x}_1 &= -F_{fb}^1 - F_{rb}^1 - F_{cp}^1 - F_{drag}^1 \\ m_1\ddot{z}_1 &= -R_{fb}^1 - R_{rb}^1 + m_1 g \\ I_1\ddot{\theta}_1 &= \left(F_{fb}^1 + F_{rb}^1\right).h_1 + \left(R_{rb}^1 - R_{fb}^1\right).l_1 + F_{cp}^1 .h_4 \end{aligned} \tag{3.1}$$

where m_1 and I_1 are the mass and the mass moment of inertia of the locomotive, respectively. F_{cp}^1 is the first coupler force. F_{drag}^1 is the aerodynamic drag force that is assumed to be applied at the carbody center of mass. F_{fb}^1, F_{rb}^1, R_{fb}^1 and R_{rb}^1 are the secondary suspension forces of the front and the rear bogie that act on the locomotive. The superscript 1 represents the first unit which is the locomotive. The subscripts *fb* and *rb* represent the front bogie and the rear bogie, respectively. The suspension forces of the front and the rear bogies can be expressed as:

$$\begin{aligned} F_{fb}^1 &= 2k_{xs}\left(x_1 - x_{fb}^1\right) + 2c_{xs}\left(\dot{x}_1 - \dot{x}_{fb}^1\right) \\ F_{rb}^1 &= 2k_{xs}(x_1 - x_{rb}^1) + 2c_{xs}(\dot{x}_1 - \dot{x}_{rb}^1) \\ R_{fb}^1 &= 2k_{zs}\left(z_1 + l_1\theta_1 - z_{fb}^1\right) + 2c_{zs}\left(\dot{z}_1 + l_1\dot{\theta}_1 - \dot{z}_{fb}^1\right) \\ R_{rb}^1 &= 2k_{zs}(z_1 - l_1\theta_1 - z_{rb}^1) + 2c_{zs}\left(\dot{z}_1 - l_1\dot{\theta}_1 - \dot{z}_{rb}^1\right) \end{aligned} \tag{3.2}$$

where x_1, z_1, and θ_1 are the *x* and *z* locations, and the pitch angle of the locomotive. x_{fb}^1, x_{rb}^1, z_{fb}^1, and z_{rb}^1 are the *x* and *z* locations of the front and the rear bogies. k_{xs}, c_{xs}, k_{zs}, and c_{zs} represent the secondary suspension springs and dampers in the *x* and *z* directions. If the coupler slack is considered, the coupler force can be expressed as

$$\begin{aligned} F_{cp}^1 &= k_{cp}(x_1 - x_2) + c_{cp}(\dot{x}_1 - \dot{x}_2) && \text{if } x_1 - x_2 \geq 0 \quad \text{(draft)} \\ F_{cp}^1 &= 0 && \text{if } x_1 - x_2 \geq -sk \\ F_{cp}^1 &= k_{cp}(x_1 - x_2 + sk) + c_{cp}(\dot{x}_1 - \dot{x}_2) && \text{if } x_1 - x_2 < -sk \quad \text{(buff)} \end{aligned} \tag{3.3}$$

where sk is the coupler slack length. x_2 is the *x* location of the second railcar. k_{cp} and c_{cp} represent the coupler spring and damper. If the coupler slack is not considered, the coupler force can be written as

$$F_{cp}^{1} = k_{cp}(x_1 - x_2) + c_{cp}(\dot{x}_1 - \dot{x}_2) \tag{3.4}$$

General equations of motion for all car bodies can be written as

$$\begin{aligned} m_i\ddot{x}_i &= -F_{fb}^{i} - F_{rb}^{i} + F_{cp}^{i-1} - F_{cp}^{i} - F_{drag}^{i} \\ m_i\ddot{z}_i &= -R_{fb}^{i} - R_{rb}^{i} + m_i g \\ I_i\ddot{\theta}_i &= \left(F_{fb}^{i} + F_{rb}^{i}\right).h_1 + \left(R_{rb}^{i} - R_{fb}^{i}\right).l_1 + \left(F_{cp}^{i} - F_{cp}^{i-1}\right).h_4 \end{aligned} \tag{3.5}$$

where *i* represents the car number in the train. The general formulations of the secondary suspension forces can be expressed as

$$\begin{aligned} F_{fb}^{i} &= 2k_{xs}\left(x_i - x_{fb}^{i}\right) + 2c_{xs}\left(\dot{x}_i - \dot{x}_{fb}^{i}\right) \\ F_{rb}^{i} &= 2k_{xs}(x_1 - x_{rb}^{1}) + 2c_{xs}(\dot{x}_1 - \dot{x}_{rb}^{1}) \\ R_{fb}^{i} &= 2k_{zs}\left(z_i + l_i\theta_i - z_{fb}^{i}\right) + 2c_{zs}\left(\dot{z}_i + l_i\dot{\theta}_i - \dot{z}_{fb}^{i}\right) \\ R_{rb}^{i} &= 2k_{zs}\left(z_i - l_i\theta_i - z_{rb}^{i}\right) + 2c_{zs}\left(\dot{z}_i - l_i\dot{\theta}_i - \dot{z}_{rb}^{i}\right) \end{aligned} \tag{3.6}$$

For the coupler forces, if the superscript $i - 1 = 0$, $F_{cp}^{i-1} = 0$. Also, if $i =$ total number of cars, $F_{cp}^{i} = 0$. The general equation for the coupler forces with the slack model can be written as

$$\begin{aligned} F_{cp}^{i} &= k_{cp}(x_i - x_{i+1}) + c_{cp}(\dot{x}_i - \dot{x}_{i+1}) && \text{if } x_i - x_{i+1} \geq 0 \\ F_{cp}^{i} &= 0 && \text{if } x_i - x_{i+1} \geq -sk \\ F_{cp}^{i} &= k_{cp}(x_i - x_{i+1} + sk) + c_{cp}(\dot{x}_i - \dot{x}_{i+1}) && \text{if } x_i - x_{i+1} < -sk \end{aligned} \tag{3.7}$$

Whereas the general equation for the coupler forces without the slack model can be written as

$$F_{cp}^{i} = k_{cp}(x_i - x_{i+1}) + c_{cp}(\dot{x}_i - \dot{x}_{i+1}) \tag{3.8}$$

3.3.2 Bogie Equations of Motion

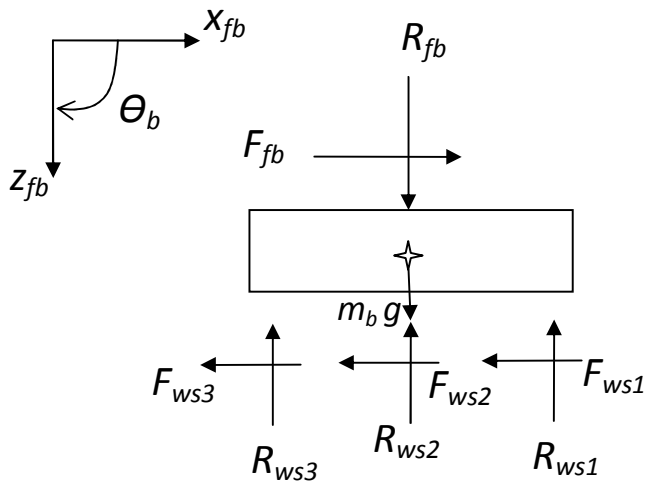

Figure 3.5 Free body diagram of the bogie.

The wheelsets are in contact with the rail and there is no relative motion between the wheel and the rail in the *z* direction. First, the front bogie of the locomotive is considered. Using the free body diagram in Figure 3.5, the equations of motion can be written as

$$\begin{aligned} m_b \ddot{x}_{fb}^1 &= F_{fb}^1 - F_{ws1}^1 - F_{ws2}^1 - F_{ws3}^1 \\ m_b \ddot{z}_{fb}^1 &= R_{fb}^1 - R_{ws1}^1 - R_{ws2}^1 - R_{ws3}^1 + m_b g \\ I_b \ddot{\theta}_{fb}^1 &= F_{fb}^1\, h_2 + (F_{ws1}^1 + F_{ws3}^1) h_3 \; + (R_{ws3}^1 \; - R_{ws1}^1) l_2 \end{aligned} \tag{3.9}$$

where m_b and I_b are the mass and the mass moment of inertia of the bogie. F_{ws1}, F_{ws2}, F_{ws3}, R_{ws1}, R_{ws2} and R_{ws3} are the primary suspension forces. The subscripts $ws1$, $ws2$, and $ws3$ represent the first, second, and third wheelsets, respectively. The primary suspension forces can be expressed as

$$
\begin{aligned}
F^1_{ws1} &= 2k_{xps}\left(x^1_{fb} - x^1_{ws1}\right) + 2c_{xps}\left(\dot{x}^1_{fb} - \dot{x}^1_{ws1}\right)\\
F^1_{ws2} &= 2k_{xps}\left(x^1_{fb} - x^1_{ws2}\right) + 2c_{xps}\left(\dot{x}^1_{fb} - \dot{x}^1_{ws2}\right)\\
F^1_{ws3} &= 2k_{xps}\left(x^1_{fb} - x^1_{ws3}\right) + 2c_{xps}\left(\dot{x}^1_{fb} - \dot{x}^1_{ws3}\right)\\
R^1_{ws1} &= 2k_{zps}\left(z^1_{fb} + l_2\theta^1_{fb}\right) + 2c_{zps}\left(\dot{z}^1_{fb} + l_2\dot{\theta}^1_{fb}\right)\\
R^1_{ws2} &= 2k_{zps}\,.\,z^1_{fb} + 2c_{zps}\,.\,\dot{z}^1_{fb}\\
R^1_{ws3} &= 2k_{zps}\left(z^1_{fb} - l_2\theta^1_{fb}\right) + 2c_{zps}\left(\dot{z}^1_{fb} - l_2\dot{\theta}^1_{fb}\right)
\end{aligned}
\tag{3.10}
$$

Similar equations of motion for the rear bogie can be obtained where the subscripts *ws1*, *ws2*, *ws3*, and *fb* are replaced with *ws4*, *ws5*, *ws6*, and *rb*, respectively. The general equations of motion for all front bogies of all cars can be written as

$$
\begin{aligned}
m_b\ddot{x}^i_{fb} &= F^i_{fb} - \sum_{j=1}^{k} F^i_{wsj}\\
m_b\ddot{z}^i_{fb} &= R^i_{fb} - \sum_{j=1}^{k} R^i_{wsj} + m_b g\\
I_b\ddot{\theta}^i_{fb} &= F^i_{fb}\,h_2 + \left(F^i_{ws1} + F^i_{wsk}\right)h_3 + \left(R^i_{wsk} - R^i_{ws1}\right)l_2
\end{aligned}
\tag{3.11}
$$

and for all rear bogies of all cars

$$
\begin{aligned}
m_b\ddot{x}^i_{rb} &= F^i_{rb} - \sum_{j=k+1}^{2k} F^i_{wsj}\\
m_b\ddot{z}^i_{rb} &= R^i_{rb} - \sum_{j=k+1}^{2k} R^i_{wsj} + m_b g\\
I_b\ddot{\theta}^i_{rb} &= F^i_{rb}\,h_2 + \left(F^i_{ws(k+1)} + F^i_{ws(2k)}\right)h_3 + \left(R^i_{ws(2k)} - R^i_{ws(k+1)}\right)l_2
\end{aligned}
\tag{3.12}
$$

where *k* is 3 for the locomotive, and 2 for all other freight cars.

3.3.3 Wheelset Equations of Motion

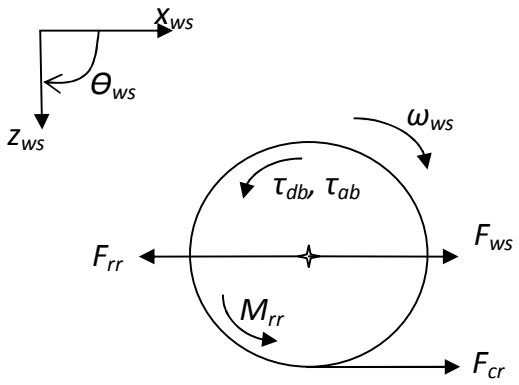

Figure 3.6 Free body diagram of the wheelset.

Consider the first wheelset of the locomotive and apply Newton's law to the free body diagram in Figure 3.6. The equations of motion of the wheelset can be written as

$$\begin{aligned} & m_{ws}\ddot{x}_{ws1}^{1} = F_{ws1}^{1} - F_{rr}^{1} + 2F_{cr1}^{1} \\ & m_{ws}\ddot{z}_{ws1}^{1} = \sum F_z = 0 = m_{ws}g + R_{ws1}^{1} - N_{ws1}^{1} \\ & \Rightarrow\ N_{ws1}^{1} = R_{ws1}^{1} + m_{ws}g \\ & I_{ws}\dot{\omega}_{ws1}^{1} = -M_{rr}^{1} - 2F_{cr1}^{1}r_0 - \tau_{db} - \tau_{ab} \end{aligned} \tag{3.13}$$

where $F_{rr}$and M_{rr} are the rolling resistance force and moment, F_{cr1}^{1} represents the creep force at one wheel/rail contact location for the 1st wheelset, N_{ws1}^{1} is the normal force at the wheel/rail contact point for the first wheelset, τ_{db} represents the dynamic braking torque, and τ_{ab} represents the air braking torque. m_{ws}, I_{ws}, and r_0 are the mass of the wheelset, mass moment of inertia of the wheelset, and the nominal radius of the wheel, respectively. It is assumed that the wheel/rail adhesion coefficient is identical in both the right and left rails. This means that creepage forces are identical on both wheels on the same axle. The equations of motion for the remaining wheelsets can be written by replacing the subscript *ws1* with *ws2, ws3, ws4, ws5,* or *ws6*. The equations of motions of the wheelsets under the second and third car do not include dynamic braking torque since this braking torque can only be applied to the wheelsets under the locomotive. The general equations of motion for all wheelsets can be expressed as

$$
\begin{aligned}
m_{ws}\ddot{x}^i_{wsq} &= F^i_{wsq} - F^i_{rr} + 2F^i_{crq} \\
N^i_{wsq} &= R^i_{wsq} + m_{ws}g \\
I_{ws}\dot{\omega}^i_{wsq} &= -M^i_{rr} - 2F^i_{crq}r_0 - \tau_{db} - \tau_{ab}
\end{aligned}
\tag{3.14}
$$

where q represents the sequence number of the wheelsets, varying from 1 to 6 for the locomotive and from 1 to 4 for the railcars. τ_{db} is zero for the freight cars.

Chapter 4

Simulation and Parametric Study

4.1 Introduction

First, all numerical assumptions, system properties, and force evaluations will be stated. Then the dynamic train models that are with and without coupler slack will be compared. Next, the developed model will be compared with a train model in SIMPACK. Since there is no data available in the literature to compare the results, the model will be verified against SIMPACK. Then the dynamic model of a train that includes three railcars will be used to perform a parametric study to evaluate how various elements will affect the train stopping distance from an initial speed. Parameters that can be varied in the model include initial train speed, railcar weight, wheel-rail interface condition, aerodynamic drag, and dynamic braking force. In addition, the effect of different numbers of railcars will be investigated.

4.2 System Properties and Force Evaluation

For the model comparison and the parametric study, a three-car train model is considered as shown in Figure 4.1. The general equations of motion that were developed in Chapter 3 can be applied to this model. Table 4.1 states the required parameters and coefficients to solve the dynamic equations. Other forces and assumptions will be presented in the following subsections.

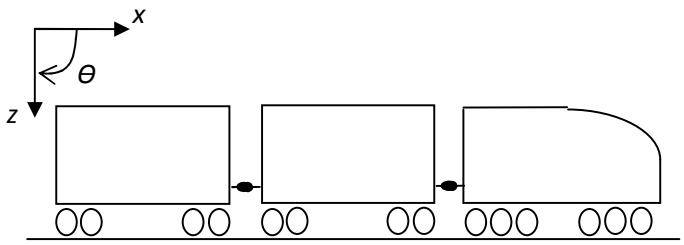

Figure 4.1 Three-car train model.

Table 4.1 System properties and coefficients.

k_{xps}	9.0×10^3 N/m	k_{zps}	5.9×10^7 N/m
c_{xps}	3.5×10^4 N/m.s	c_{zps}	4.0×10^5 N/m.s
k_{xs}	6.0×10^5 N/m	k_{zs}	5.5×10^4 N/m
c_{xs}	1.5×10^5 N/m.s	c_{zs}	1.0×10^4 N/m.s
k_{cp}	1.0×10^9 N/m	m_1 (locomotive)	190,500 kg
c_{cp}	4.0×10^8 N/m.s	m_2, m_3 (loaded freight cars)	130,000 kg
l_1	8 m	m_2, m_3 (empty freight cars)	27,000 kg
l_2	2 m	I_1 (locomotive)	1403 kg.m^2
h_1	1 m	I_2, I_3 (loaded freight cars)	1000 kg.m^2
h_2	0.5 m	I_2, I_3 (empty freight cars)	800 kg.m^2
h_3	0.3 m	Bogie mass	1500 kg
h_4	0.3 m	Bogie mass of inertia	219 kg.m^2
R_1^w	0.5 m	Wheelset mass	500 kg
R_2^w(conical profile)	∞	Wheelset mass of inertia	125 kg.m^2
R_1^r (tangent track)	∞	A, Area (locomotive)	160 ft^2
R_2^r	0.2 m	A, Area (freight cars)	140 ft^2
C coefficient (lcomotive)	24	C coefficient (freight cars)	4.9

4.2.1 Propulsion Resistance

Propulsion resistance includes rolling resistance and aerodynamic drag. The Canadian National version of the Davis formula (see section 2.3.4) will be used. The formula units were originally in the English system, but were then converted into the Metric Systems. The aerodynamic drag can be calculated separately. The formula can be modified to apply to each wheelset and can be rewritten as:

$$Rr = R_{rr} + R_{drag} \tag{4.1}$$

where R_{rr} is the rolling resistance in N/tonne, and R_{drag} is the aerodynamic resistance in N/tonne. Rolling resistance for each wheelset can be calculated as

$$R_{rr} = 0.75 + \frac{9.02}{W_{ws}} + 0.0305\,\dot{x}_{ws} \quad \text{(N/tonne)} \tag{4.2}$$

where W_{ws} is weight on each wheelset in tonnes. The rolling resistance force can then be expressed as

$$F_{rr} = 0.75W_{ws} + 9.02 + 0.0305\,W_{ws}\,\dot{x}_{ws} \ \text{(N)} \tag{4.3}$$

Also, R_{drag} can be calculated as

$$R_{drag} = \frac{2.22\,CA}{1000\,W}\dot{x}^2 \quad \text{(N/tonne)} \tag{4.4}$$

Since aerodynamic drag is calculated for each car, the total weight of the car in tonnes is used. The aerodynamic drag for each car can be expressed as

$$F_{drag}^{i} = \frac{2.22\,CA}{1000}\dot{x}_i^2 \ \text{(N)} \tag{4.5}$$

4.2.2 Creep Force

Since only the longitudinal creep force will be calculated, Kalker's empirical theory can be simplified, and Equations (2.12) can be used. Figure 4.2 shows the normalized creep force after simplifying Kalker's empirical formula; it gives the same results as in Figure 2.3.

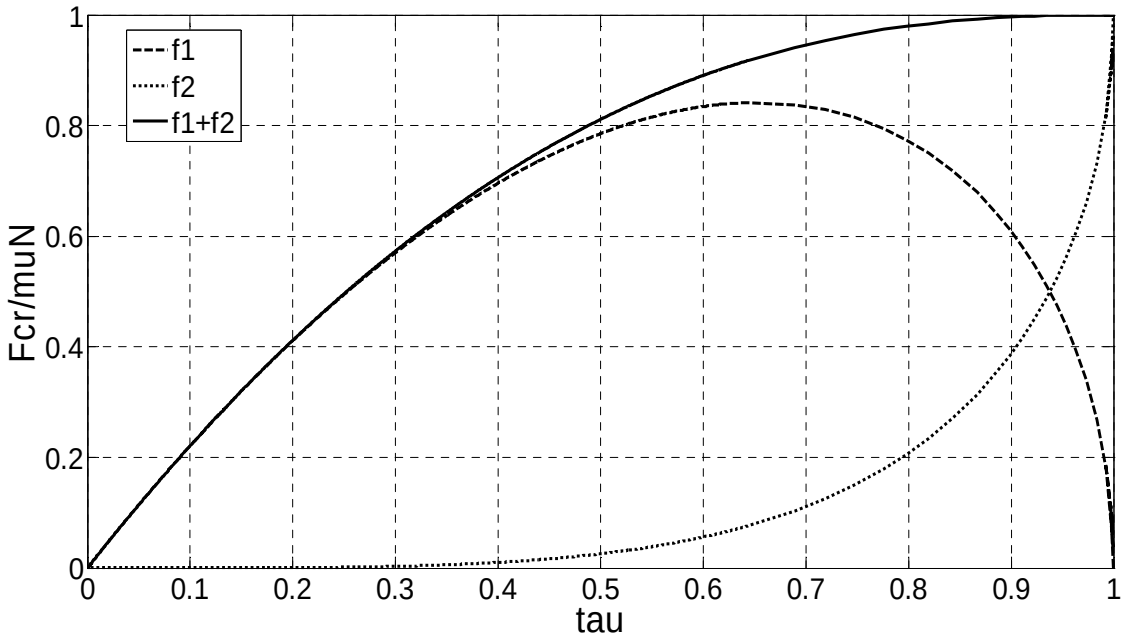

Figure 4.2 Kalker's empirical theory applied to the longitudinal direction only.

4.2.3 Dynamic Braking

As mentioned earlier, dynamic braking is only applied at the locomotives. For DC traction motors, based on the design curves which were provided in Figures 2.8 and 2.9, one can simulate dynamic braking by fitting a piecewise linear function to the curves. Figure 4.3 assumes the dynamic braking torque versus train speed at three different control positions. This braking torque is applied at each wheelset under the locomotive. The highest braking effort can be considered as maximum braking (highest control position), while the lowest braking effort can be considered as minimum braking (lowest control position).

For AC traction motors, if we look at the braking force plot in Figure 2.13 where the force changes from constant to a curve, we can compute the maximum power at each axle as follows

$$P_{max} = \frac{\dfrac{510{,}000\ N\ \times 27000 \dfrac{m}{\text{hr}}}{3600 \dfrac{sec}{\text{hr}}}}{6\ axles} = 638\ \text{kW} \tag{4.6}$$

which gives the maximum power that can be provided by the motor as shown in [28]. This means that for each axle, the maximum braking torque that can be provided at each axle is

$$\tau_{db,max} = \frac{510{,}000\ N\ \times\ 0.5\ m}{6\ axles} =\ 43\ kN.m \tag{4.7}$$

To calculate the maximum braking torque at each axle for high speeds (greater than 27 km/hr),

$$\tau_{db} = \frac{P_{max}\ (\mathrm{W})}{\omega_{ws}(rad/s)} \tag{4.8}$$

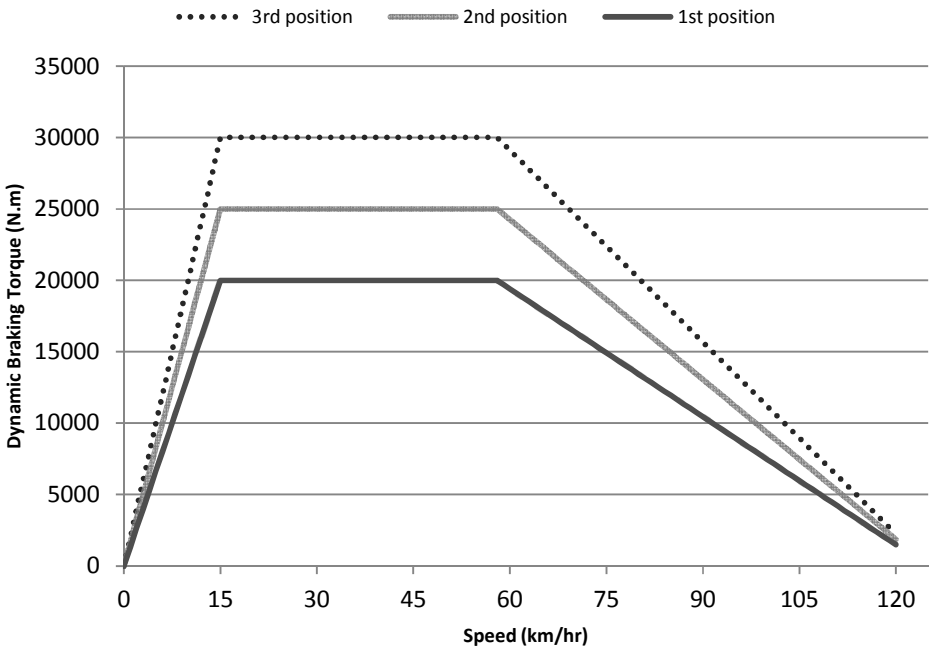

Figure 4.3 Assumed DC motor dynamic braking torque for model simulation.

In the model comparison and the parametric study, only DC traction motors will be considered to estimate the train braking distance.

4.2.4 Air Brake

The air brake is applied at each wheelset, for the locomotive and the freight cars, as a braking torque. Since this type of braking applies friction force on the wheelset, applying it at high speed may cause heat damage to the wheelset. In all simulations (except slack model comparison), it is

assumed that it is applied at speeds less than 15 km/hr. It is increased gradually until maximum air braking of 5,000 *N.m* at a speed of 5 km/hr. It is then fixed until the train comes to a complete stop. In the simulation, the air brake is applied only when DC traction motors are used since its dynamic braking fades at low speeds. AC motors, on the other hand, provide very good dynamic braking at low speeds.

4.3 Coupler Slack Model Comparison

The dynamic train model developed earlier is simulated with and without coupler slack, using the coupler force equations stated in Chapter 3. In the simulations, the coupler slack length is 3 cm ($1\frac{1}{8}$ in) . DC traction motors are considered, loaded railcars are used, and the dynamic braking is fixed at the second position. The initial speed is 54 km/hr. For this specific comparison, it is assumed that air brakes are applied at a speed less than 22 km/hr, and it is gradually increased until it reaches a maximum of 5,000 *N.m* at a speed of 12 km/hr. It is then kept constant until the train comes to a complete stop. The results are compared with the train model in which the coupler slack is ignored. Figure 4.4 shows the distance traveled for both cases. The difference is about 2.0 m (or 1%) in distance, with the slack causing a slightly larger braking distance. Figure 4.5 shows the train speed for both cases. In the first case, the slack action response causes a deviation to the speed that is further highlighted in Figure 4.5. The deviation is caused by the inter-train dynamic forces caused by the coupler slack (or deadband) when a change in force state (going from traction to braking) occurs. Because the two responses are nearly identical, the train model without coupler slack will be considered in all simulations later in order to reduce the computational time required for the models.

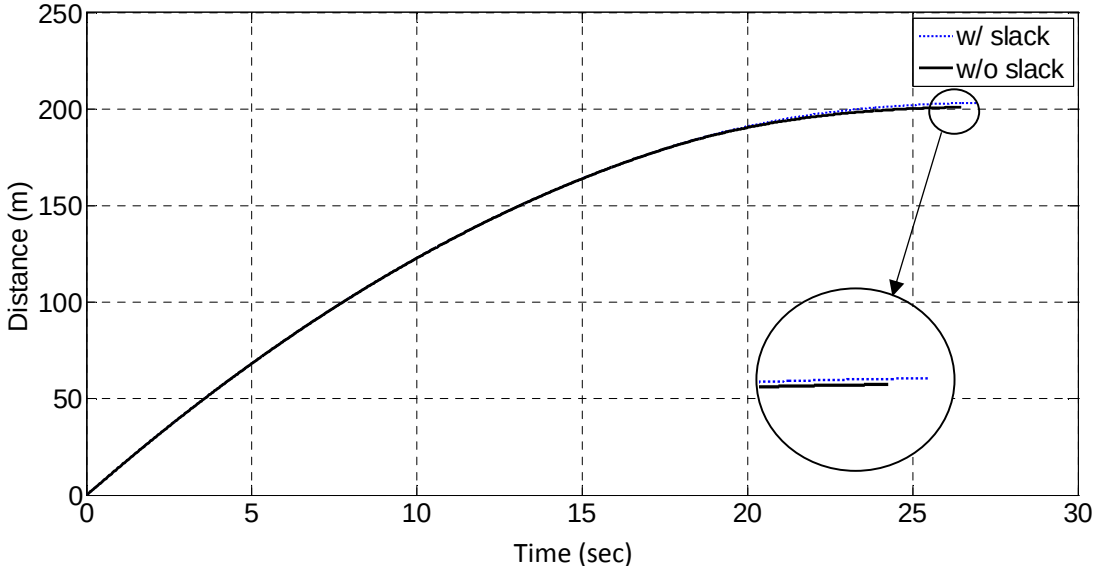

Figure 4.4 Distance travelled by the train for cases with and without coupler slack.

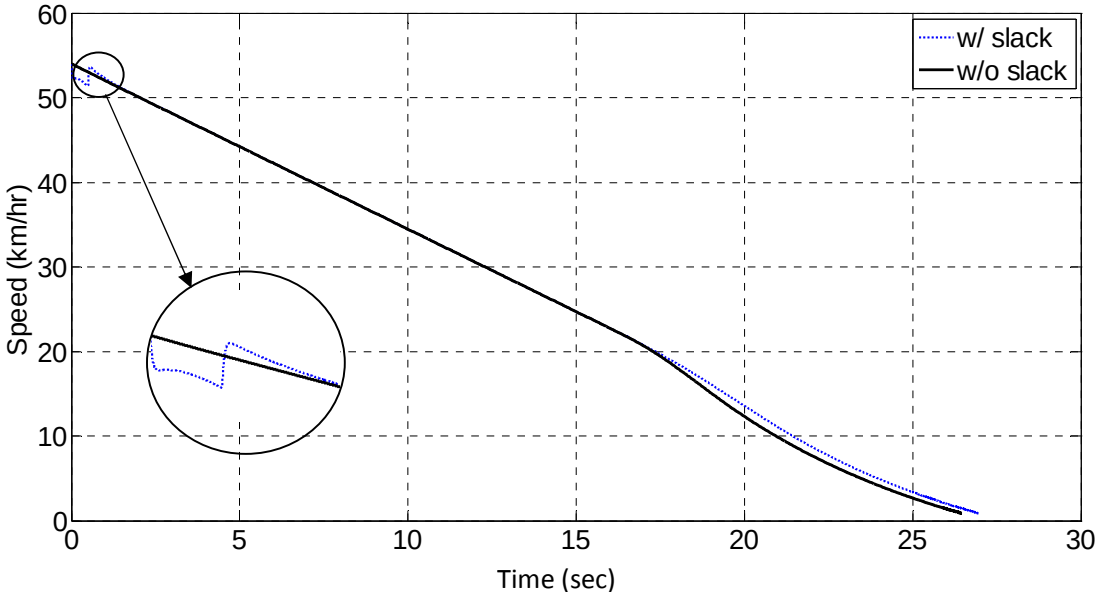

Figure 4.5 Train speed for cases with and without coupler slack.

4.4 Model Verification

To verify the dynamic equations, SIMPACK is used to simulate three railcars as shown in Figure 4.6. Loaded railcars are used, and the dynamic braking is fixed at the first position using DC traction motors to bring the train to a stop from 72 km/hr. The first car is the locomotive with six wheelsets, and the other railcars have four wheelsets each. All are connected with

simple couplers. Furthermore, all primary and secondary suspensions, and the propulsion resistance are included in this model.

Figure 4.7 shows the air brake model in SIMPACK where the air brake is applied at 15 km/hr (4.17 m/s), gradually increased to 5000 N.m at 5 km/hr (1.39 m/s), and kept constant until the train stops. Figure 4.8 shows the dynamic braking model in SIMPACK where it is fixed in the first position. In Figure 4.9, the simulation results show the distance travelled and the train speed versus time. The stopping distance is 489 m. The same operating conditions are used when simulating the model discussed earlier in Matlab. Figure 4.10 shows that the train has travelled a distance of 493 m, for an error of less than 1% between the two simulation models. It is suspected that the small error is due to slightly different wheel/rail contact mechanics in SIMPACK, compared to Kalker's empirical model that was adopted in the developed model.

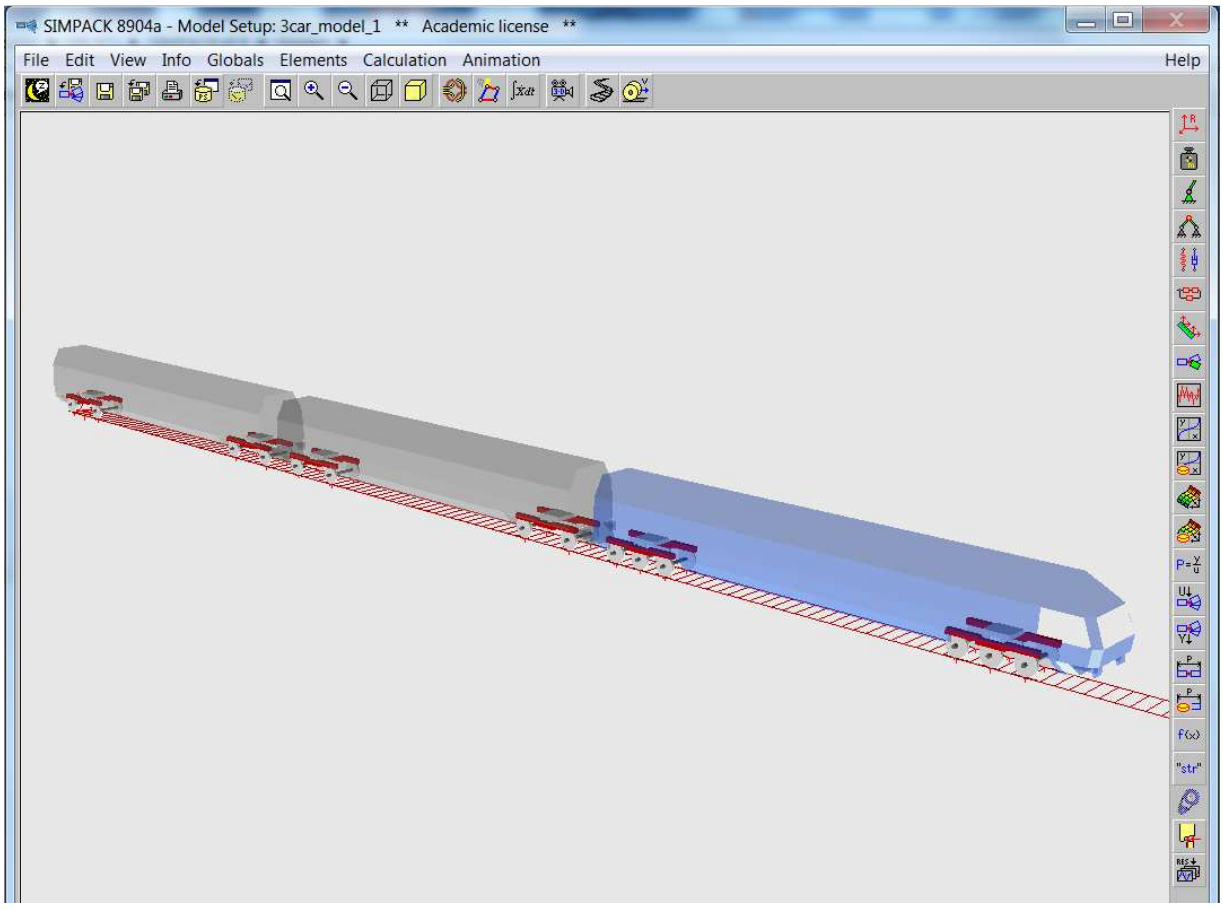

Figure 4.6 Three-railcar train model in SIMPACK.

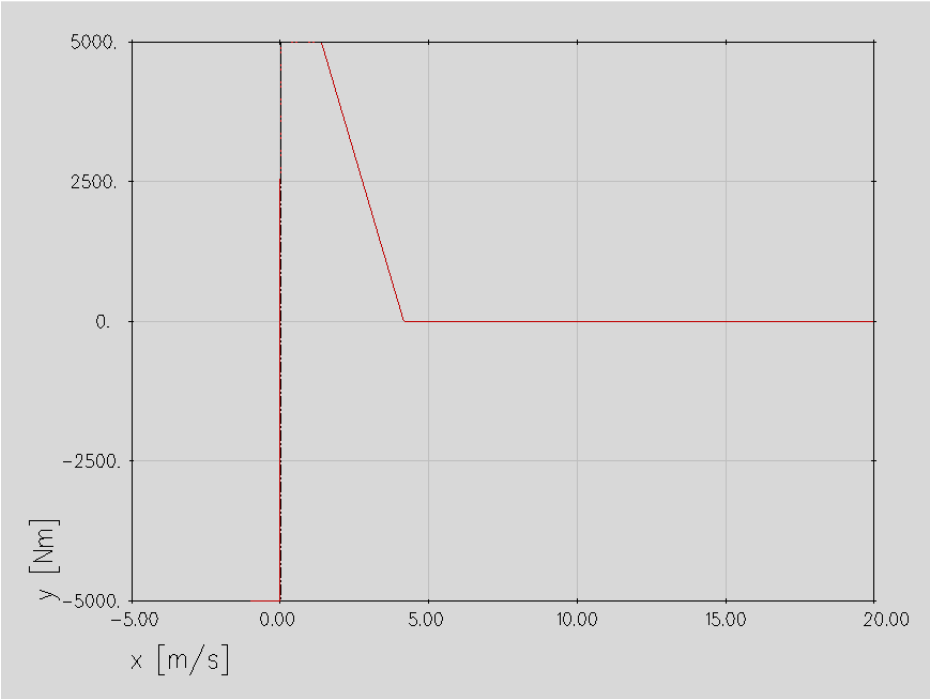

Figure 4.7 Air brake model in SIMPACK.

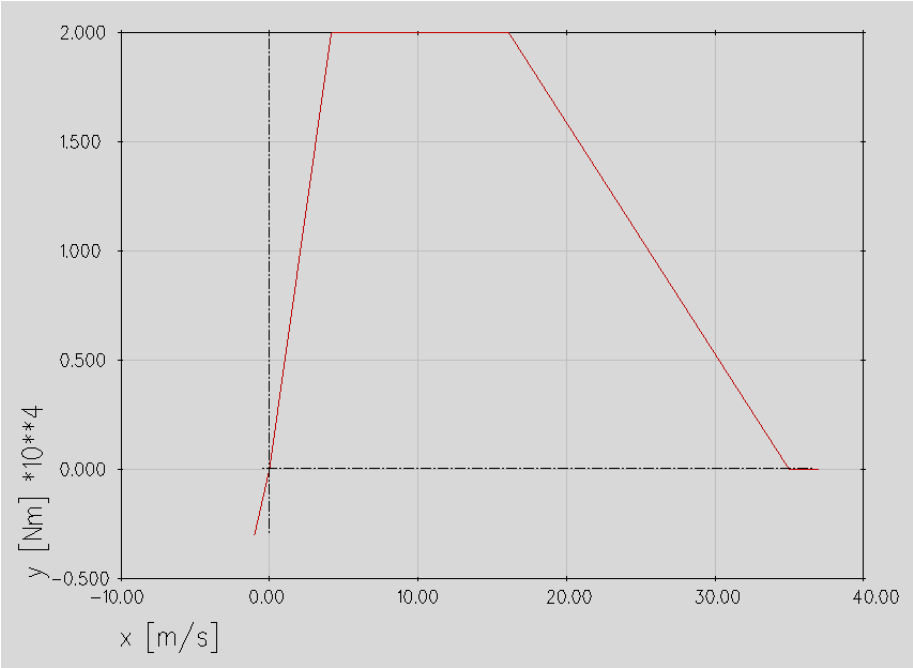

Figure 4.8 Dynamic braking model in SIMPACK.

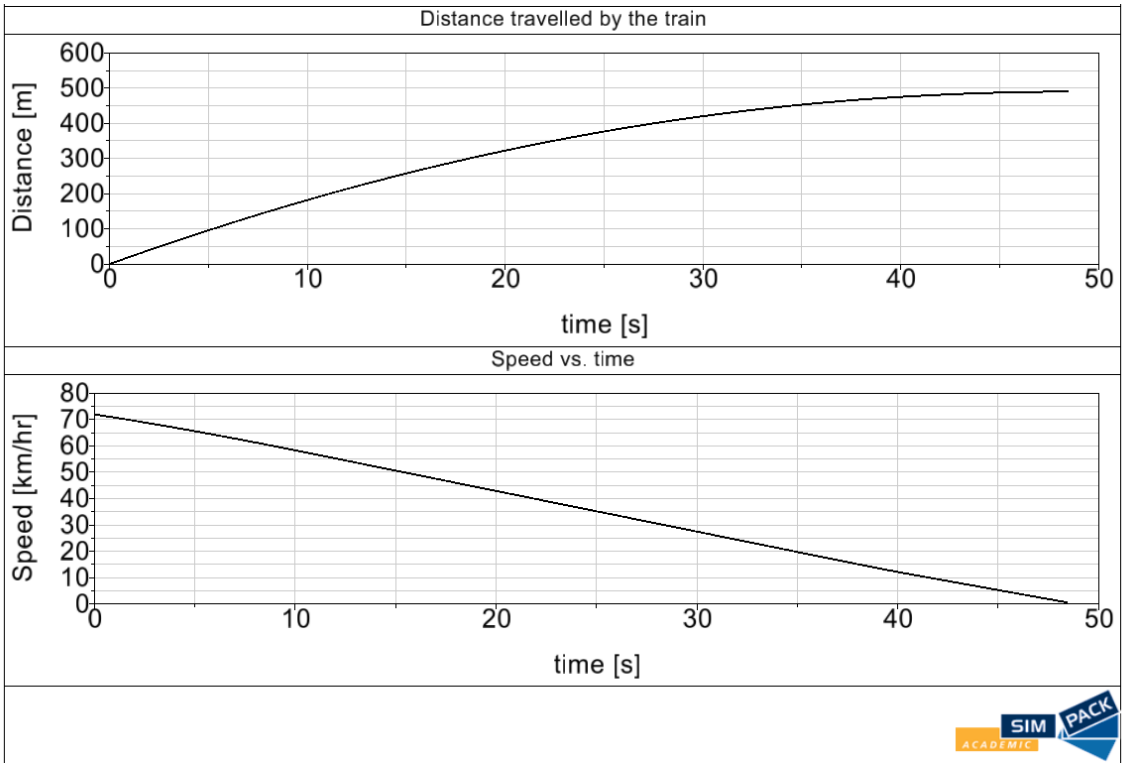

Figure 4.9 Distance travelled and speed versus time from SIMPACK.

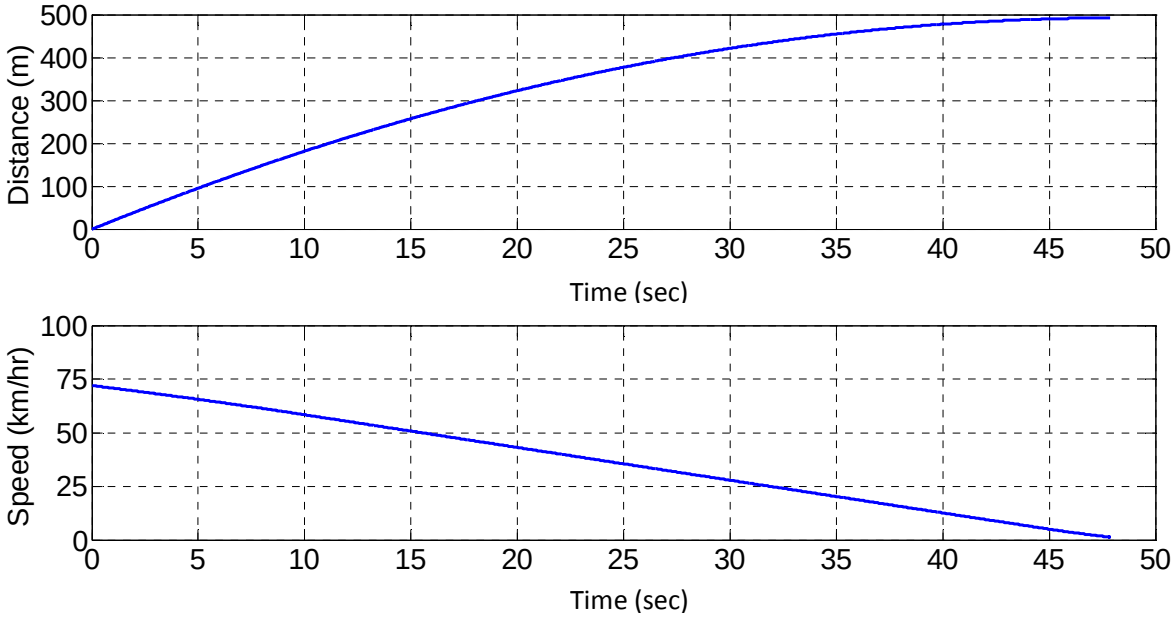

Figure 4.10 Distance travelled and speed versus time from Matlab.

4.5 Parametric Study

Matlab is used to solve all the equations with a maximum time step of 0.001 second. All assumptions and initial conditions will be stated under each case for different weights, dynamic braking efforts, initial speeds, aerodynamic drag forces, and wheel/rail adhesion condition. For the purpose of the parametric study, the dynamic braking is fixed at an assumed position for each simulation. The dynamic braking is applied after one second of the simulation to determine how the system behaves before and after the application of the brake. The delay also represents the delay in applying the dynamic brakes by the train engineer. Additionally, the torque is applied gradually such that a quarter of the torque amount is increased in each second until the total braking torque for the initial speed is applied at the end of the fifth second.

4.5.1 Different Weights

Two different weight conditions for the railcars are used in the simulation: empty freight cars and loaded freight cars (see Table 4.1). The locomotive mass is fixed, m_1 = 190,500 kg. The dynamic braking is fixed at the 2nd position, and the initial speed is 54 km/hr. Figure 4.11 shows the distance travelled by the train versus time. In the case of the loaded freight cars, the train needs 258 m distance to stop, while in the case of the empty freight cars, the train needs 197 m distance to stop. The more weight the railcars have, the longer the distance and the time that are needed by the train to stop. The corresponding speed versus time relationships are shown in Figure 4.12.

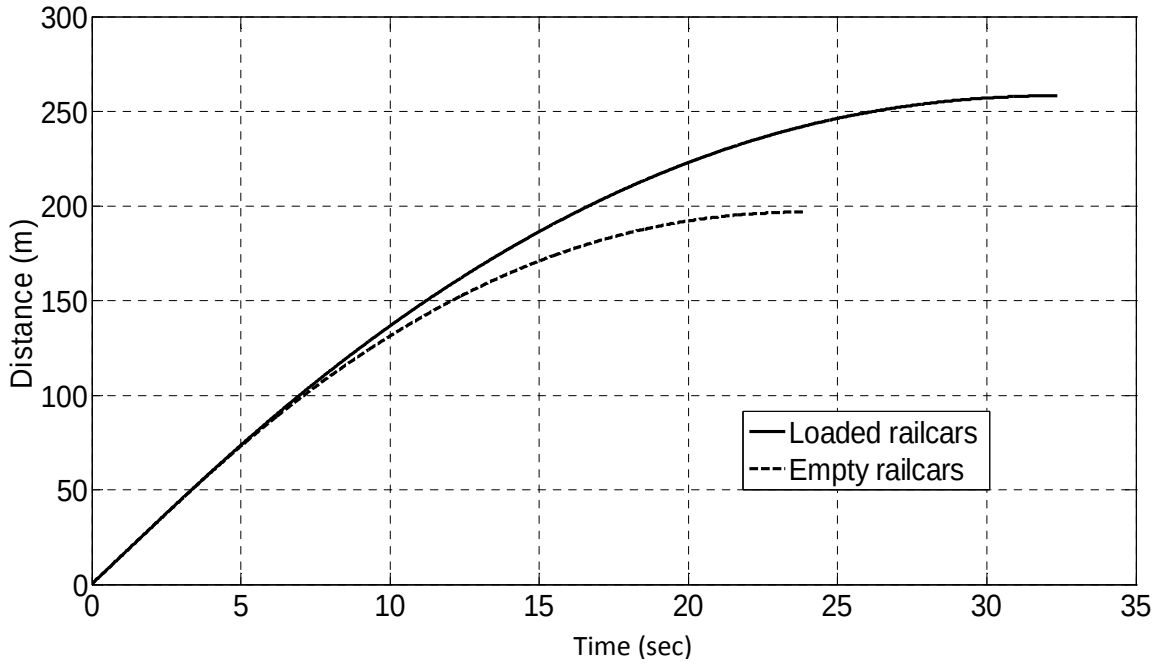

Figure 4.11 Distance travelled by the train for different weight conditions.

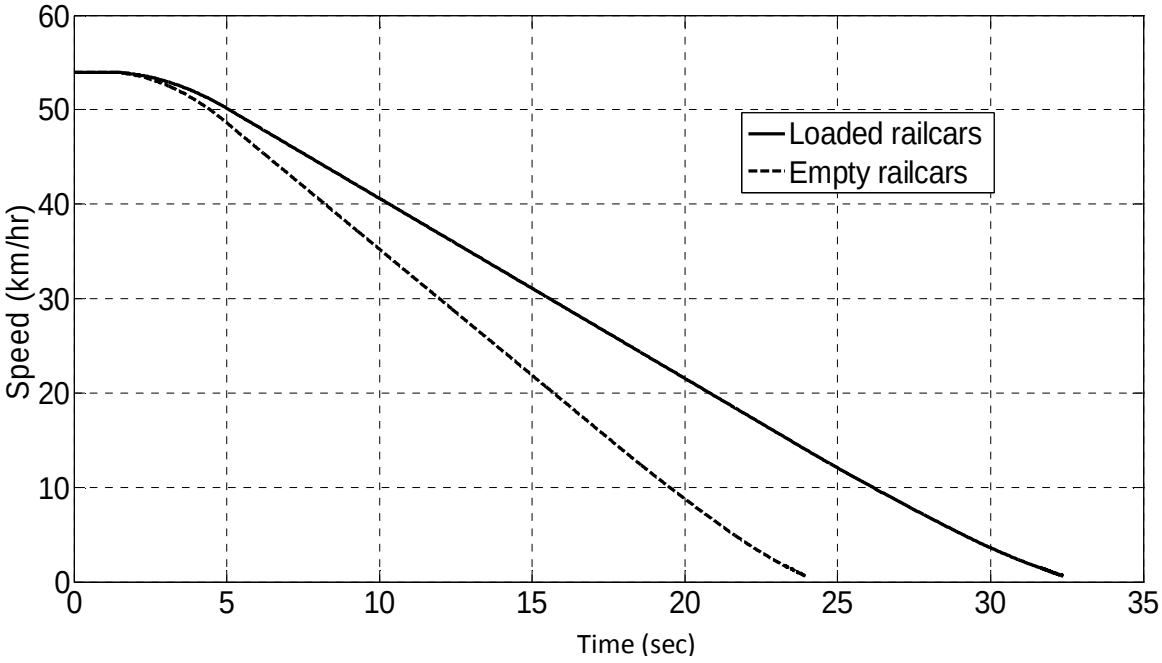

Figure 4.12 Speeds versus stopping time for the train for different weight conditions.

4.5.2 Different Dynamic Braking Efforts

The three different dynamic braking positions are used in the simulation for loaded railcars with an initial speed of 54 km/hr, as per Figure 4.3. Figure 4.13 shows the distance traveled by the train using the three dynamic braking positions defined earlier. Notice that the more dynamic braking is applied, the less distance is traveled by the train. The dynamic brake plays an important role in the travelled distance needed for a train to come to a complete stop. The speeds for these conditions are shown in Figure 4.14.

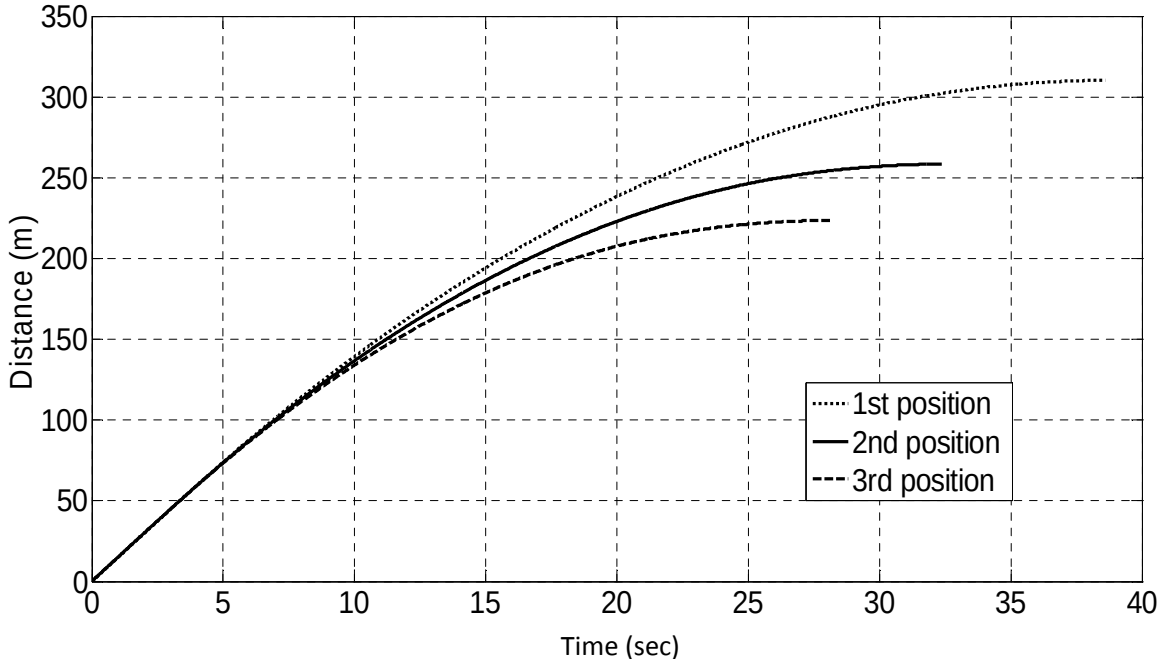

Figure 4.13 Distance traveled by the train for different braking forces.

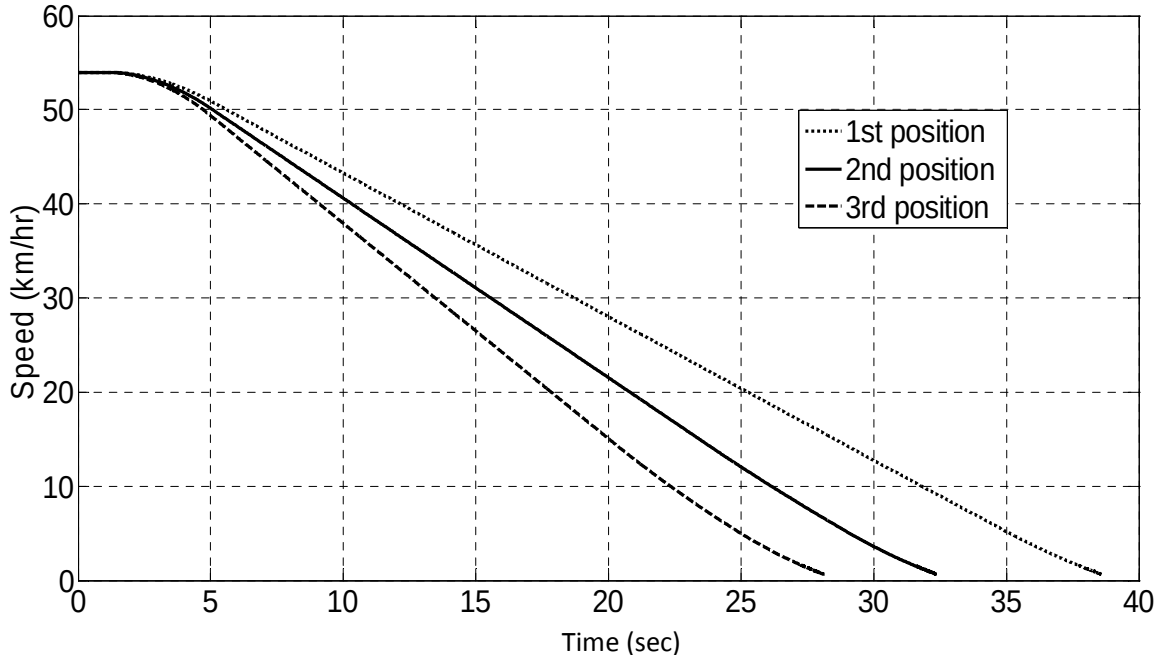

Figure 4.14 Speeds versus time for the train for different braking forces.

4.5.3 Different Initial Speeds

Changing the initial speed significantly affects the stopping distance since it depends on the dynamic braking provided at that speed. In this simulation, loaded railcars are used. Also, the dynamic braking is fixed at the 2nd position. Figure 4.15 shows the speed versus time plots for different initial conditions. In Figure 4.16, we can see that the difference between distances traveled for the 90 km/hr case and the 72 km/hr case is larger than the difference between distances for 72 km/hr and 54 km/hr cases.

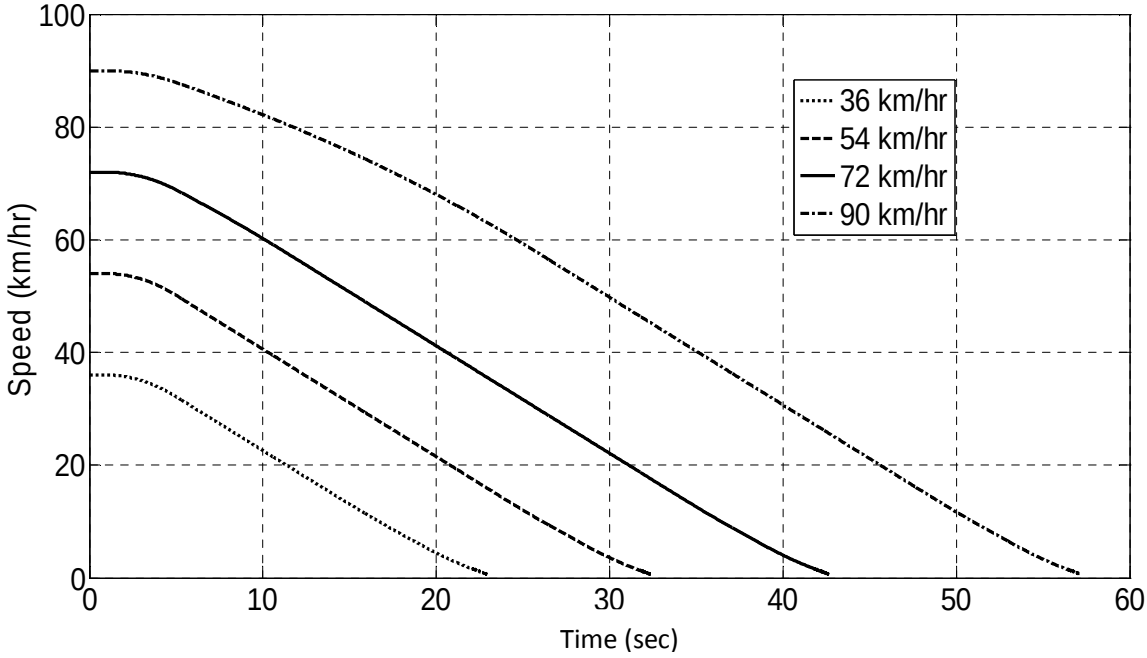

Figure 4.15 Speeds versus time for the train for different initial speeds.

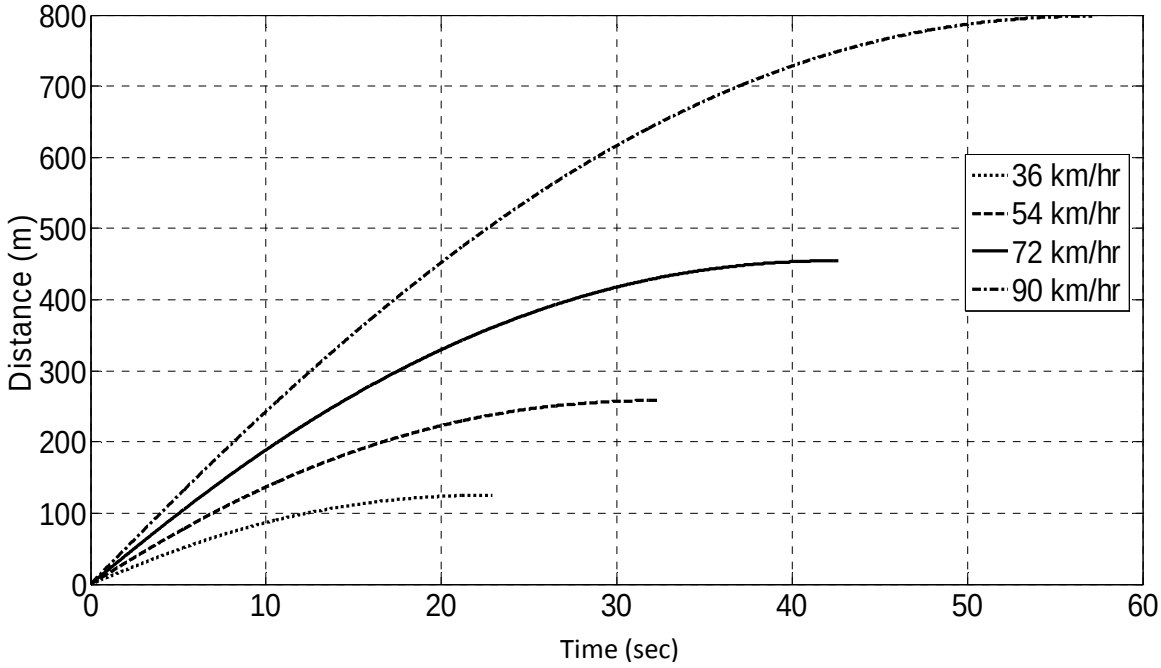

Figure 4.16 Distance travelled by the train for different initial speeds.

4.5.4 Aerodynamic Drag

The model is exercised with and without aerodynamic drag forces to determine the difference in the distance travelled by a train. The simulation is run for an initial speed of 90 km/hr. The dyanmic braking is set to the 2nd position, and loaded railcars are considered. Figure 4.17 shows the difference between the distance travelled by the train with and without aerodynamic drag forces. The stopping distance for the case that includes the aerodynamic drag is about 2 meters shorter than the case with no aerodynamic drag. This means that aerodynamic drag does not have a significant effect on freight trains since they do not run at high speeds.

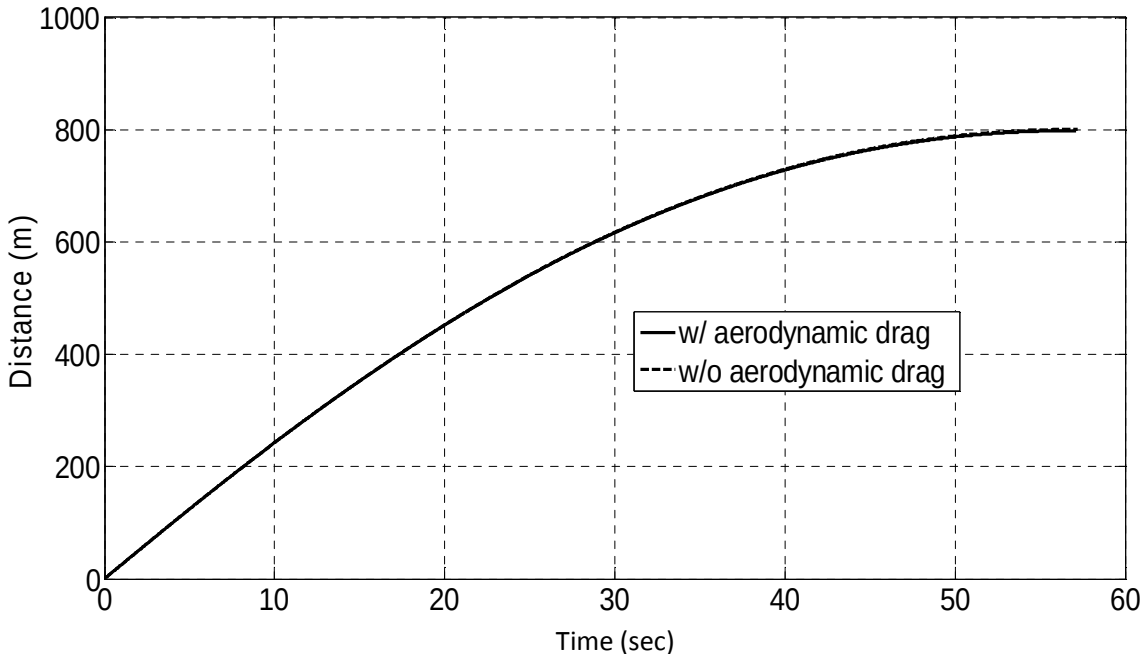

Figure 4.17 Distance travelled by the train with and without aerodynamic drag.

4.5.5 Wheel/Rail Condition

The wheel/rail condition is very important to consider before applying dynamic braking in order to avoid wheel lockup. Dividing the longitudinal creepage force by the wheel load yields the normalized creepage force, which can easily be related to the wheel lockup condition as:

$\frac{F_{cr}}{\mu N} \geq 1$ wheel lockup

$\frac{F_{cr}}{\mu N} < 1$ wheel rolling condition

where N is the normal force and μ is the static friction coefficient. Let's assume a case where the friction coefficient is fixed at 0.4, the initial speed is at 54 km/hr, and the railcars are loaded. It is assumed that the dynamic braking position is fixed in each simulation. Figure 4.18 represents the normalized creepage force with time at the first wheelset. We can see that the dynamic braking positions can be applied safely under this adhesion condition. However, if the wheel/rail adhesion condition is poor (i.e., wet, icy, or oily rail surface), wheel lockup must be considered when applying dynamic braking, since the coefficient of friction is reduced. Let's assume a second case where the friction coefficient is fixed at 0.2 with the same initial speed and weights. As shown in Figure 4.19, the third position of dynamic braking results in normalized creepage force that is close to unity. The maximum normalized creepage is about 0.78 when applying the 2nd position braking, which means that the 2nd position dynamic braking can minimize the stopping distance safely. The amount of dynamic braking force should be chosen carefully depending on the wheel/rail adhesion condition. Notice that the normalized creepage force responds quickly in the first few seconds. This is because dynamic braking is gradually applied to the wheelsets.

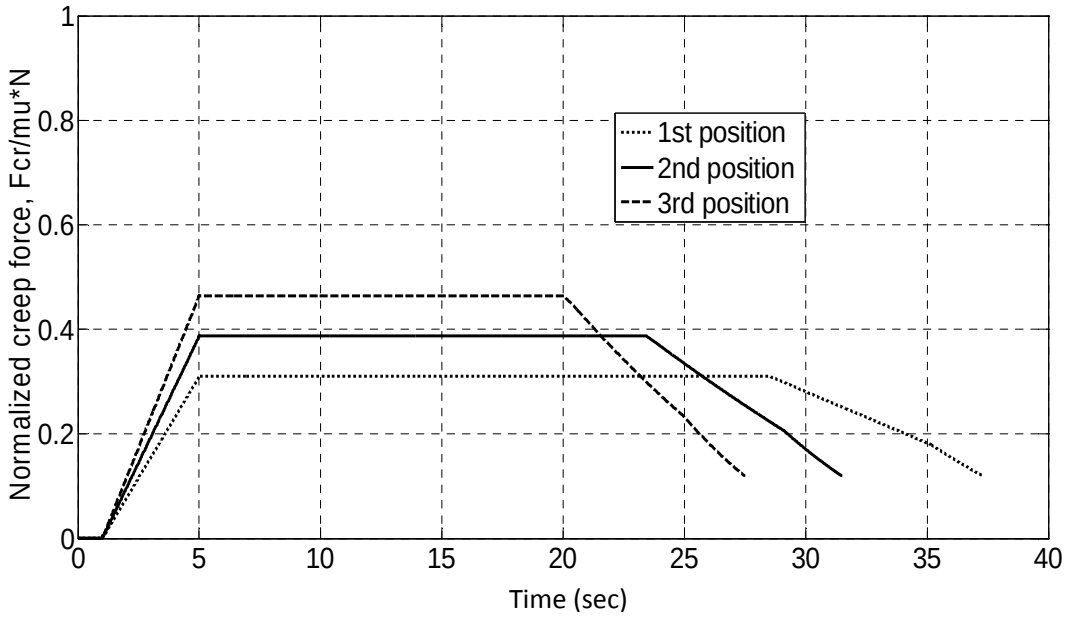

Figure 4.18 Normalized creepage force using different braking forces for *μ=0.4*.

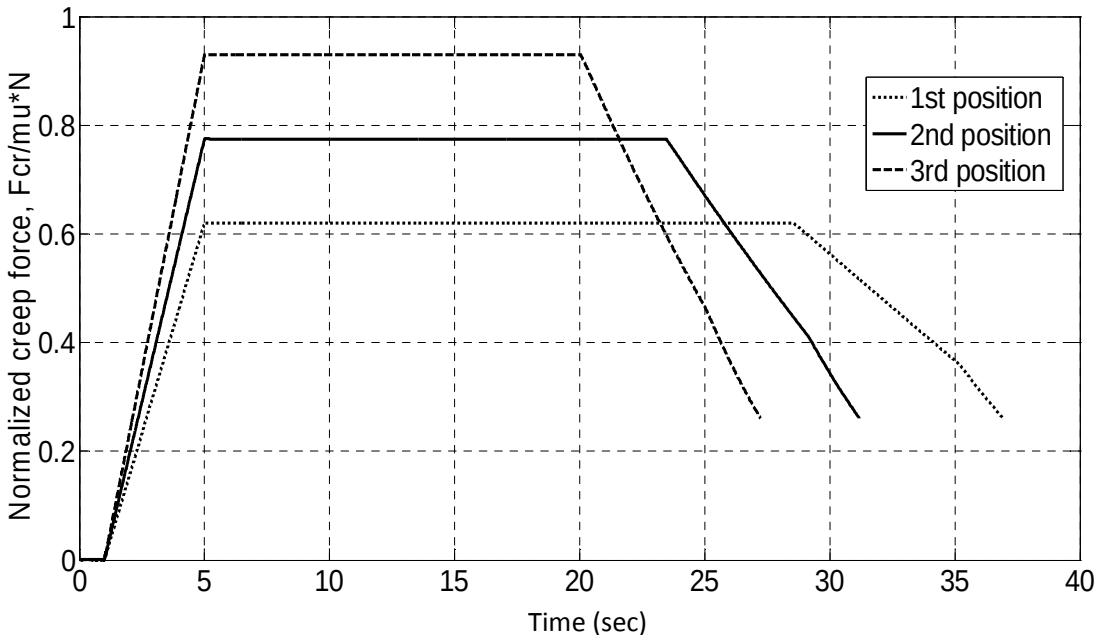

Figure 4.19 Normalized creepage force using different braking forces for μ=0.2.

4.5.6 Number of Railcars

The developed model can easily be used for different numbers of railcars. Loaded railcars are considered in the simulations with initial speed of 54 km/hr. It turns out that adding more railcars has a significant effect on the stopping distance of a train. Figure 4.20 shows the distance travelled for three, five, and eight railcars; the dynamic braking is fixed at the second position. The stopping distance is about 258 m for a train consisting of three cars, 378 m if five cars are considered, and 555 m for a train consisting of eight cars.

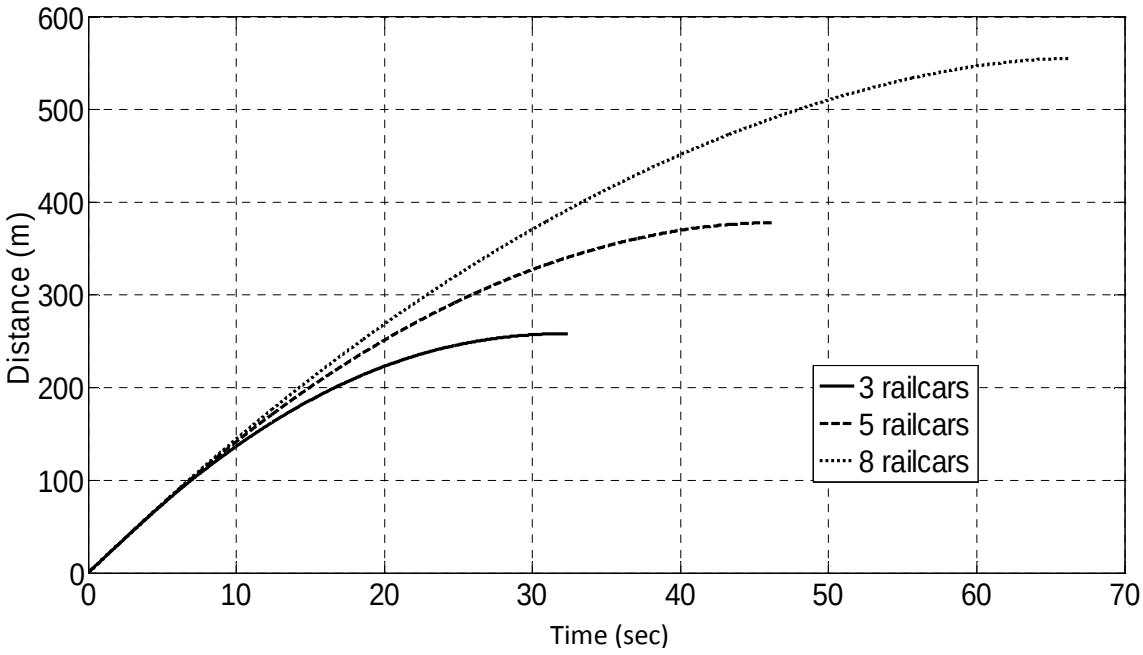

Figure 4.20 Distances travelled by a train with three, five, and eight railcars.

Chapter 5

MRAC of Dynamic Braking Forces

5.1 Introduction

This study augments the adhesion control systems that are used in the railroad industry. Most of the current adhesion control algorithms use variations of proportional-integrative-derivative (PID). The MRAC method suggested in this study provides a more advanced method of allowing the traction motors to deal with the dynamic variations that can occur during train operation. In this control method, the dynamic braking force is controlled so that the system output can imitate the reference model. The reference model is designed based on multiple factors.

In this chapter, the MRAC is applied to the train model to control the dynamic braking forces while preventing wheel lockup and excessively large coupler forces. First, the train system model used for control purposes will be described. Then, the MRAC system and the method developed to apply it to the train system output will be presented. All required coefficients, constants, and assumptions will be stated. Both DC and AC traction motors will be considered. Motor torque will be controlled by adjusting the current in DC motors, and electrical excitation frequency in AC motors. Random adhesion coefficients will be considered to evaluate the performance of MRAC.

5.2 Train Model

The train model is shown in Figure 5.1, with one locomotive and three freight cars. The model is set up such that it can be used to investigate the three coupler forces between all units. The general equations of motion that were developed in Chapter 3 can be applied to this model. All required parameters and coefficients needed for solving the dynamic equations are as shown earlier in Table 4.1. Propulsion resistance, creep forces, and air brake are evaluated in Section 4.2.

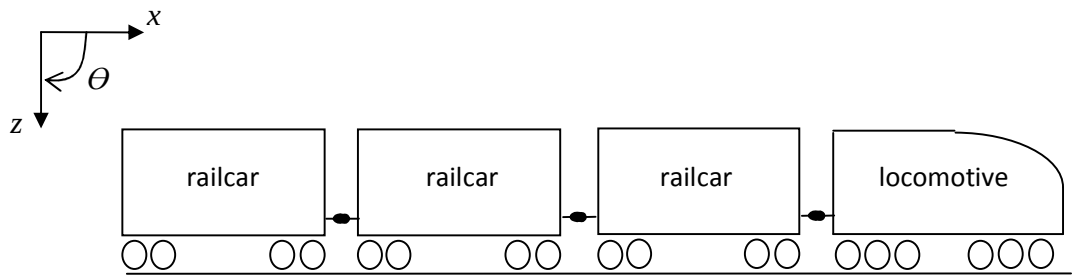

Figure 5.1 Four-railcar train model.

5.3 Control Model

In this section, we will describe MRAC model. First, the available dynamic braking for both AC and DC traction motors will be discussed, and then the control strategy and MRAC system will be described.

5.3.1 Dynamic Braking

As mentioned previously, dynamic braking is only applied at the locomotive since it is the only unit with traction motors. The total dynamic braking force depends on the number of traction motors, the amount of electrical current or excitation in the motors, and train speed. It is assumed that the locomotive has six traction motors (a traction motor on each wheelset) that can be controlled independently of each other. The gear ratio for Siemens locomotive, which will be assumed for both AC and DC motors, is 1:5.19 [28].

5.3.1.1 AC Motors

In AC motors, the applied torque is limited by the power provided by the motor at high speeds, and is limited by the motor voltage at low speeds, as shown previously in Figure 2.13 for an SD90MAC locomotive with 4300 hp. Looking at the braking force plot where the force changes from constant to a curve, we can compute the maximum power at each axle as

$$P_{max} = \frac{\dfrac{510{,}000\ N\ \times 27000\,\frac{m}{\text{hr}}}{3600\,\frac{sec}{\text{hr}}}}{6\ axles} = 638\ \text{kW}$$

which gives the same maximum power that can be provided by the motor as in [28]. This means that for each axle, the maximum continuous braking torque that can be provided at each axle is

$$\tau_{db,max} = \frac{510{,}000\ N\ \times\ 0.5\ m}{6\ axles} = \ 43\ kN.m$$

where 0.5 m is the wheel radius. To calculate the maximum braking torque at each axle for high speeds (greater than 27 km/hr),

$$\tau_{db} = \frac{P_{max}\ (\mathrm{W})}{\omega_{ws}\ (rad/s)} \tag{5.1}$$

Figure 5.2 shows the calculated braking torque based on the available information for an SD90MAC locomotive with AC traction motors. Note that if 43000 N.m is divided by the gear ratio, 5.19, it gives 8258 N.m, the maximum motor torque.

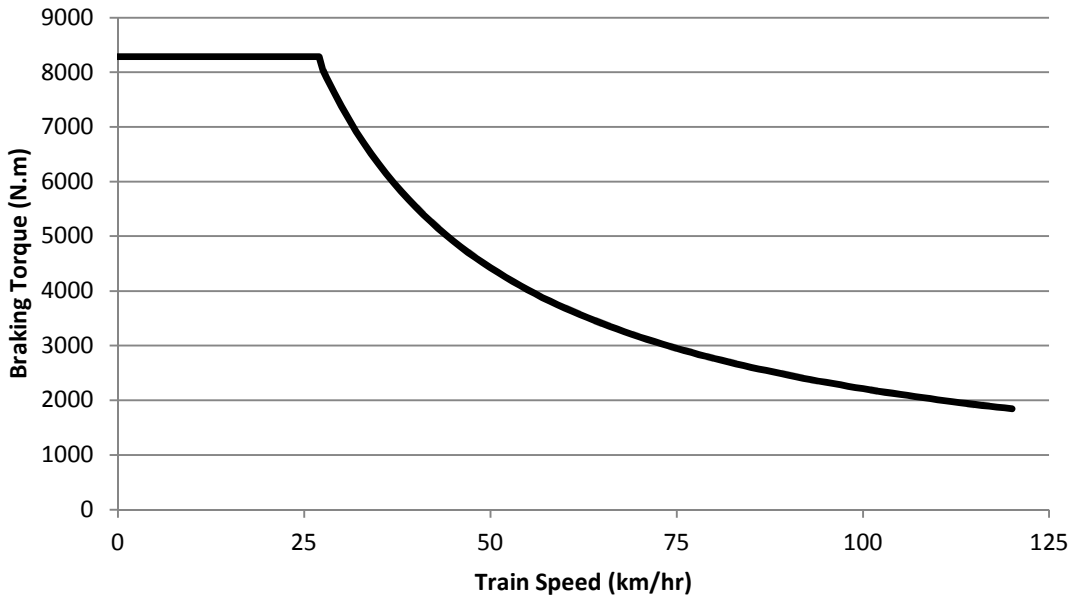

Figure 5.2 Available torque for each AC motor in Siemens SD90MAC.

As mentioned previously in Section 2.3.2.2, the continuous braking torque is applied at a very small slip ratio, where the torque-slip relationship is linear. Using Figure 2.12, we assume a maximum slippage of 5% to reach the maximum continuous braking torque. Figure 5.3 shows a linear relationship between the motor torque and slip ratios that are less than 5%. The maximum motor torque is 8258 N.m at a 5% slip ratio. The slippage is a function of rotor speed frequency and the electrical excitation frequency of the motor. The rotor speed frequency can be measured by a wheelset speed sensor while considering the gear ratio. In the control model, knowing dynamic braking allows one to determine the slip ratio (from Figure 5.3) and the electrical excitation frequency.

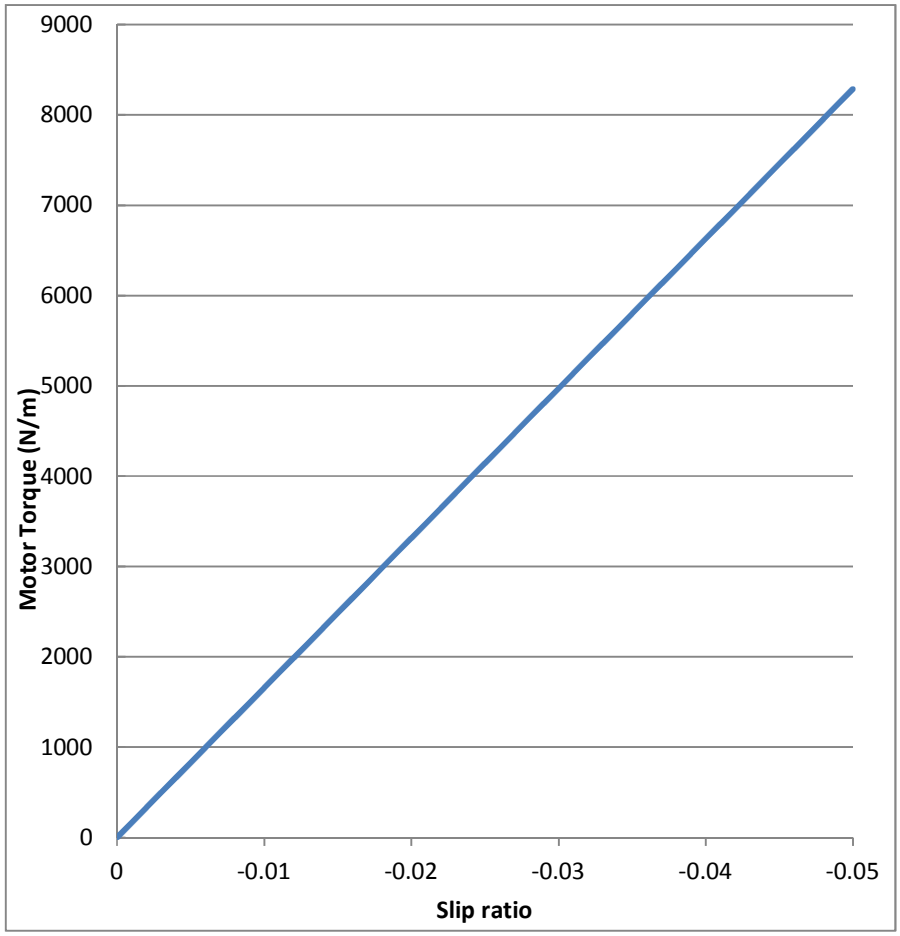

Figure 5.3 Linear relationship between motor torque and very small slip ratios.

5.3.1.1 DC Motors

The braking torque that is applied by a DC motor is directly proportional to the current that is provided to the traction motors, as expressed in Equation (2.14) where motor torque constant, k_t, is assumed to be 15 for the simulations. Additionally, the motor current is limited according to the traction motor design characteristics. In Figure 5.4, three regions are shown. The first and third regions are commonly referred to as "voltage limited." The middle region is referred to as "current limited." The voltage-limited region includes low train speeds at which the armature rotational speed generates currents far below the maximums tolerated by the motor. It also includes very high train speed in which the currents are intentionally kept low (inversely proportional to the train speed) to insure that the high armature speed does not cause braking torques that are too large to be tolerated safely by the motor's mechanical components. The current limited region represents moderate speeds at which the currents are maxed out by the maximum current that can be passed through the motor without any detrimental effects on the traction motor. In Figure 5.4, note that the maximum current is 552.3 Amps. If this is multiplied by the motor torque constant, 15, and the gear ratio, 5.19, the result is 43 *k*N.m, which is the maximum continuous motor torque assumed.

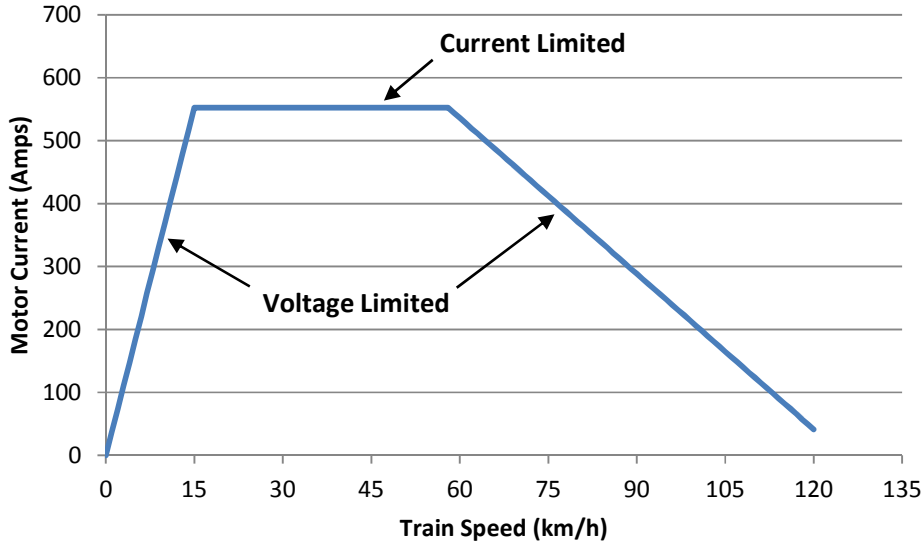

Figure 5.4 Maximum allowable current supplied to the traction motors at different train speeds.

5.3.2 Control Strategy

Two measurable values will be used in the control strategy: the rotational speed of each wheelset, and the actual forward speed of the wheelset. As mentioned in Section 2.2, these are important for calculating the longitudinal creepage, which can be expressed as

$$\xi_x = \frac{V_{ws} - R_{ws}\omega_{ws}}{V_{ws}} \tag{5.2}$$

where V_{ws} is the actual forward speed of the wheelset, ω_{ws} is the rotational speed of the wheelset, and R_{ws} is the wheel rolling radius. Simulations are run for fixed wheel/rail adhesion coefficients in order to study the relationship between the creepages, the applied braking torque, and the normalized creep force. In the simulations, the weight of the locomotive is assumed to be 190,500 kg, and the dynamic braking torque is applied until slipping occurs. Figure 5.5 shows the applied braking torque versus creepage for different values of wheel/rail adhesion coefficients. Note that the higher the adhesion coefficient allows more braking torque to be applied before the wheel starts to slip.

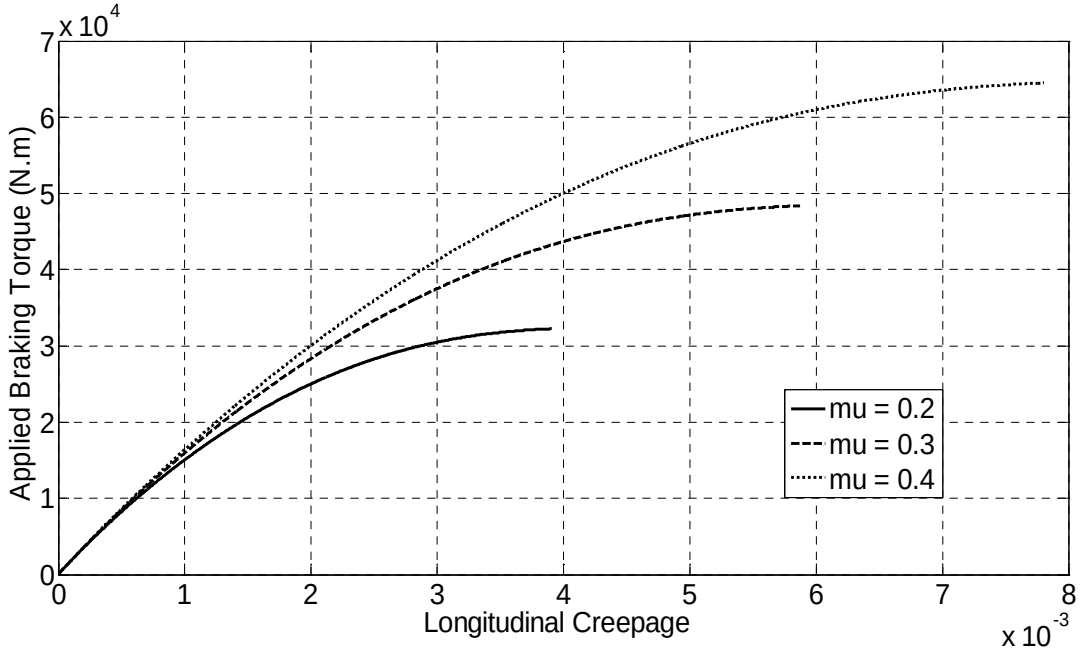

Figure 5.5 Dynamic braking torque versus longitudinal creepage for different wheel/rail adhesion coefficients.

Figure 5.5 implies that the slope of each plot decreases as the braking torque increases, with wheel slippage starting at zero slope. The slope equation can be calculated as

$$S_T = \frac{d\tau_{db}}{d\xi_x} \quad (\text{N.m}) \tag{5.3}$$

where S_T defines the torque/creep ratio. The normalized creep force versus torque/creep ratio is then plotted for the three different wheel/rail adhesion conditions in Figure 5.6. The three plots give almost identical results, indicating that the normalized creep force is independent of the adhesion coefficients during dynamic braking for that specific weight of the locomotive. However, if different locomotive weights are used, the relationship results in different plots as shown in Figure 5.7 for three different locomotive weights. The plot shows that for heavier locomotives, a larger normalized creep force can be generated at a given torque-creep ratio.

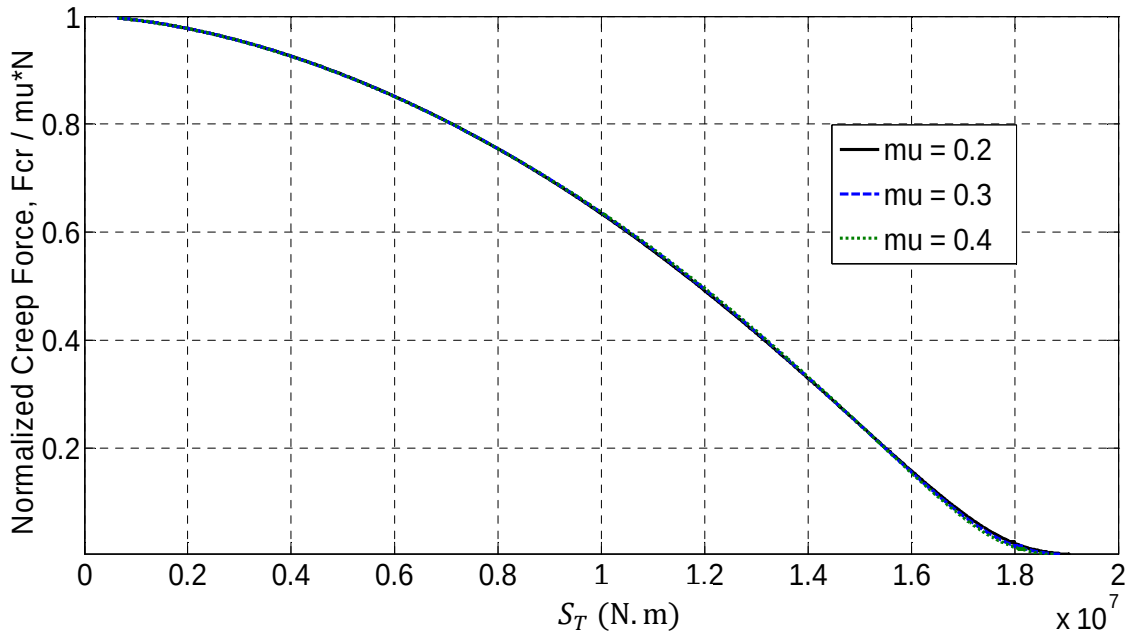

Figure 5.6 Normalized creep force versus torque-creep rate for different wheel/rail adhesion coefficients.

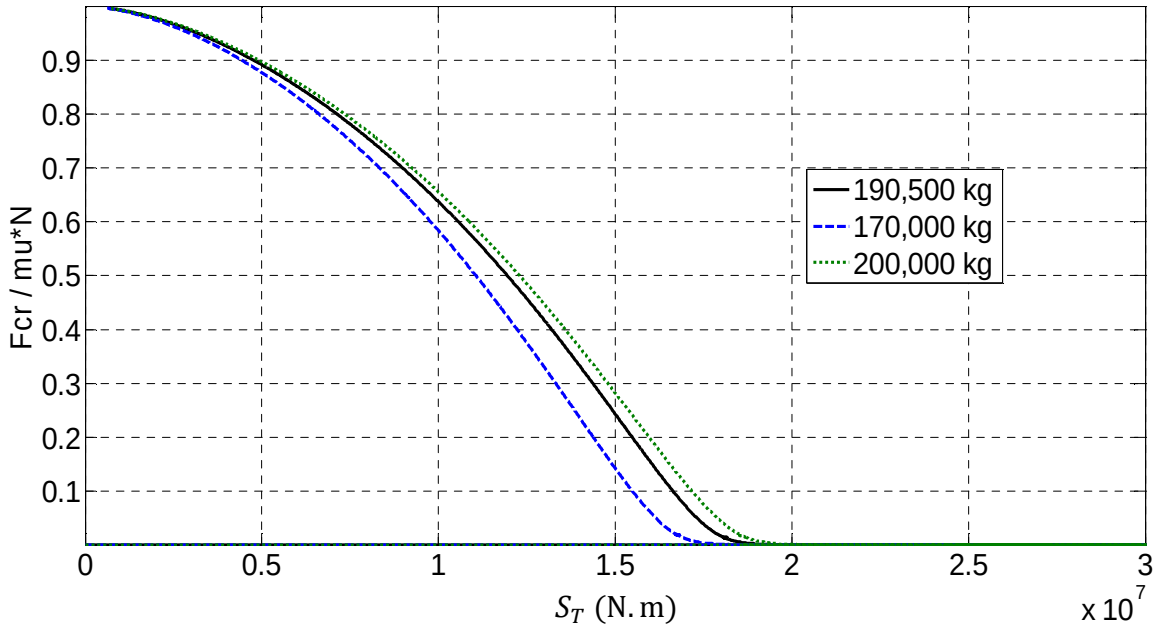

Figure 5.7 Normalized creep force versus torque-creep rate for different locomotive weights.

N can be divided by S_T and a new relationship is established, where N/S_T can be defined as the normal-load-torque-creep ratio. Figure 5.8 shows the normalized creep force versus N/S_T for the 190,500 kg locomotive under different wheel/rail adhesion conditions. This is repeated for the 190,500 kg locomotive to make sure that the plots give identical results if N/S_T is used. Figure 5.9 shows the normalized creep force versus N/S_T for different locomotive weights. The results are nearly identical, concluding that the normalized creep force, $F_{cr}/\mu N$, and N/S_T relationship can be used in the control model. In addition, the established relationship can be used if there is a change in the wheel/rail normal load because of weight transfer while braking or because of fuel weight reduction.

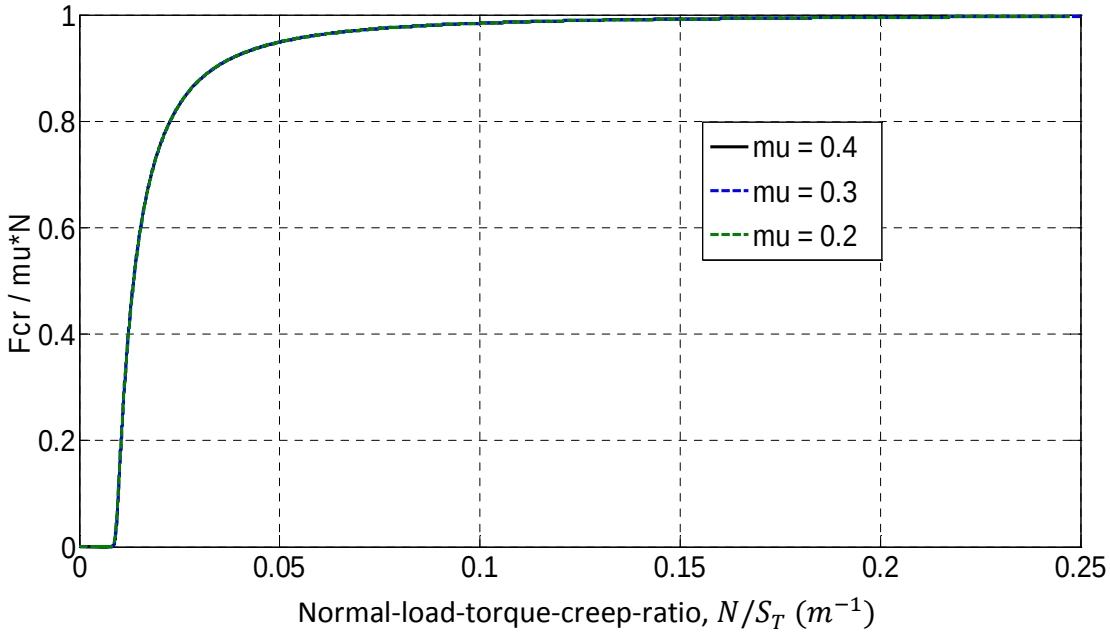

Figure 5.8 Normalized creep force versus N/S_T for different wheel/rail adhesion coefficients.

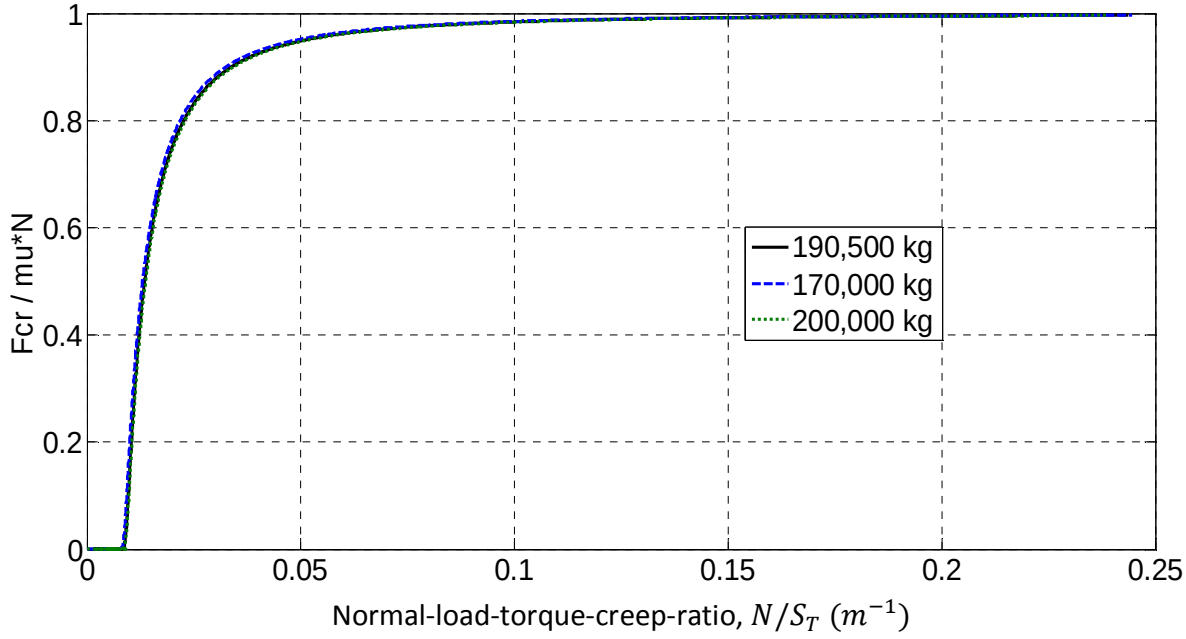

Figure 5.9 Normalized creep force versus N/S_T for different locomotive weights.

5.3.3 MRAC System

The system output that must be controlled is the normalized creepage force, $F_{cr}/\mu N$, which can be obtained from the established relationship in Figure 5.9 using the measurable value, N/S_T. The normalized creep force should not exceed 1 (or 100%) in order to prevent wheel lock-up. This is described in Equation (2.12). The control method can be applied to both DC and AC traction motors depending on what type of locomotive is used in the simulations. The purpose of this control is to adjust the current provided to the DC traction motors or the voltage excitation frequency of the AC traction motors such that the maximum allowable dynamic braking is achieved without locking up the wheels or generating large coupler forces that cause damage or derailment. This results in minimizing the stopping distance of the train within the limits of the wheel/rail conditions and the available torque from the traction motors.

Details of how MRAC is applied are described in Section 2.4, and Figure 5.10 shows the block diagram for MRAC for convenience. The output, y_p , represents the normalized creep force, y_m represents the reference model output, and u_c represents the desired values of the system output. First, the desired values for the reference inputs should be determined. Three factors must be considered to design the behavior of system output: adhesion coefficient, coupler forces, and available dynamic braking from the traction motors. Wheel/rail adhesion coefficients decrease at higher speeds, as shown previously in Figures 2.4 and 2.5. Increasing dynamic braking at high speed can result in high coupler forces. Gradually increased dynamic braking along with the decreasing train speed can prevent excessive coupler forces. Additionally, the amount of available dynamic braking that the traction motors can provide becomes lower at higher speeds. These factors are all speed-dependent. Based on these factors, the desired system output is designed as a function of train speed as shown in Figure 5.11. To include a small amount of design factor, the maximum value of the normalized creep force is selected to be 0.75 as opposed to 1, which is theoretically achievable.

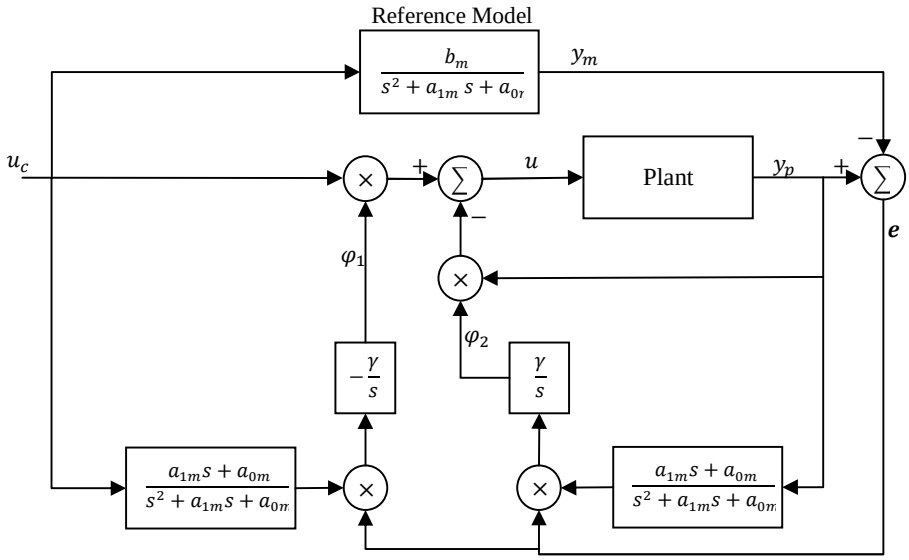

Figure 5.10 Block diagram of MRAC applied to a system [8].

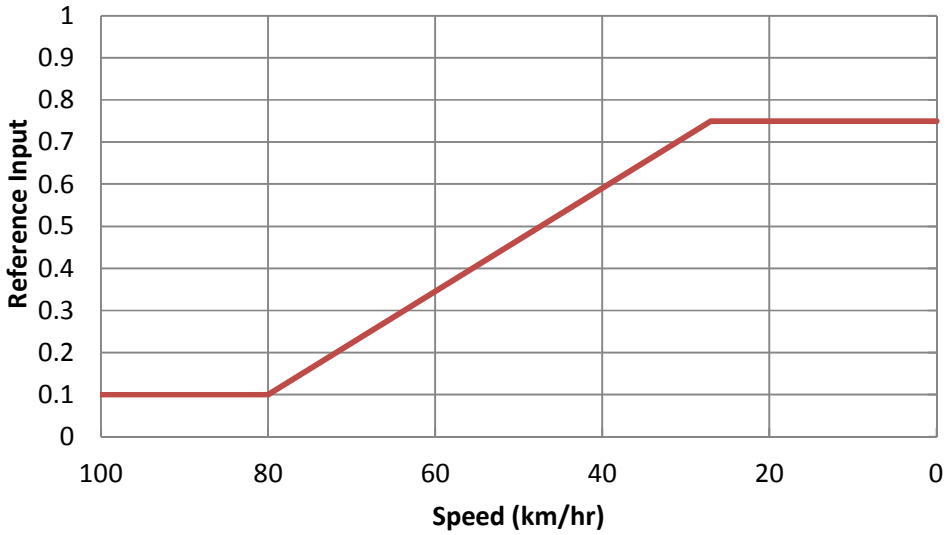

Figure 5.11 Desired values of the normalized creep force versus train speeds.

Now, the reference model characteristics must be determined. In order to design the reference model, it is assumed that $a_{1m} = 2\zeta/\omega_n$ and $a_{0m} = b_m = 1/\omega_n^2$. Three different characteristics are considered and simulated to investigate the reference model response: (a) $\omega_n = 1$ and $\zeta = 0.7$, (b) $\omega_n = 5$ and $\zeta = 0.7$, and (c) $\omega_n = 1$ and $\zeta = 0.3$. The results are shown in Figure 5.12 for high speeds, and in Figure 5.13 for moderate speeds. Note that the

second model results in the best response with a negligible overshoot. The second model allows the reference model output to have results similar to the desired reference input. This is chosen for all subsequent control model simulations. As shown in the control diagram, the control model gains are based on the error between the reference model output and the system output.

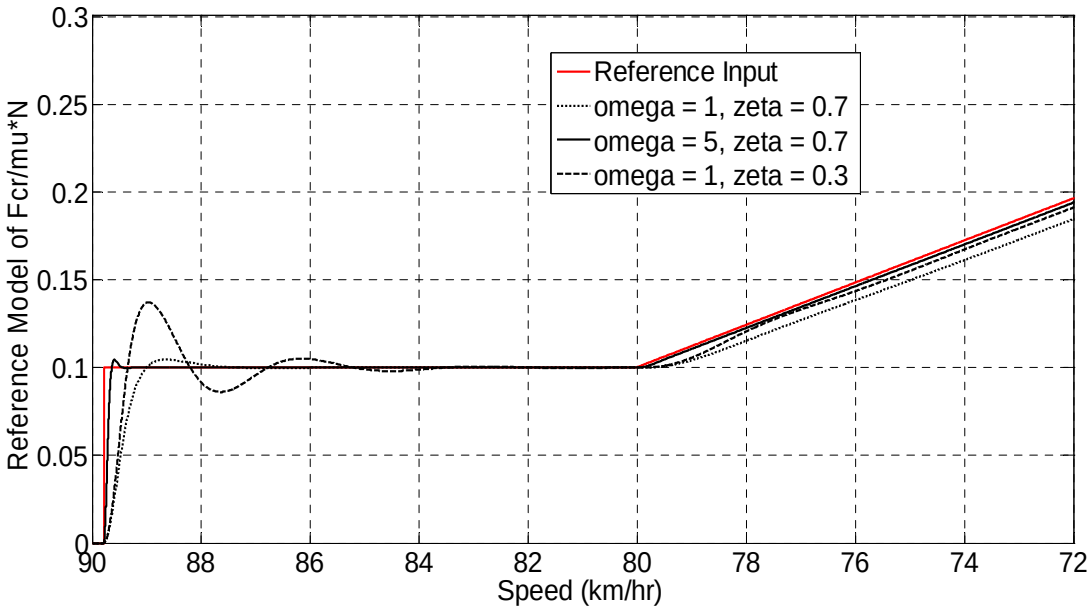

Figure 5.12 Reference model responses versus speeds using different design characteristics for high speeds.

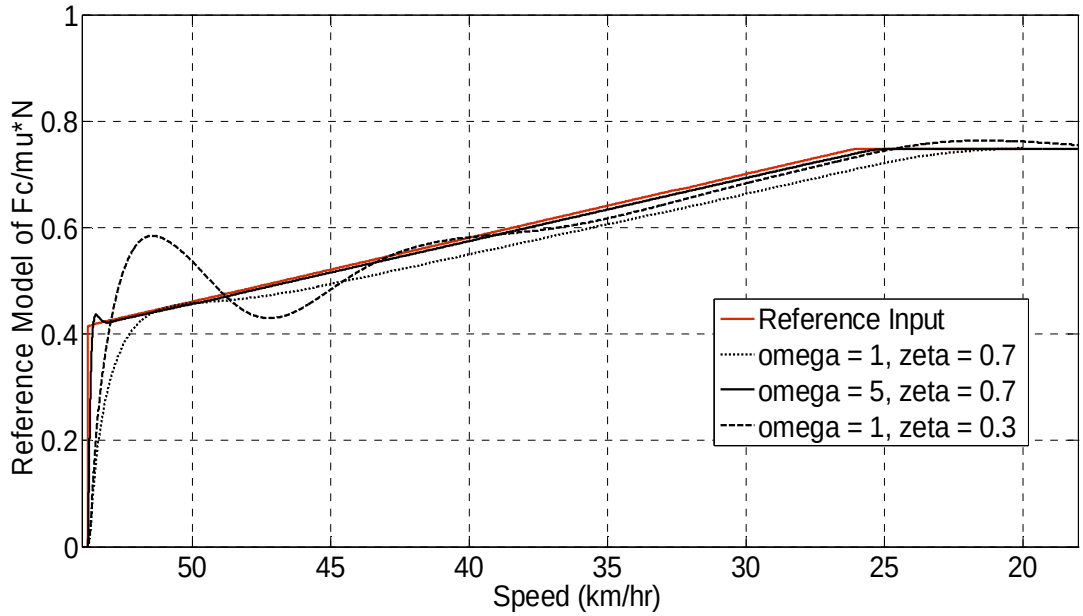

Figure 5.13 Reference model responses versus speeds using different design characteristics for moderate speeds.

As mentioned earlier in Section 2.4, increasing γ results in faster adaptation and consequently a quicker system response. Decreasing γ results in slower adaptation and consequently a longer response time. In this control model, γ is chosen as 500 for an acceptable system response. Because the system output closely follows the reference model output that is designed for safe braking, safe train braking will be achieved. The coupler forces will be plotted to make sure that they are within the acceptable limits. According to coupler design, the maximum allowable coupler force is set at 1,100 kN (24.7 kips) which is determined to be below the limit causing coupler damage or derailment [4, 21]. To reduce the computational time, one controller will be used for the first wheelseet and identical dynamic braking torque will be applied to all locomotive wheelsets.

5.4 Simulation and Results

For all simulation runs, the initial speed is fixed at 90 km/hr (approximately 60 mph), the locomotive mass is 190,500 kg (approximately 420,000 lb), and each freight car mass is 130,000 kg (approximately 286,000 lb). It is assumed that all locomotive wheelsets are motorized with DC or AC traction motors. Two cases are considered:

1) the wheel/rail adhesion coefficients are changed with time traveled in order to evaluate the MRAC performance under different wheel/rail conditions, and
2) the wheel/rail adhesion coefficients are changed randomly according to the distance traveled along the rail.

The simulation results will be presented for each case by showing the controlled motor current for DC motors, and the controlled voltage excitation frequency for AC traction motors.

5.4.1 Case 1: MRAC Performance

Figure 5.14 shows the assumed wheel/rail adhesion coefficient, μ, versus time. There are sudden changes in μ every seven seconds in order to simulate rail friction changes that are assumed to occur during braking. The results for each type of traction motor are discussed in the following sections.

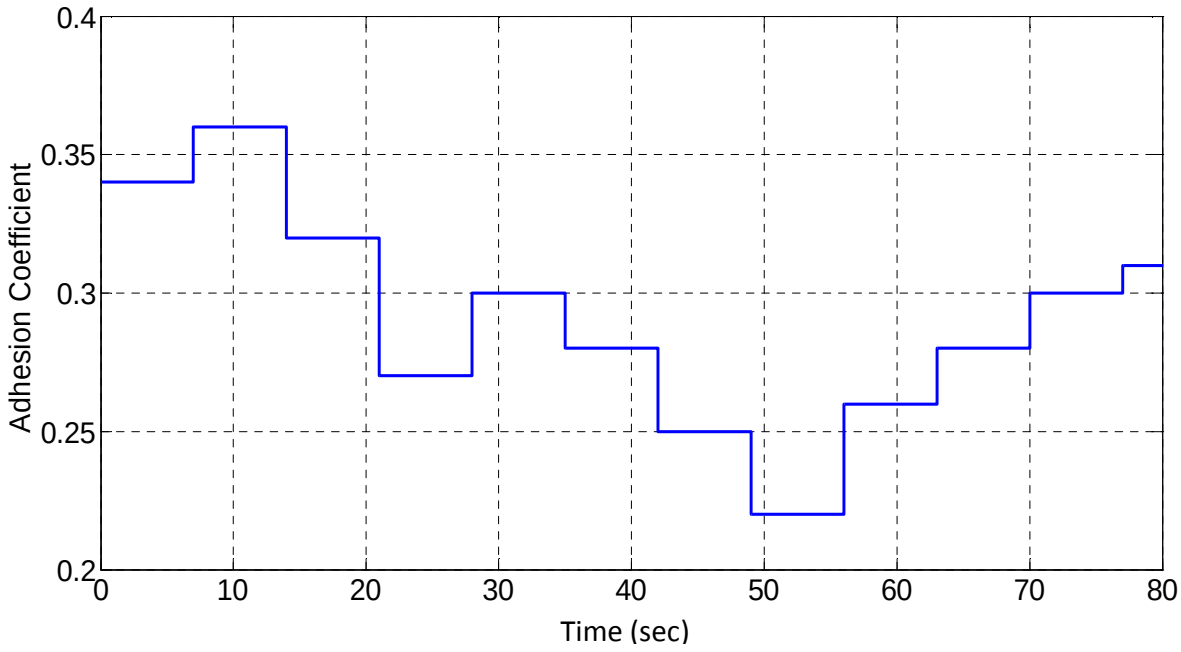

Figure 5.14 Adhesion coefficient versus time.

5.4.1.1 DC Motors

Figure 5.15 indicates that MRAC is able to adjust the motor current rapidly to accommodate the changes occurring at the rail. The dynamic braking torque, which is directly related to the motor current, is shown in Figure 5.16. The measurable system output, N/S_T, is plotted versus time in Figure 5.17. Using the relationship established in Figure 5.9, the normalized creep force is plotted and it is maintained closely as the designed reference model output, as shown in Figure 5.18. The coupler forces are shown in Figure 5.19, indicating that the 1st coupler has the highest force because of the buff loads due to the three railcars behind the locomotive. The 3rd coupler force is the lowest because it is subjected to the buff load of only one railcar. This means that couplers that are closer to the locomotive are subjected to higher forces than those farther away from the locomotive during braking. The highest coupler force of 240 *k*N is considerably smaller than the coupler design limit. Figure 5.20 and Figure 5.21 show the distance travelled by the train and train speed, respectively, versus time.

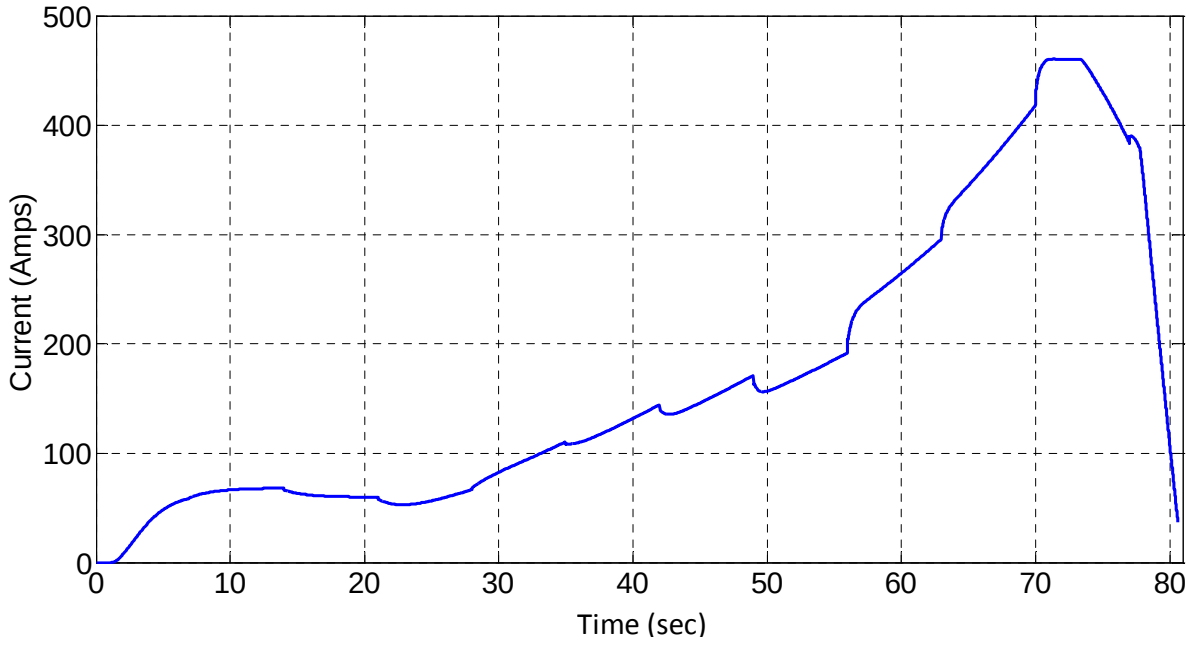

Figure 5.15 Controlled motor current versus time using DC motors.

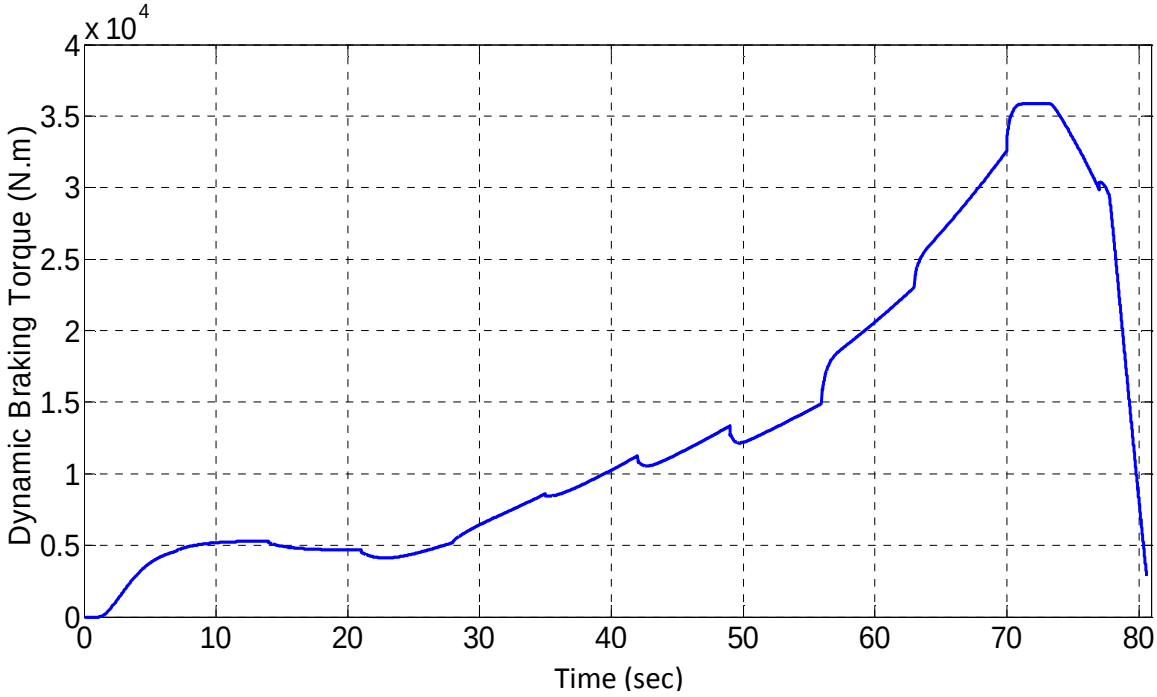

Figure 5.16 Controlled dynamic braking torque versus time using DC motors.

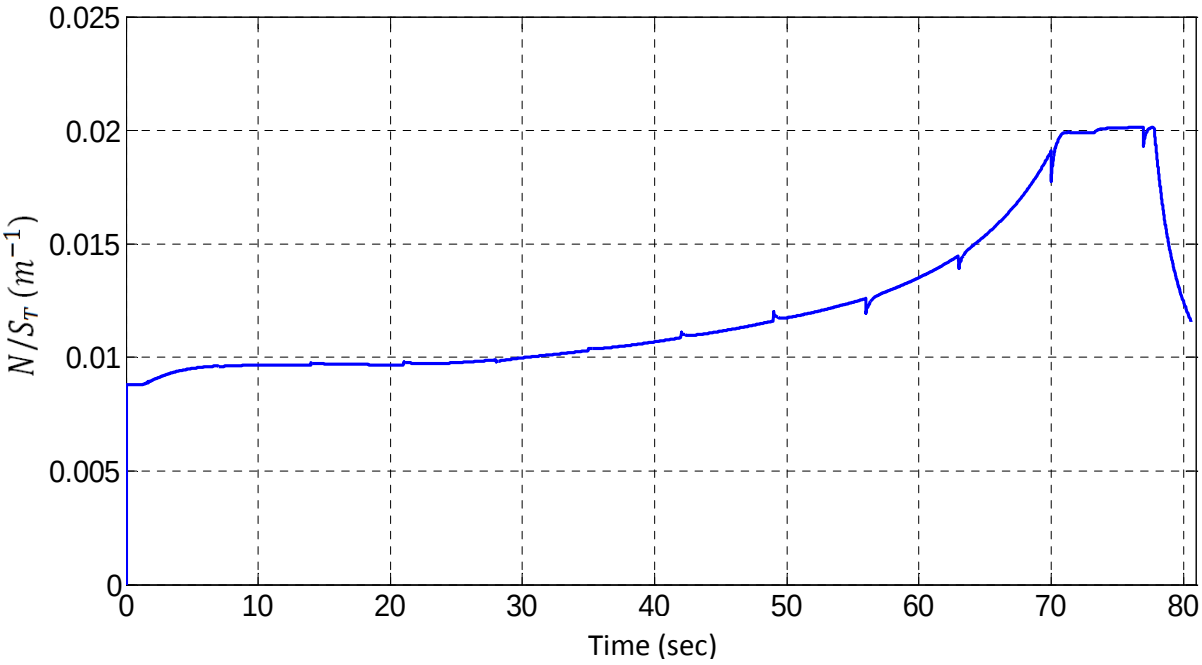

Figure 5.17 N/S_T versus time using DC motors.

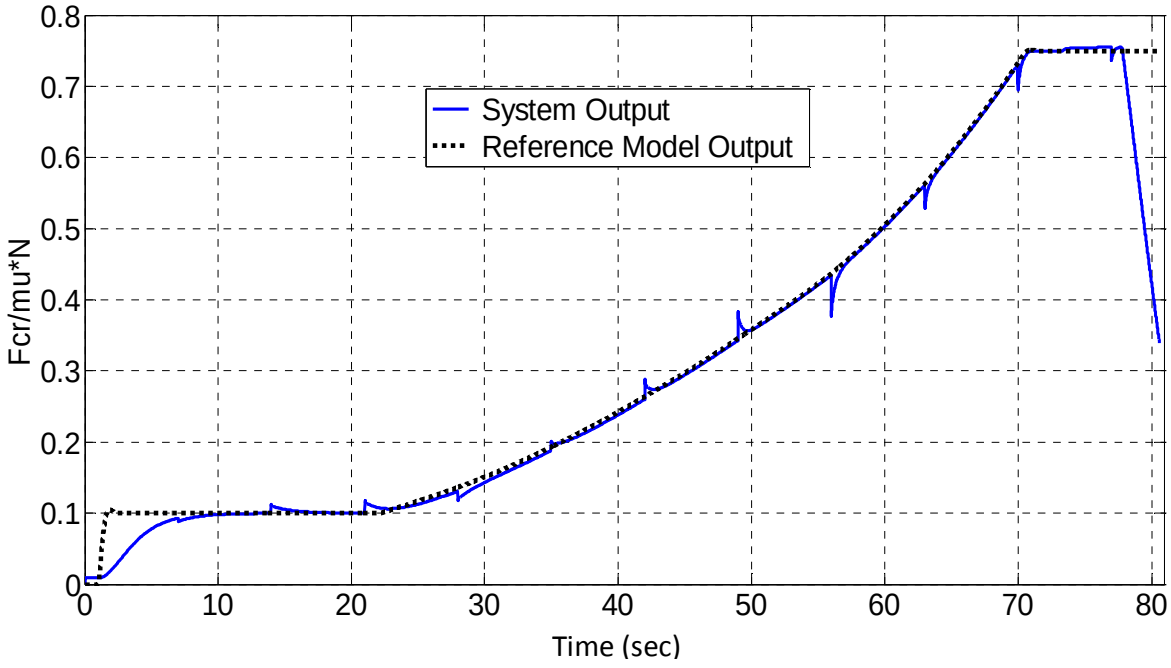

Figure 5.18 Normalized creep force and reference model output versus time using DC motors.

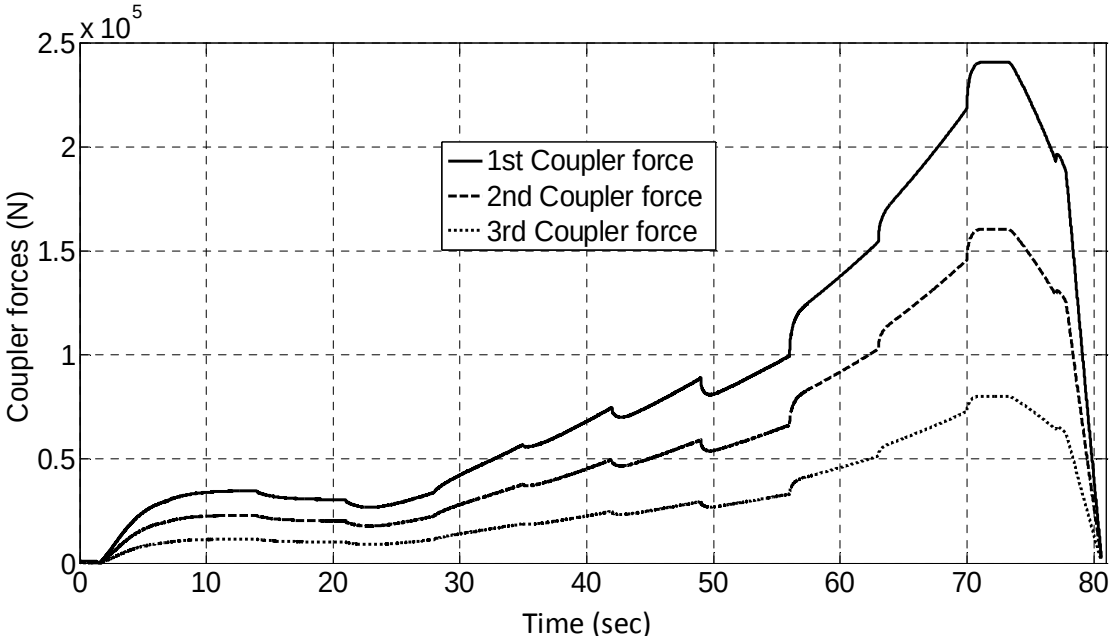

Figure 5.19 Coupler forces versus time using DC motors.

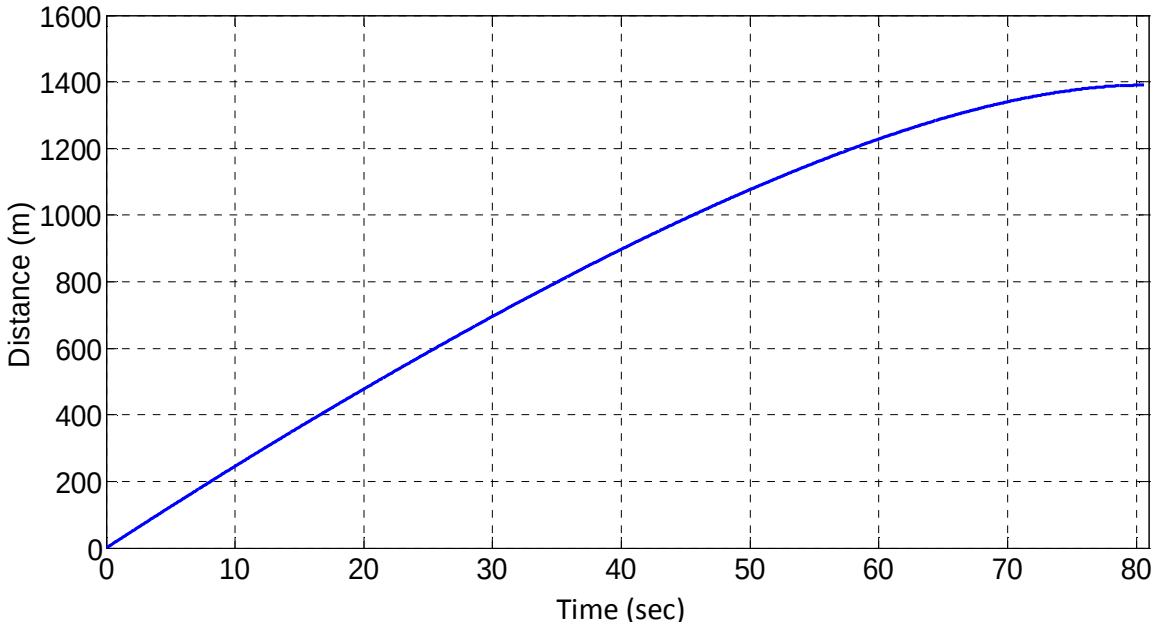

Figure 5.20 Train braking distance versus time using DC motors.

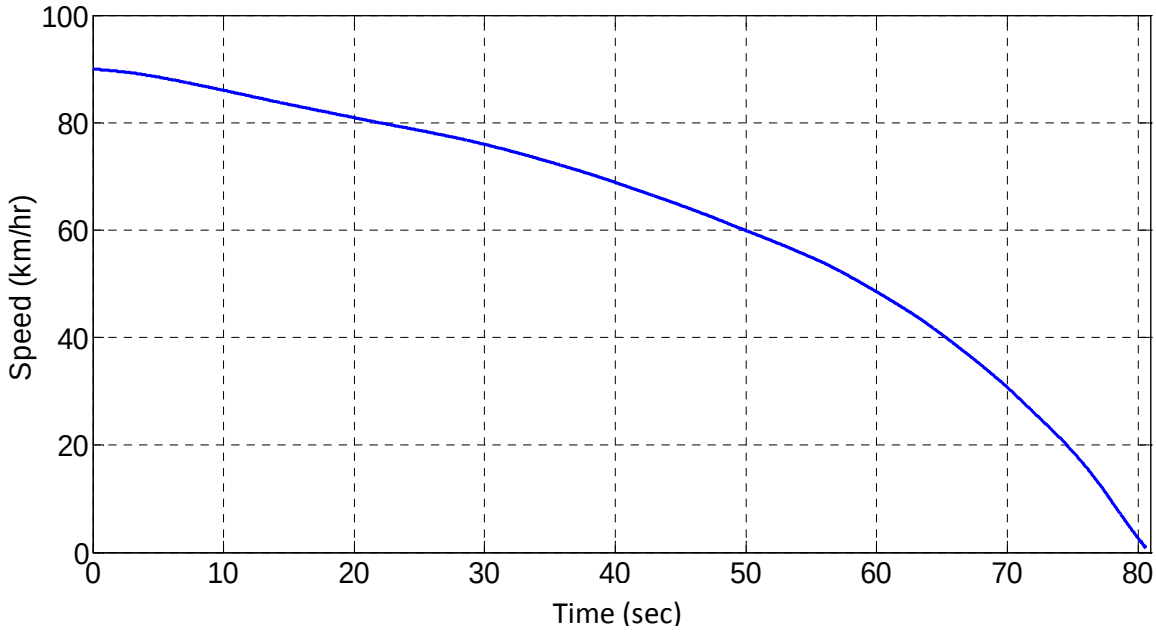

Figure 5.21 Train speed versus time using DC motors.

5.4.1.2 AC Motors

Figure 5.22 indicates that MRAC is able to adjust the dynamic braking torque rapidly to accommodate the changes occurring at the rail. The motor excitation frequency, which is based on the motor slip ratio, is shown in Figure 5.23. The excitation frequency is magnified at two selected times in Figure 5.24 to show the adjusted frequency when the motor torque needs adjustment in the control model. The measurable system output, N/S_T, is plotted versus time in Figure 5.25. Using the relationship established in Figure 5.9, the normalized creep force is plotted and is maintained close to the designed reference model output, as shown in Figure 5.26. The coupler forces are shown in Figure 5.27, which indicate that the highest coupler force of 250 *k*N is considerably smaller than the coupler design limit. Figures 5.28 and 5.29 show the train braking distance and train operating speed, respectively, versus time.

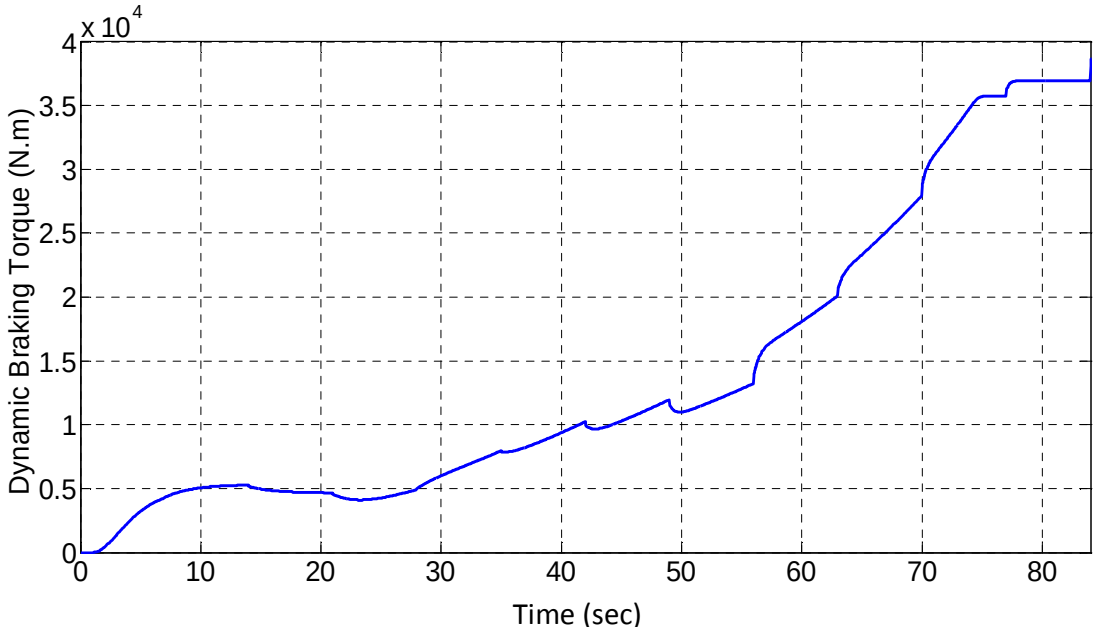

Figure 5.22 Controlled dynamic braking torque versus time using AC motors.

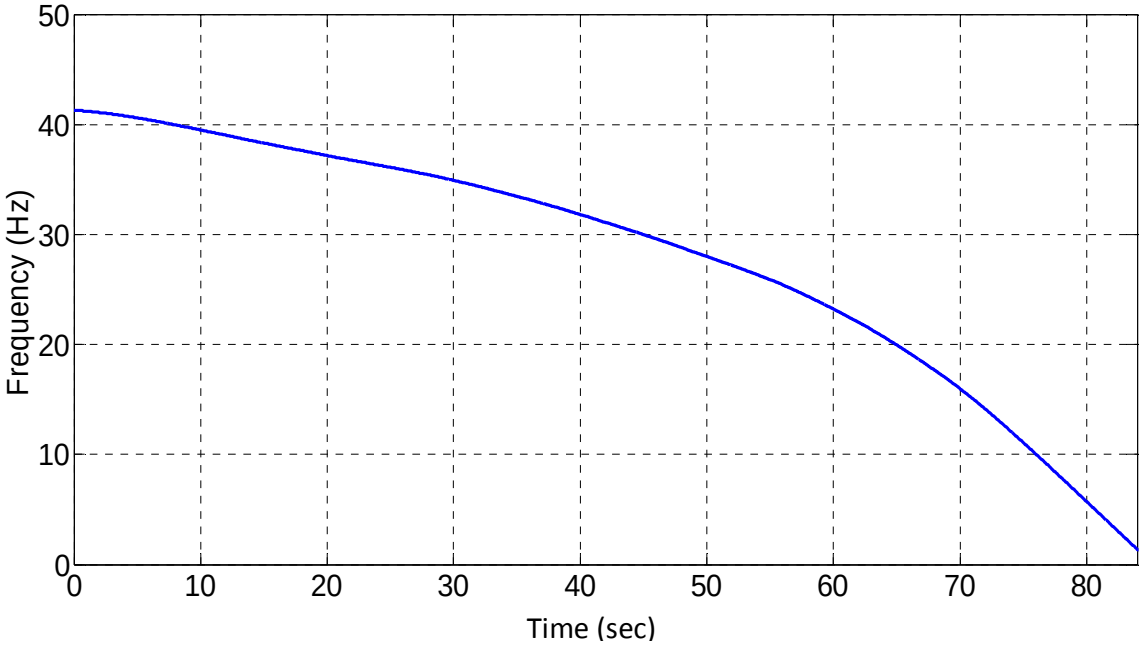

Figure 5.23 Controlled motor excitation frequency versus time using AC motors.

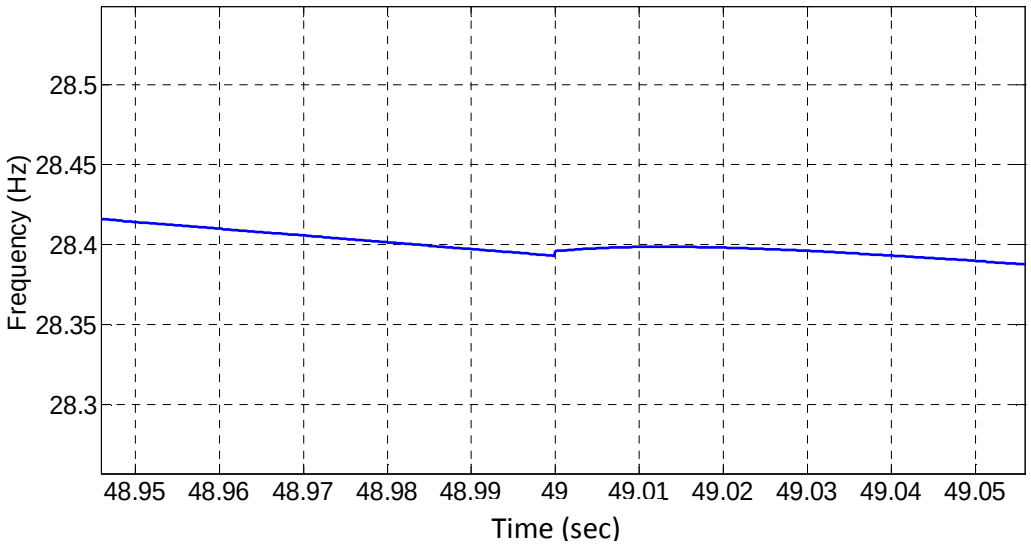

(a)

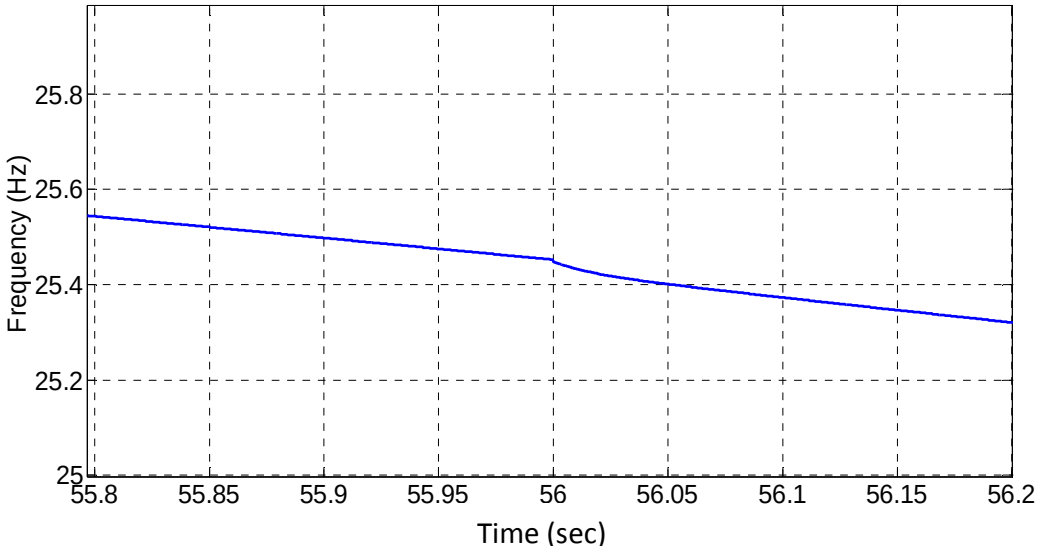

(b)

Figure 5.24 Controlled motor excitation frequency versus times at (a) 49 sec. and (b) 56 sec.

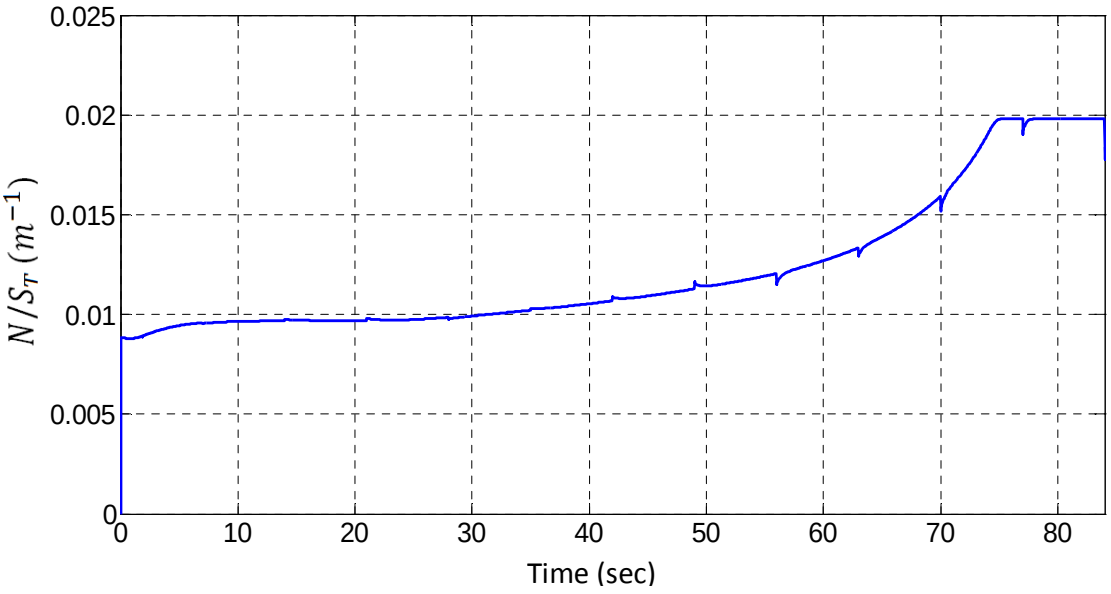

Figure 5.25 N/S_T versus time using AC motors.

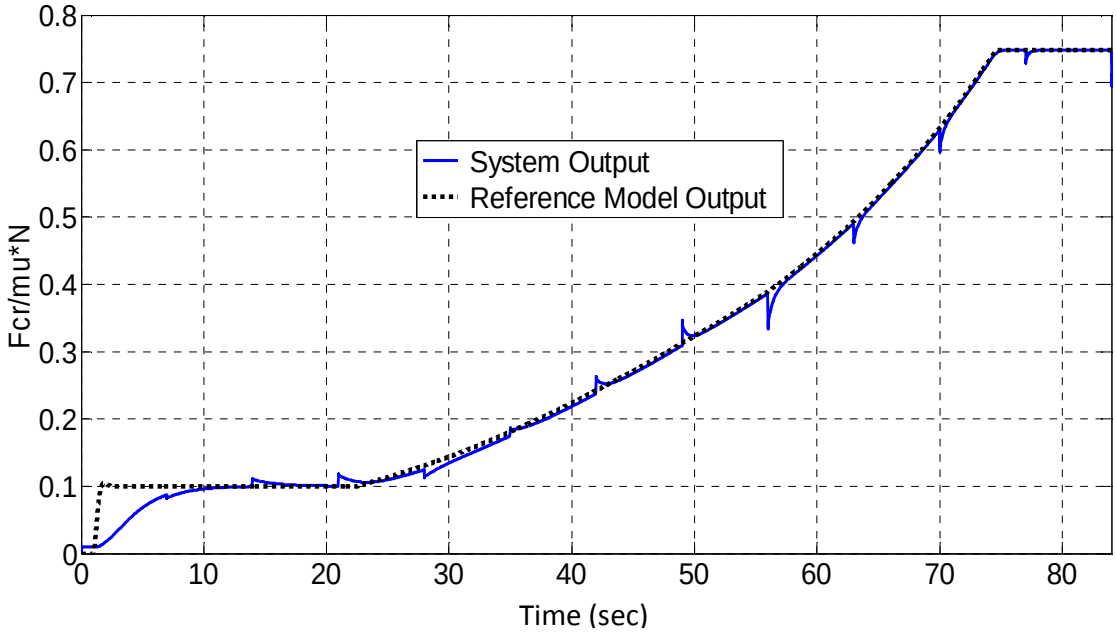

Figure 5.26 Normalized creep force and reference model output versus time using AC motors.

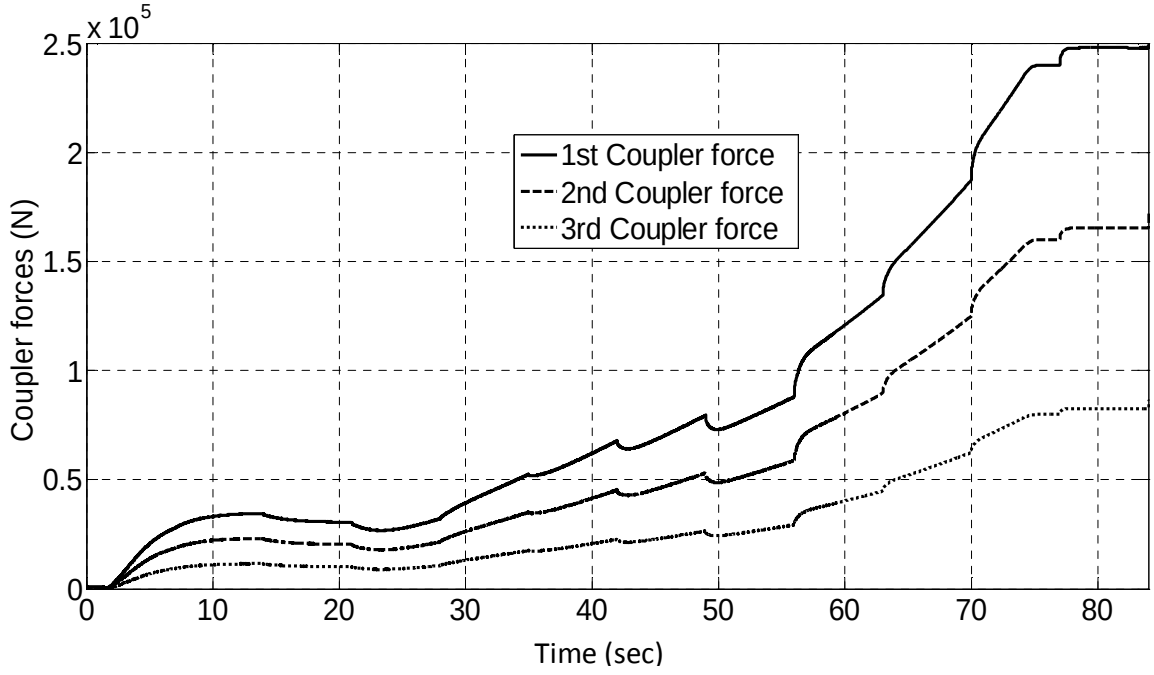

Figure 5.27 Coupler forces versus time using AC motors.

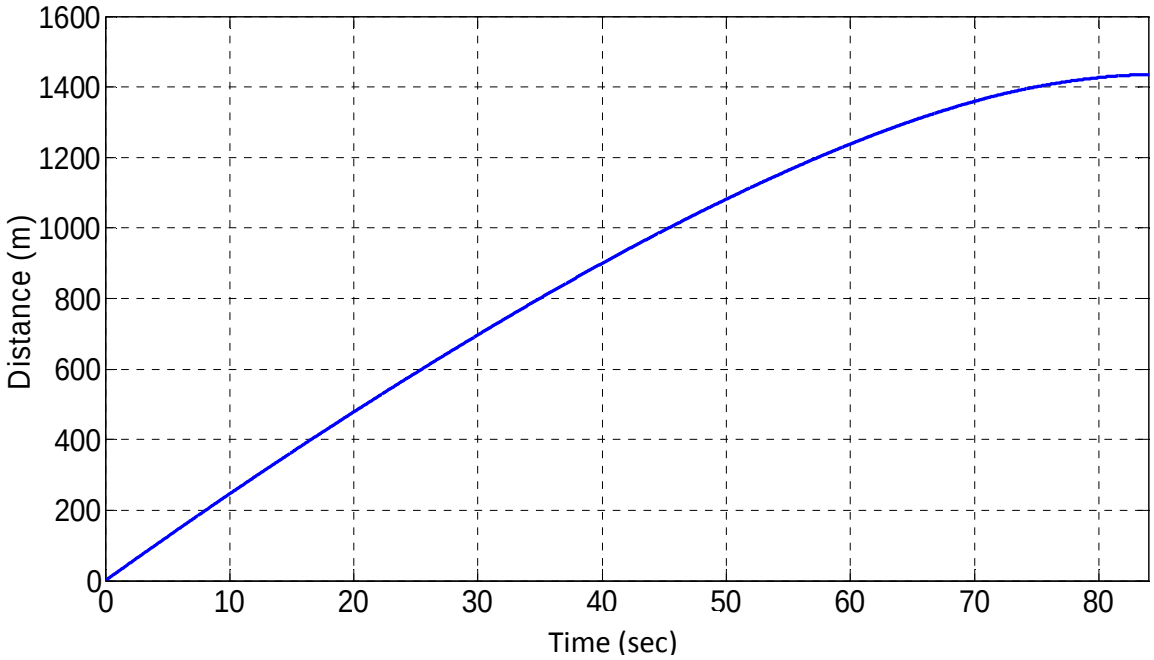

Figure 5.28 Train braking distance versus time using AC motors.

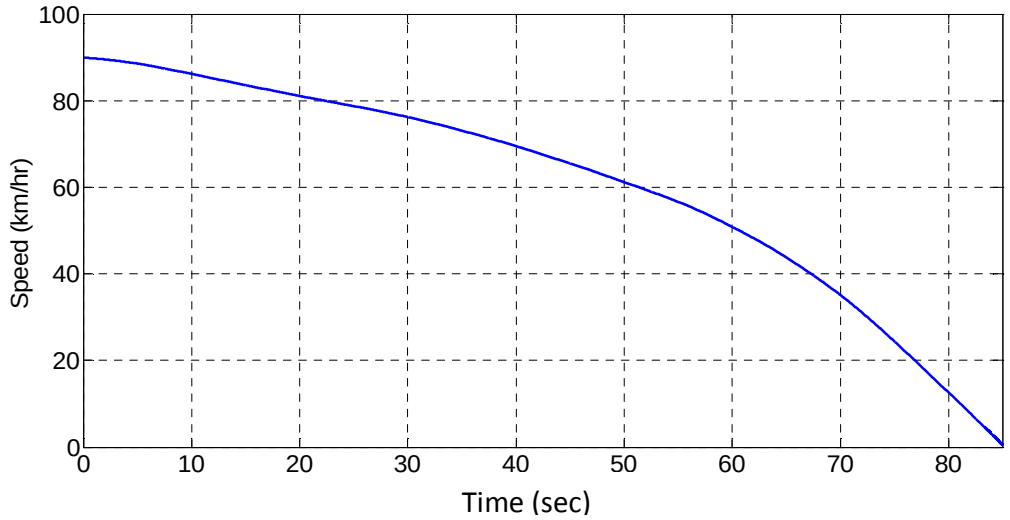

Figure 5.29 Train speed versus time using AC motors.

The difference in the train braking distance for DC and AC traction motors cannot be compared since the available braking effort at low speeds for both motor types is different. Additionally, pneumatic brakes are applied at low speeds in the simulations when using DC motors.

5.4.2 Case 2: Wheel/Rail Adhesion Coefficient Change with Distance

Figure 5.30 shows assumed wheel/rail adhesion coefficient, μ, versus distance on the track. The adhesion coefficient changes randomly between high and low values along the track. Next, the results will be shown for each type of traction motor.

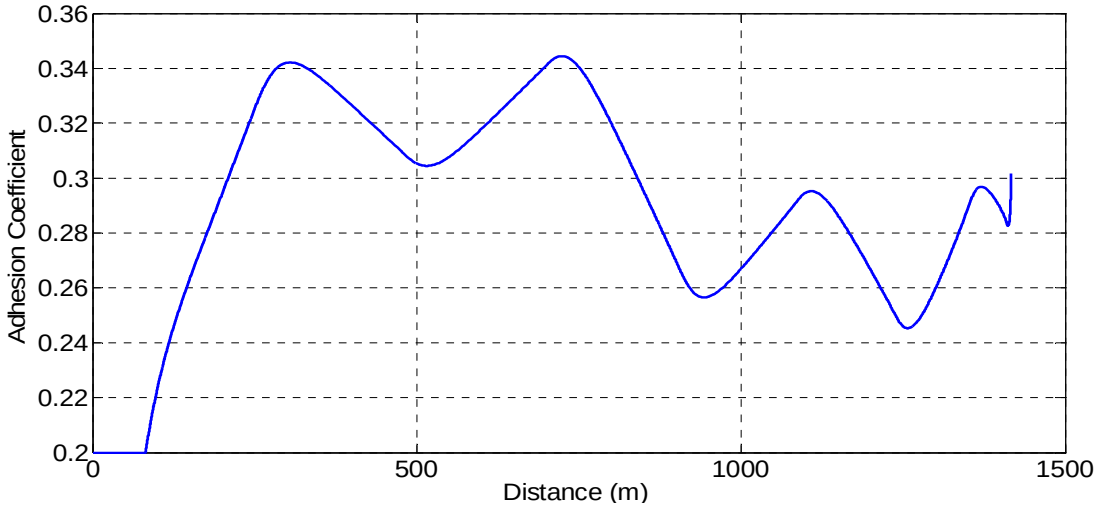

Figure 5.30 Adhesion coefficient versus distance on the track.

5.4.2.1 DC Motors

MRAC is able to keep the normalized creep force very close to the reference model output as shown in Figure 5.31. At low speeds, the normalized creep force decreases since the available braking torque decreases. The simulations are stopped at 0.7 km/hr since the computational time is very long to decrease the train speed to a complete stop. The measurable system output, N/S_T, is plotted versus time in Figure 5.32. MRAC is able to adjust the motor current to accommodate the changes occurring at the rail as shown in Figure 5.33. The dynamic braking torque, which is directly related to the motor current, is shown in Figure 5.34. In Figure 5.35, the coupler forces are plotted versus distance, where the first coupler has a maximum of 240 *k*N force. The distance travelled by the train is approximately 1371 m (1500 yards) as seen in Figure 5.36. The train speed versus time is also plotted in Figure 5.36.

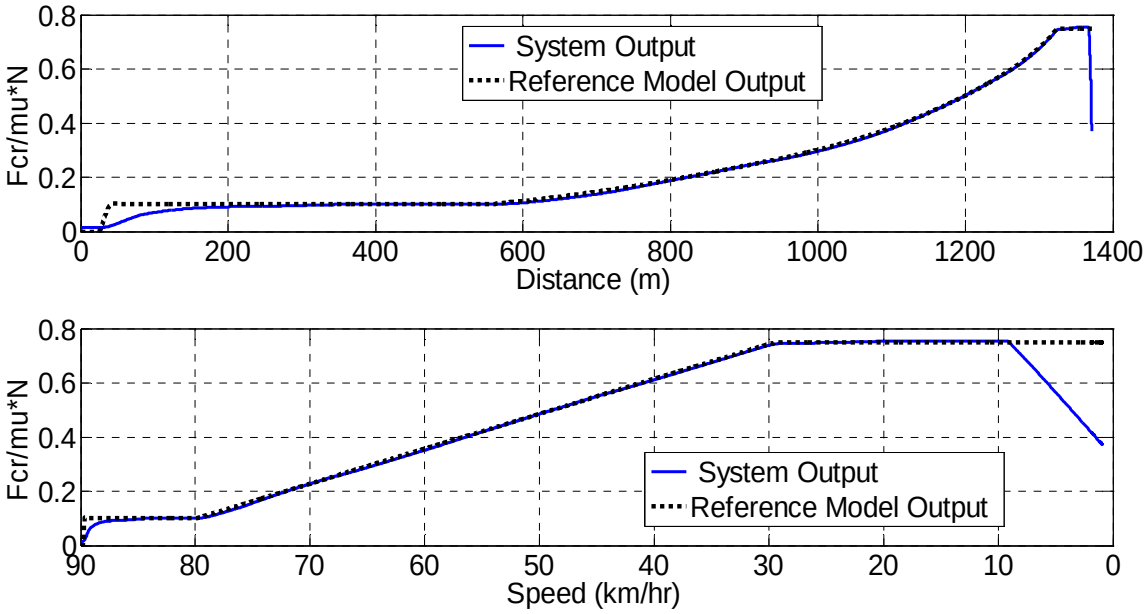

Figure 5.31 Normalized creep force and reference model output using DC motors.

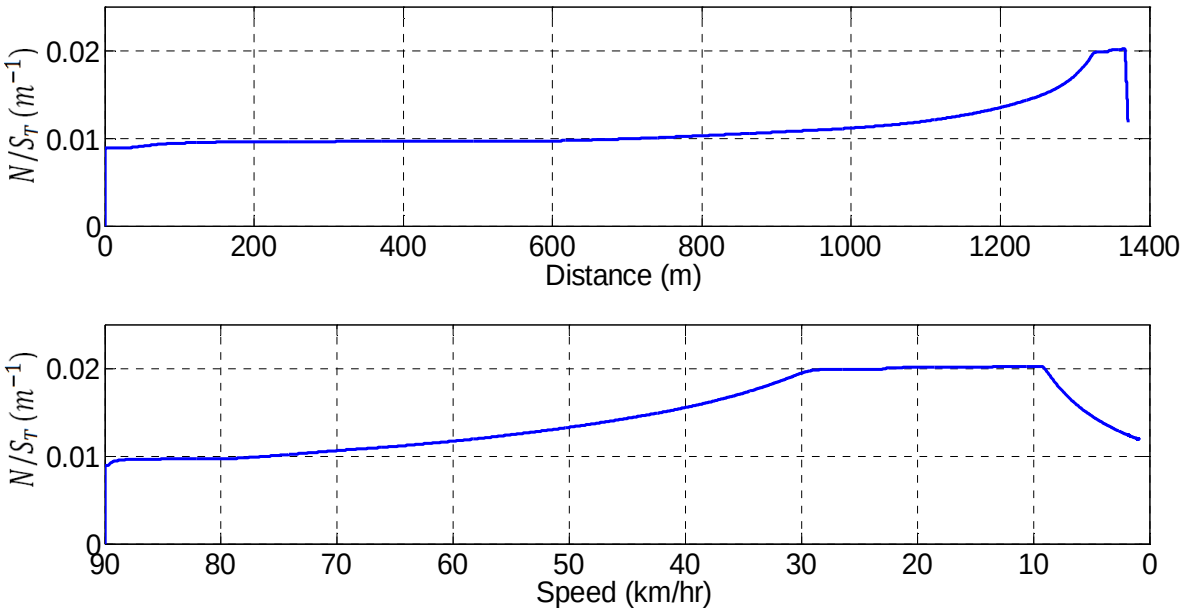

Figure 5.32 N/S_T versus distance and speed using DC motors.

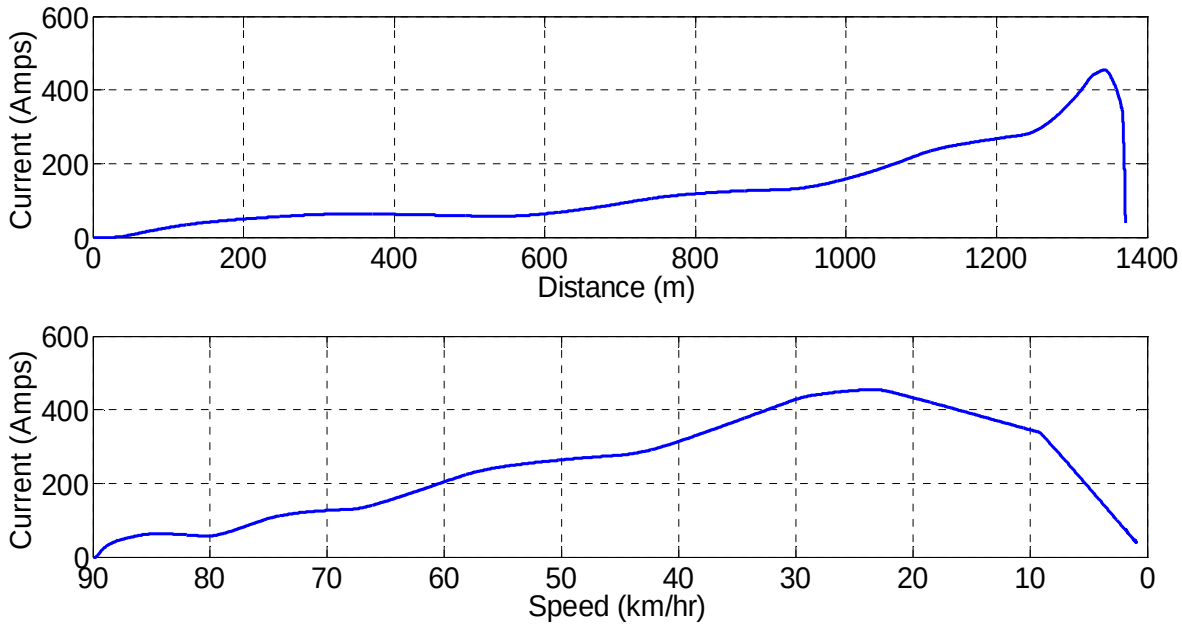

Figure 5.33 Controlled motor current versus distance and speed using DC motors.

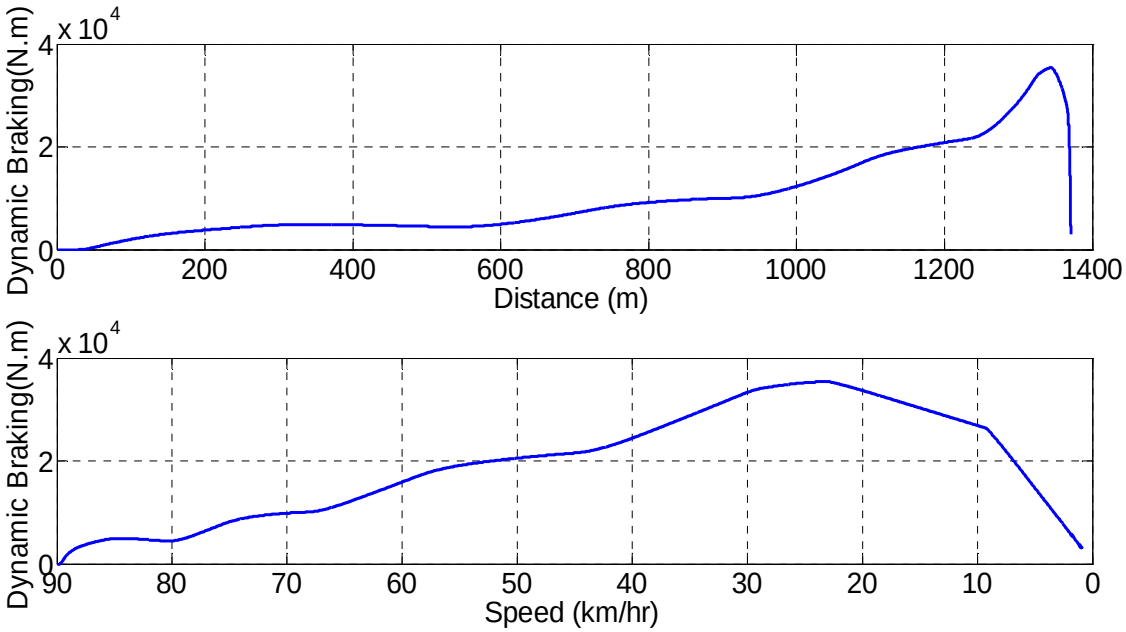

Figure 5.34 Controlled dynamic braking torque versus distance and speed.

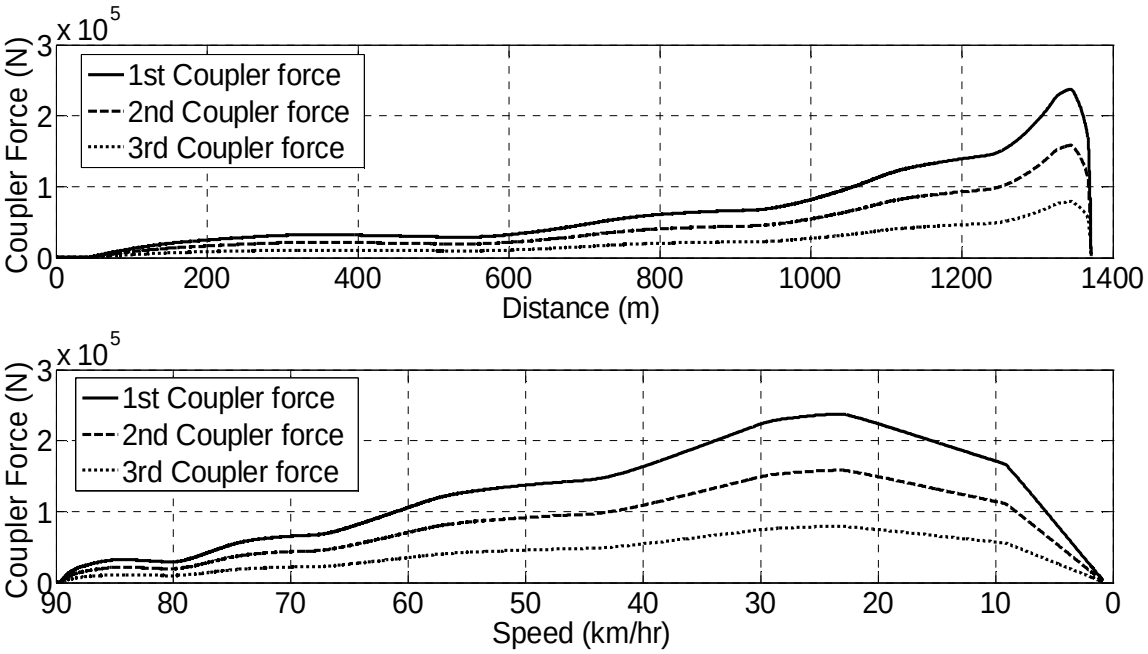

Figure 5.35 Coupler forces versus distance and speed using DC motors.

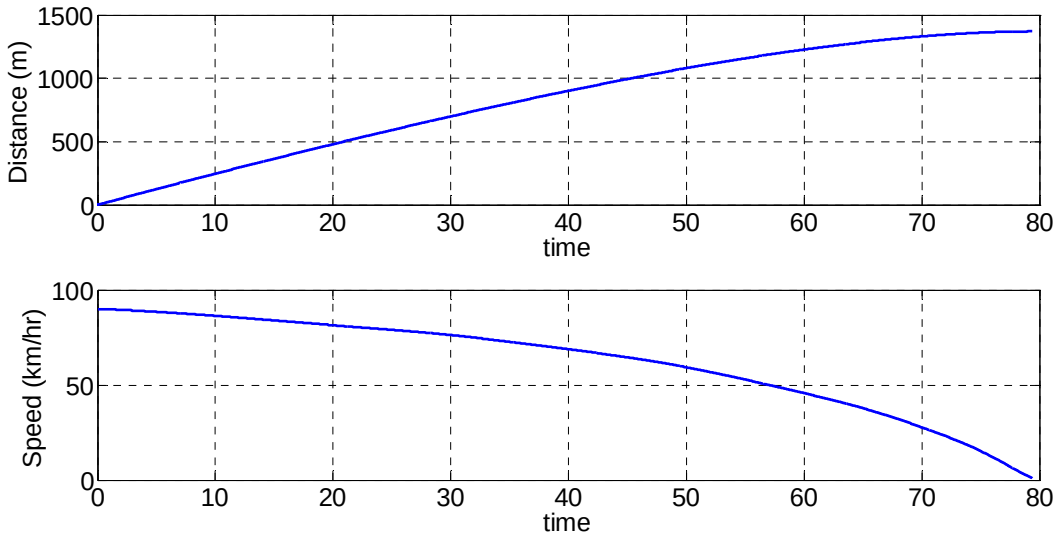

Figure 5.36 Distance travelled by the train and train speed versus time using DC motors.

5.4.2.2 AC Motors

Figure 5.37 indicates that MRAC is able to keep the normalized creep force very close to the reference model output. The measurable system output, N/S_T, is plotted in Figure 5.38. MRAC is able to adjust the dynamic braking torque rapidly to accommodate the changes occurring at the rail, as shown in Figure 5.39. The motor excitation frequency, which is based on the motor slip ratios, is shown in Figure 5.40. The coupler forces, shown in Figure 5.41, indicate that the maximum coupler force of 240 *k*N is much smaller than the coupler design limit. Train braking distance and train speed versus time are shown in Figure 5.42. The stopping distance is approximately 1415 m in this case.

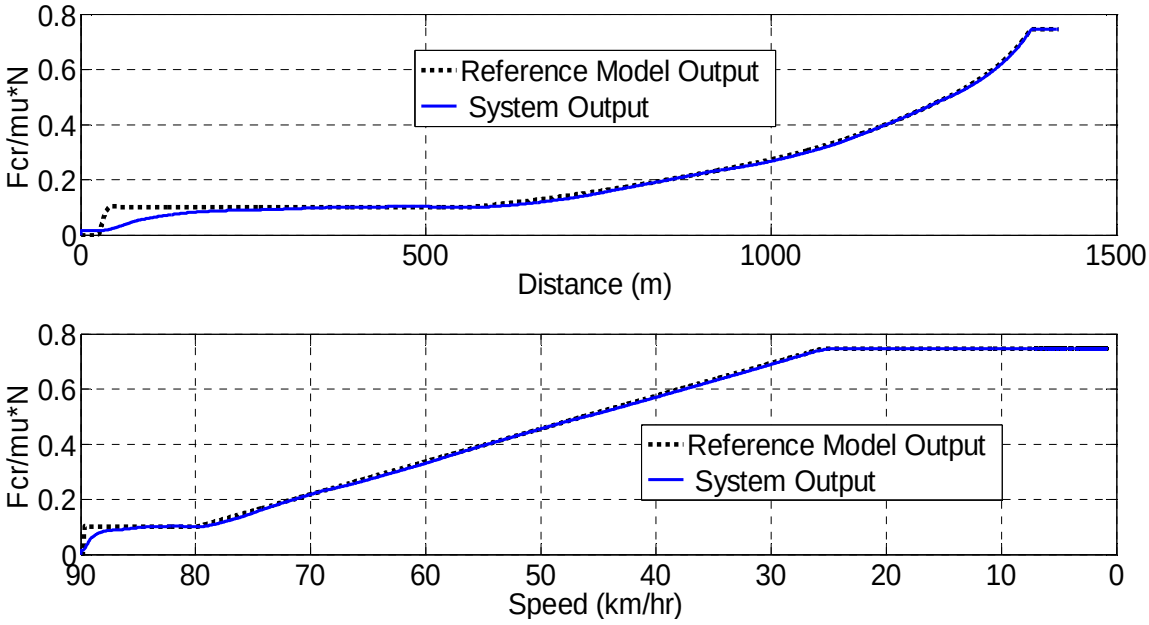

Figure 5.37 Normalized creep force and reference model output using AC motors.

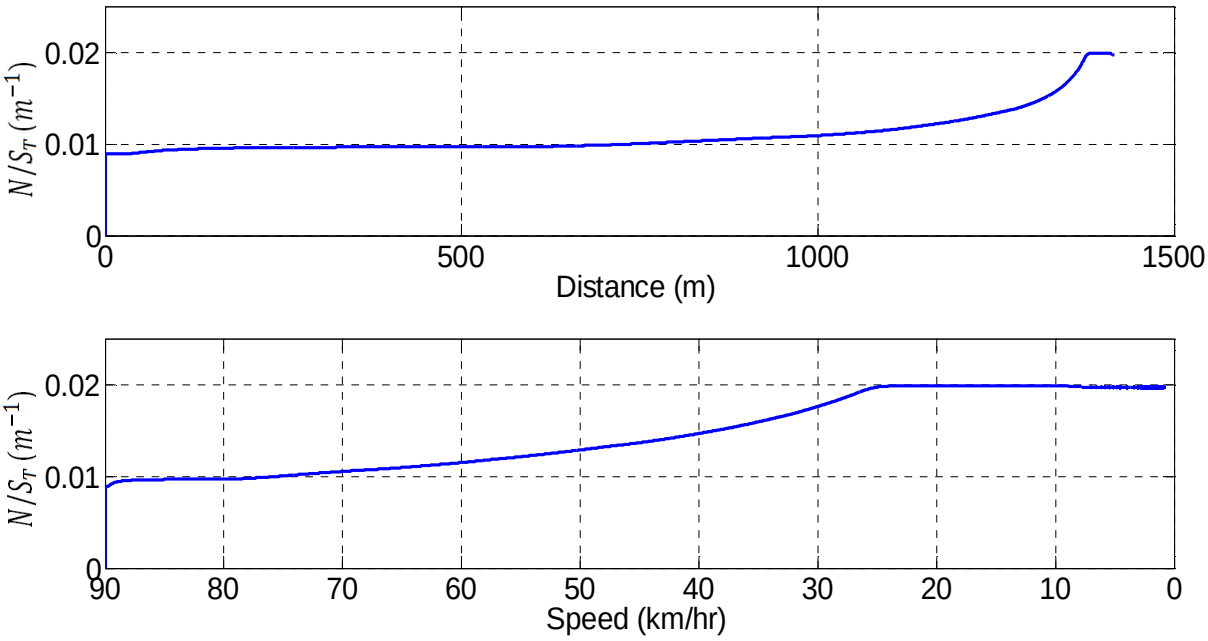

Figure 5.38 N/S_T versus distance and speed using AC motors.

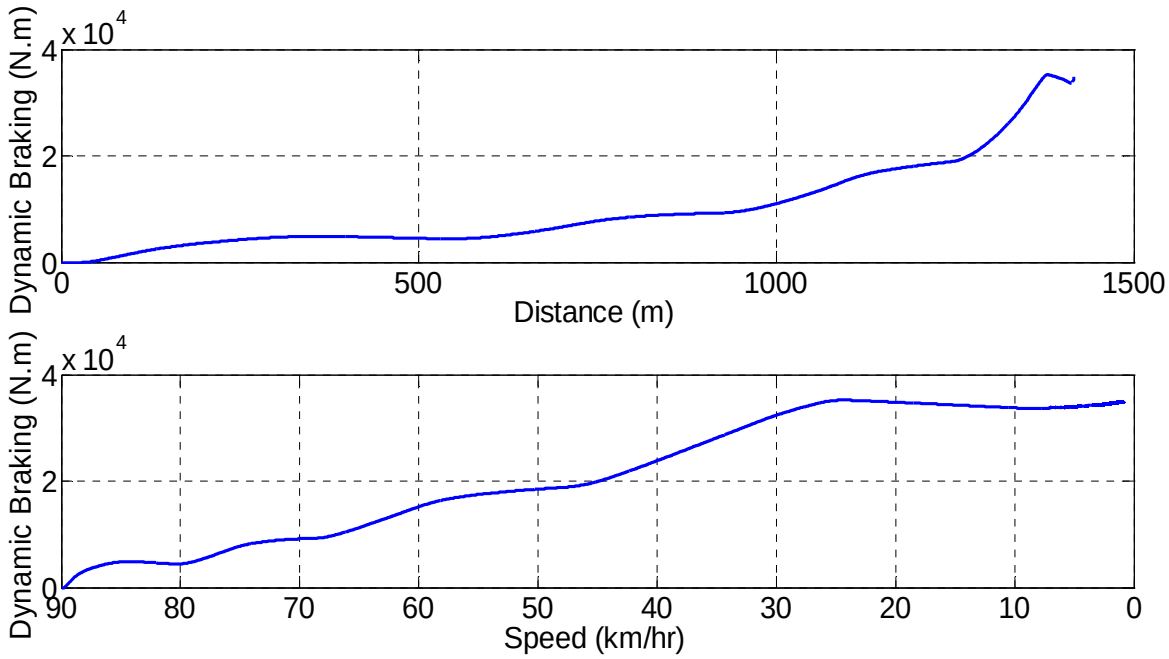

Figure 5.39 Controlled dynamic braking torque versus distance and speed.

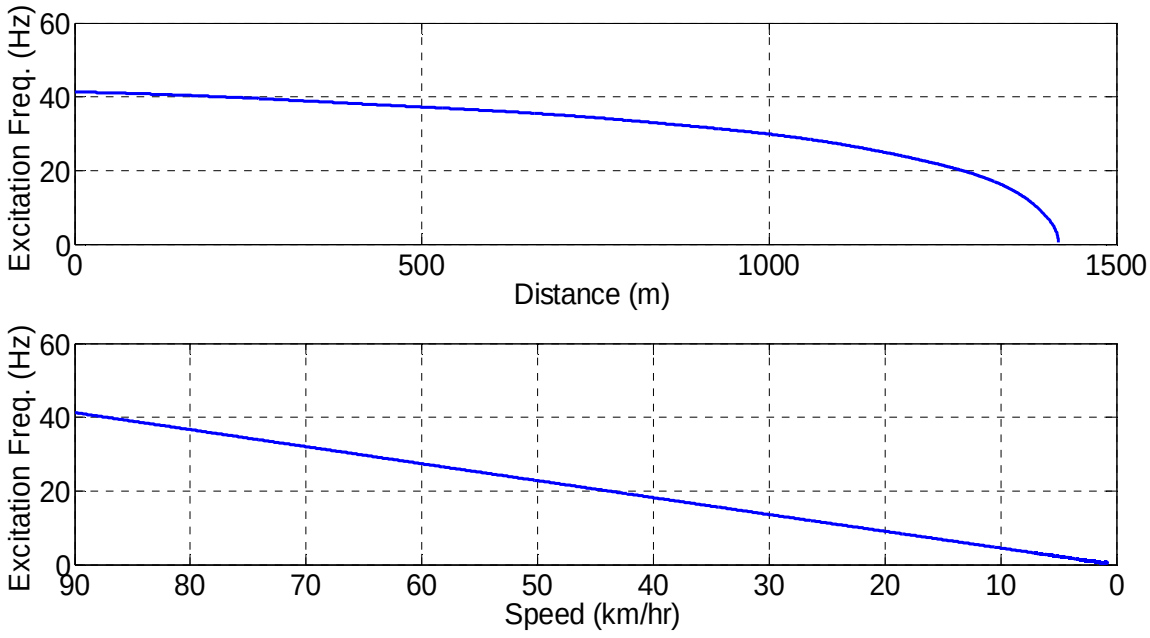

Figure 5.40 Controlled motor excitation frequency versus distance and speed using AC motors.

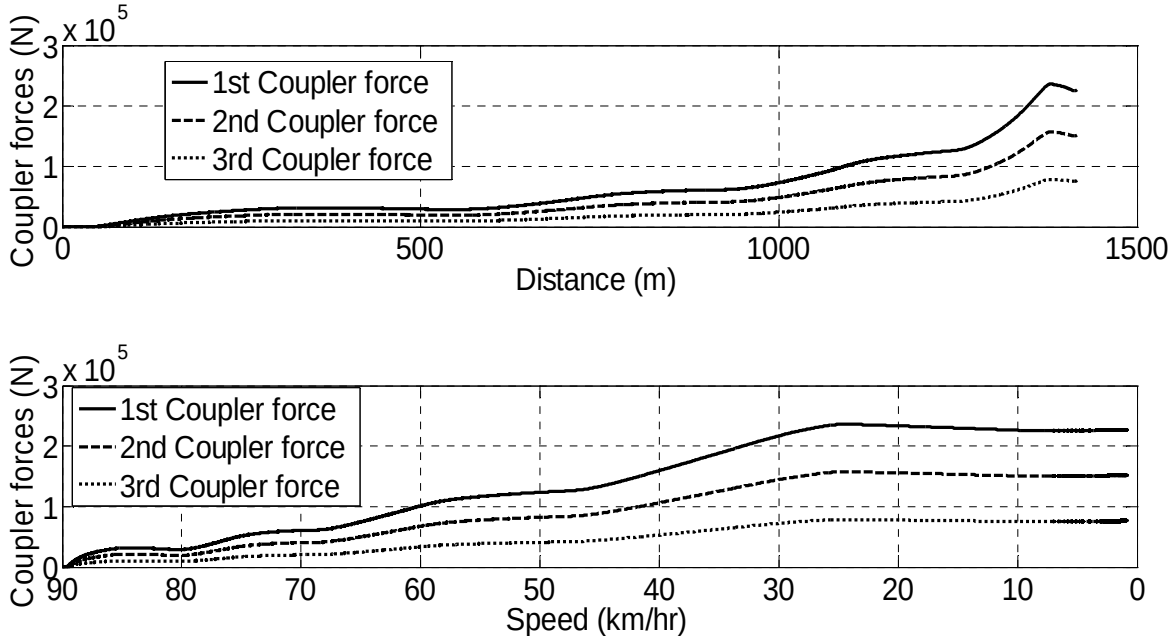

Figure 5.41 Coupler forces versus distance and speed using AC motors.

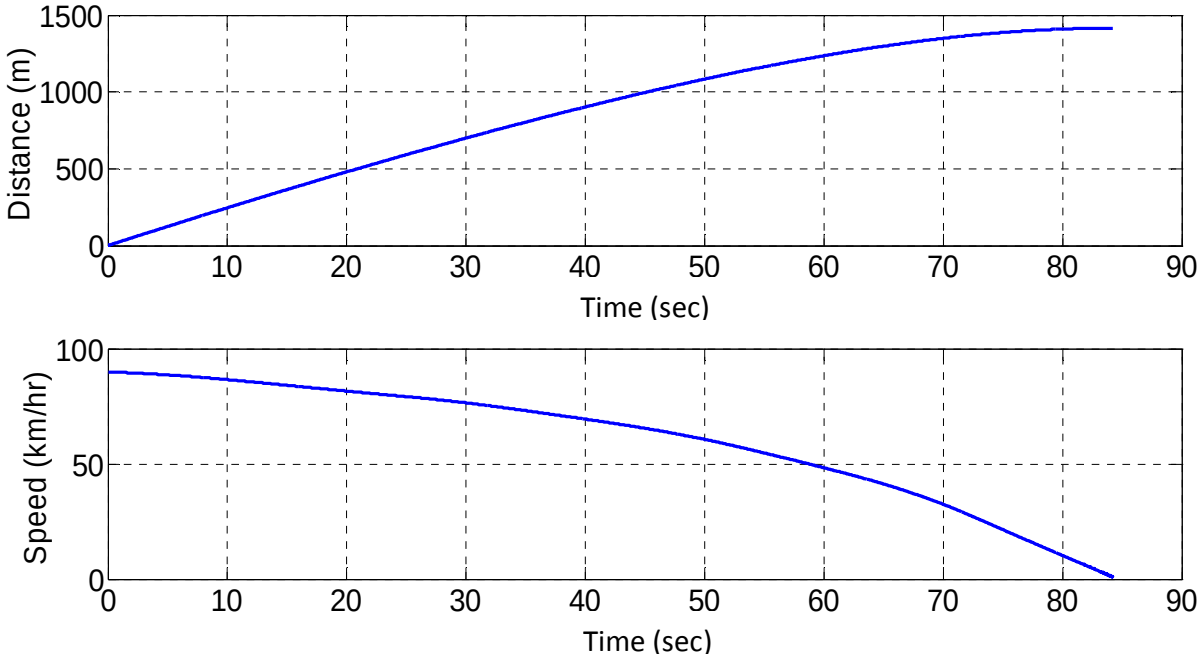

Figure 5.42 Distance travelled by the train and train speed versus time using AC motors.

Chapter 6

Robustness of the MRAC system

6.1 Introduction

In this chapter, the MRAC system robustness will be studied. In order to do this, the solution to control system problems such as input and output disturbances using MRAC will be investigated. Train system parameters will be changed rapidly to investigate the MRAC system's ability to resist these changes and adapt control parameters without changing the initial conditions of the train operation. System parameters that will be varied include coupler forces, primary suspension forces, longitudinal creepage, normal load, and braking torque. Only the AC traction motor will be considered in this chapter. Figure 6.1 illustrate the input and output of the train system. The input starts with the motor excitation frequency, f_e, which determines the braking torque. The output of the train model is N/S_T, which is used to determine the normalized creep force, $F_{cr}/\mu N$. In the results, the inputs and outputs of the system will be plotted and discussed.

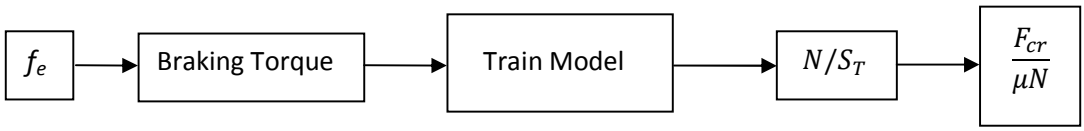

Figure 6.1 Block diagram of the train system inputs and outputs.

6.2 Simulations and Results

Random wheel/rail adhesion conditions are used. Adhesion conditions, shown previously in Figure 5.30, will be considered in the robustness study. The initial speed is 90 km/hr and the weight of the locomotive is 190,500 kg. In the MRAC system, the same reference model input is used as previously shown in Figure 5.11.

6.2.1 Coupler Stiffness and Damping

The coupler stiffness and damping are suddenly reduced and increased by 25%, as illustrated in Figure 6.2. These changes in the coupler forces are assumed to study the robustness of the

controller with respect to in-train forces. Figure 6.3 shows that the motor frequency and braking torque are not affected by the sudden changes in the coupler stiffness and damping. Figure 6.4 shows that, similarly, the output of the system is not affected by sudden changes in coupler stiffness and damping, and normalized creep forces, $F_{cr}/\mu N$, closely follow the reference model output response.

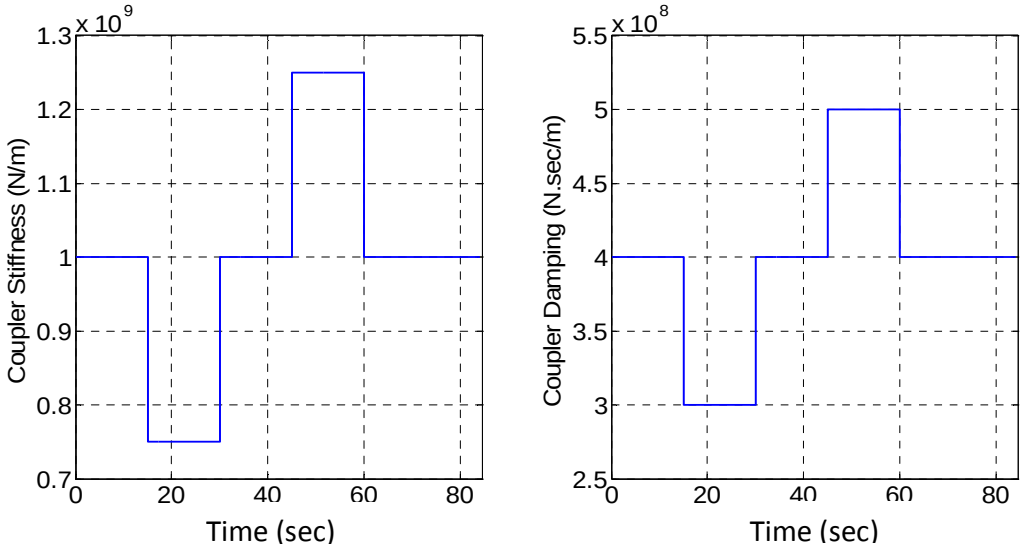

Figure 6.2 Sudden changes in the coupler stiffness and damping.

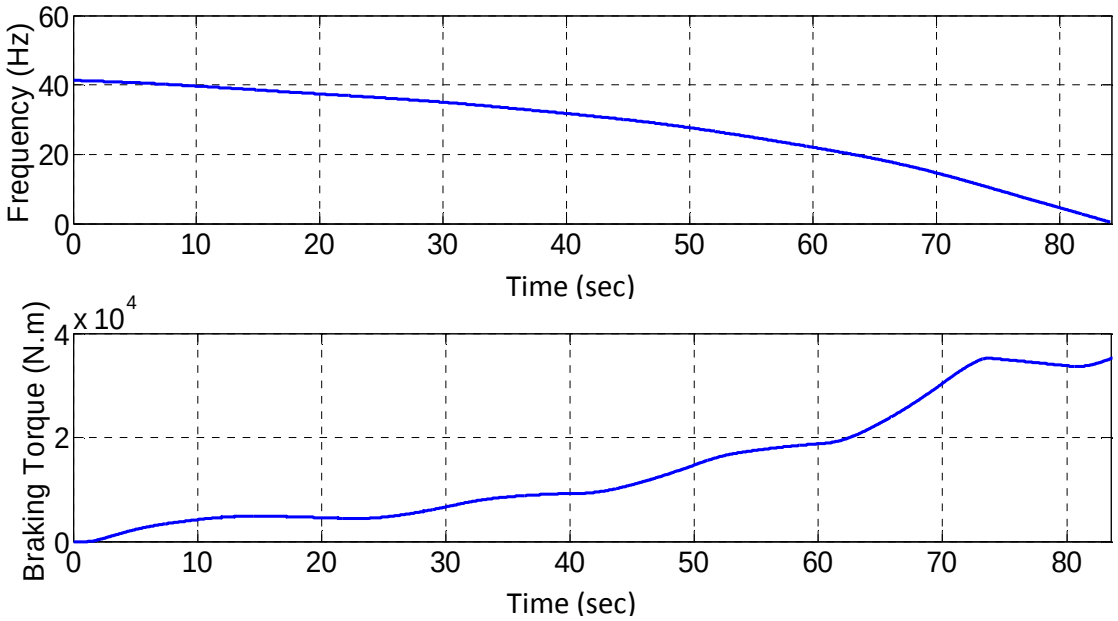

Figure 6.3 Motor excitation frequency and braking torque.

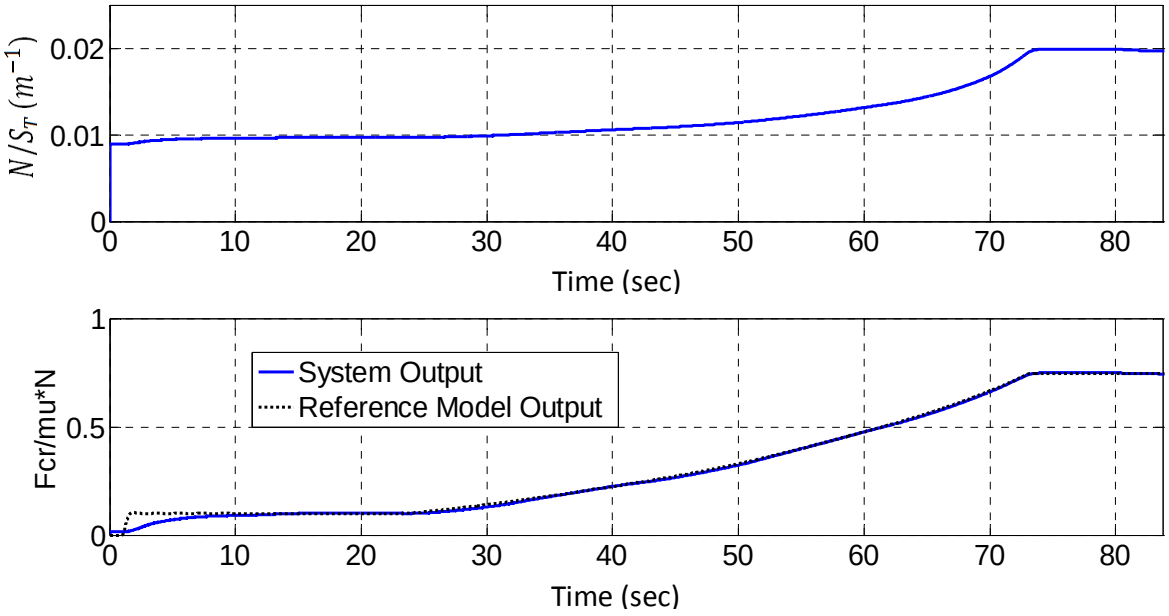

Figure 6.4 Train model outputs.

6.2.2 Primary Suspension Stiffness and Damping

Primary suspension stiffness and damping are reduced and increased by 25% in a square-wave function, as illustrated in Figure 6.5. The changes are not meant to suggest that such rapid changes in suspension stiffness and damping can happen in practice; they are merely intended to illustrate the system response robustness in the presence of $\pm 25\%$ error in the suspension model. Figure 6.6 shows that the motor frequency and braking torque are slightly affected by the sudden changes in the primary suspension stiffness and damping. The MRAC is able to accommodate these changes in less than 4 milliseconds, as shown in Figure 6.7, where the motor frequency plot is magnified at two time positions when the sudden changes occur. The outputs of the system are slightly affected by the sudden changes, as shown in Figure 6.8, and $F_{cr}/\mu N$ response closely follows the reference model output response.

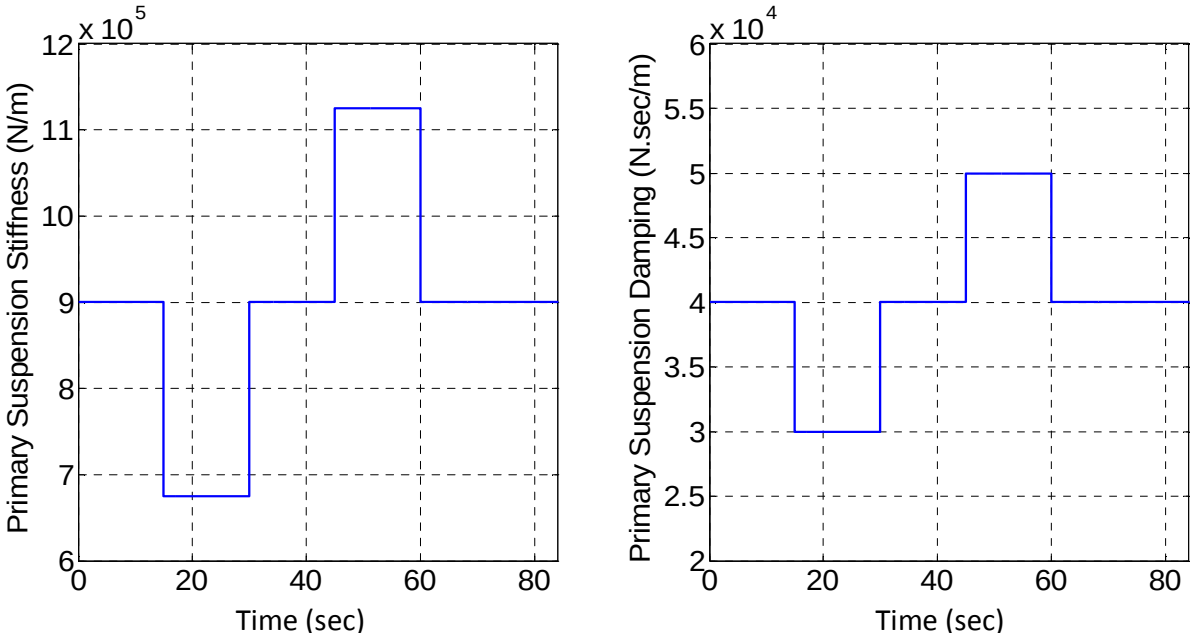

Figure 6.5 Sudden changes in the primary suspension stiffness and damping.

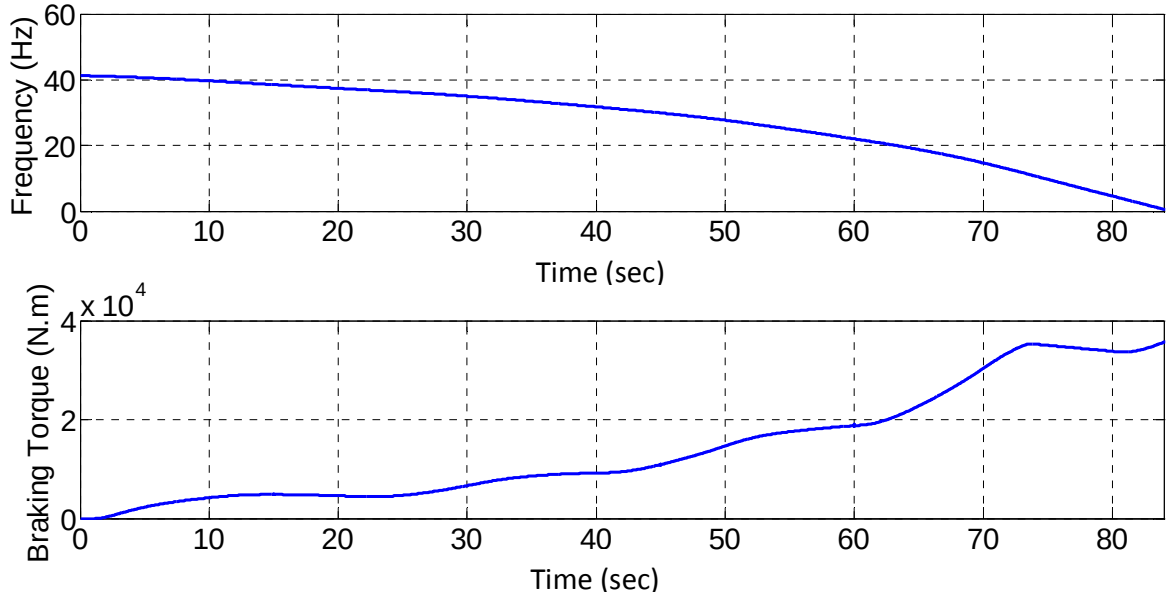

Figure 6.6 Motor excitation frequency and braking torque.

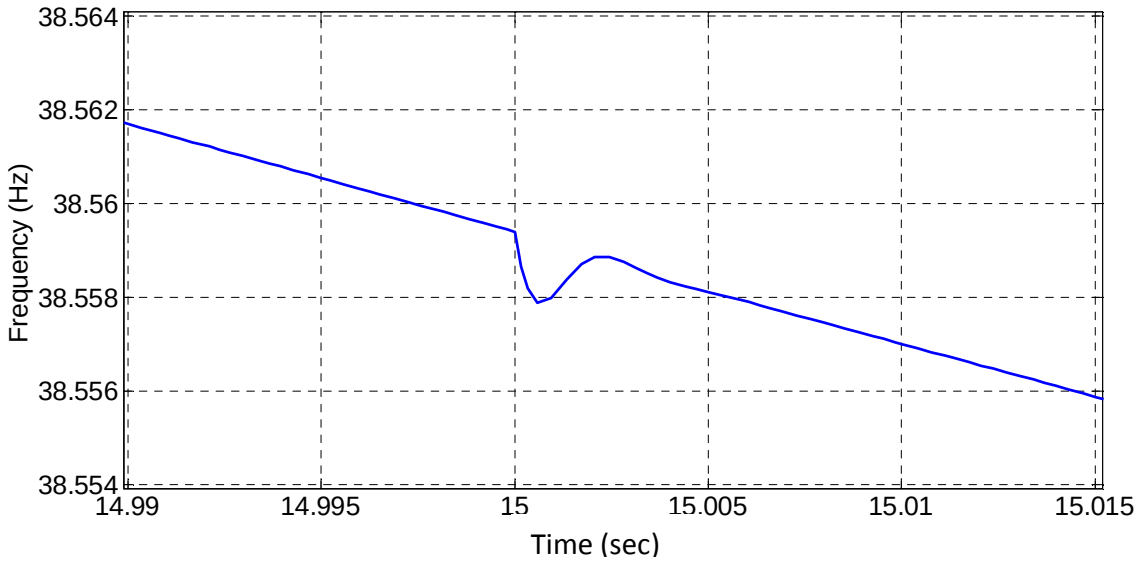

(*a*)

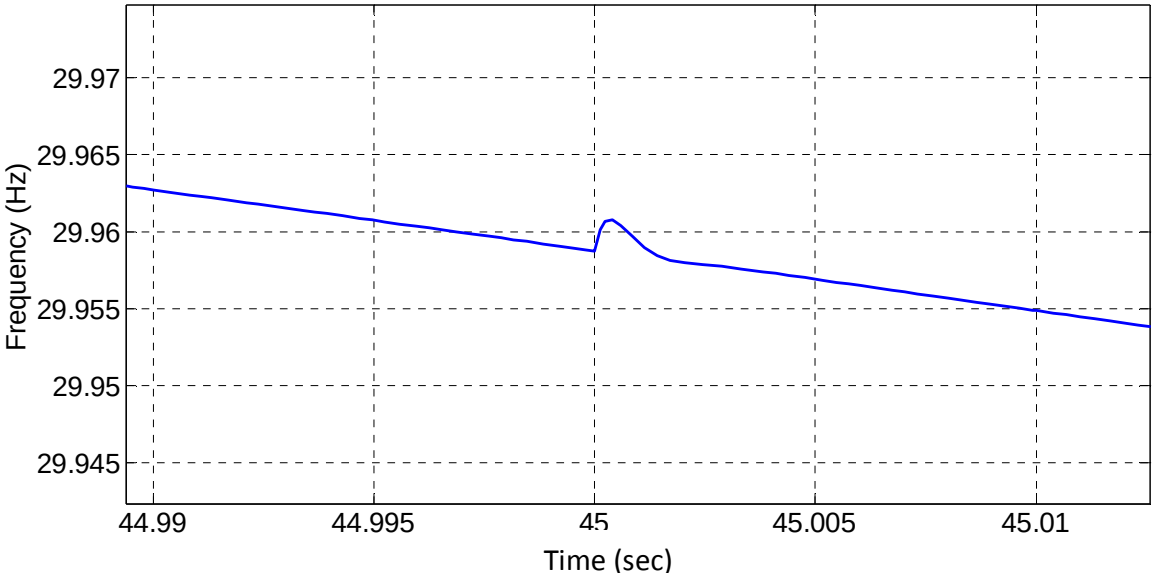

(*b*)

Figure 6.7 Motor excitation frequency at times: (*a*) 15 seconds and (*b*) 45 seconds.

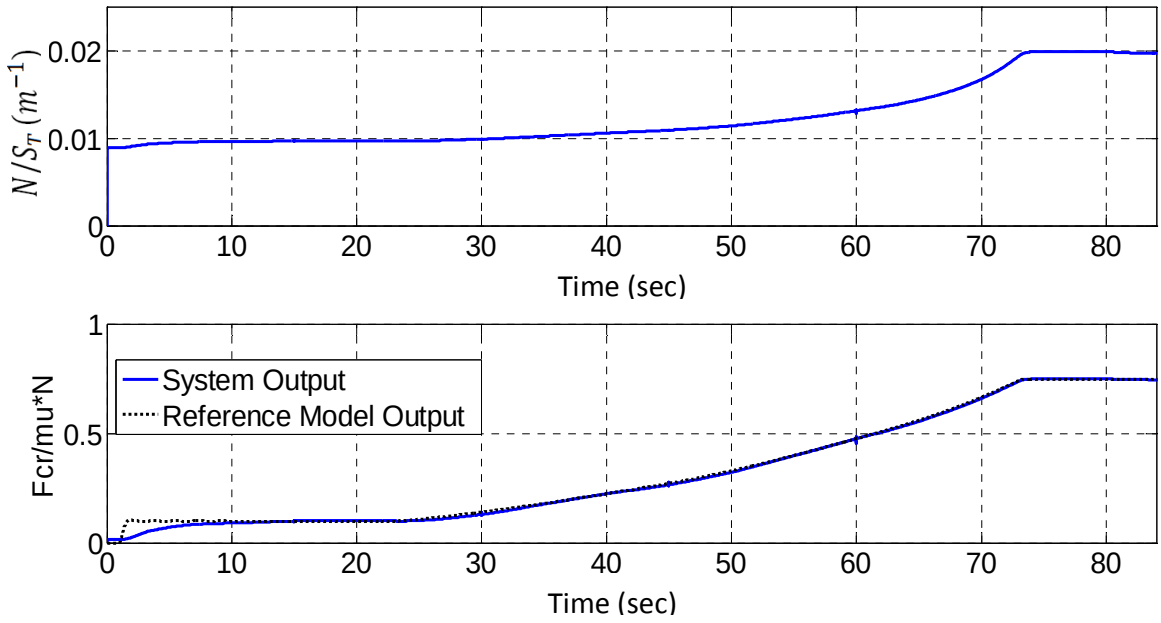

Figure 6.8 Train model outputs.

6.2.3 Creepage

Longitudinal creepage is suddenly reduced and increased by 20%, as illustrated in Figure 6.9. This means that the wheel rotational speed is suddenly changed at 15, 30, 45, and 60 seconds during the simulation. This may also represent sudden changes in the actual rolling radius of the wheel. Figure 6.10 shows that the motor frequency and braking torque are slightly affected by the sudden changes in longitudinal creepage. MRAC is able to accommodate these sudden changes, and the system goes back quickly to normal behavior in a few milliseconds as shown in Figure 6.11, where the motor frequency plot is magnified twice when sudden changes in traction occur. The outputs of the system are slightly affected by the sudden changes, as shown in Figure 6.12. The normalized creep forces, $F_{cr}/\mu N$, closely follow the reference model output.

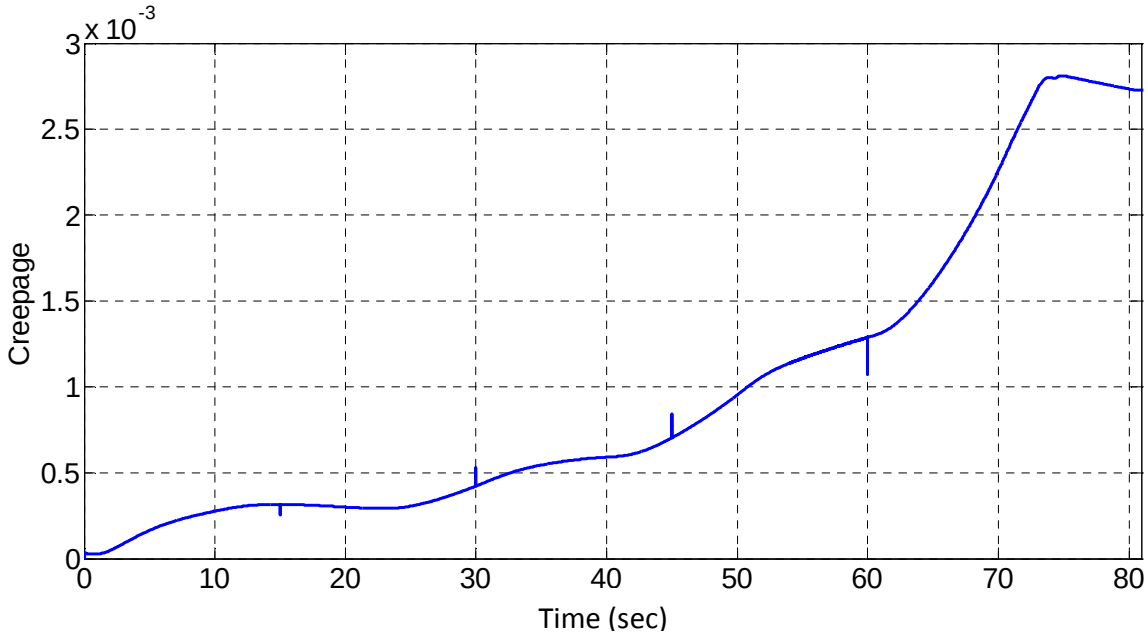

Figure 6.9 Sudden changes in the longitudinal creepage.

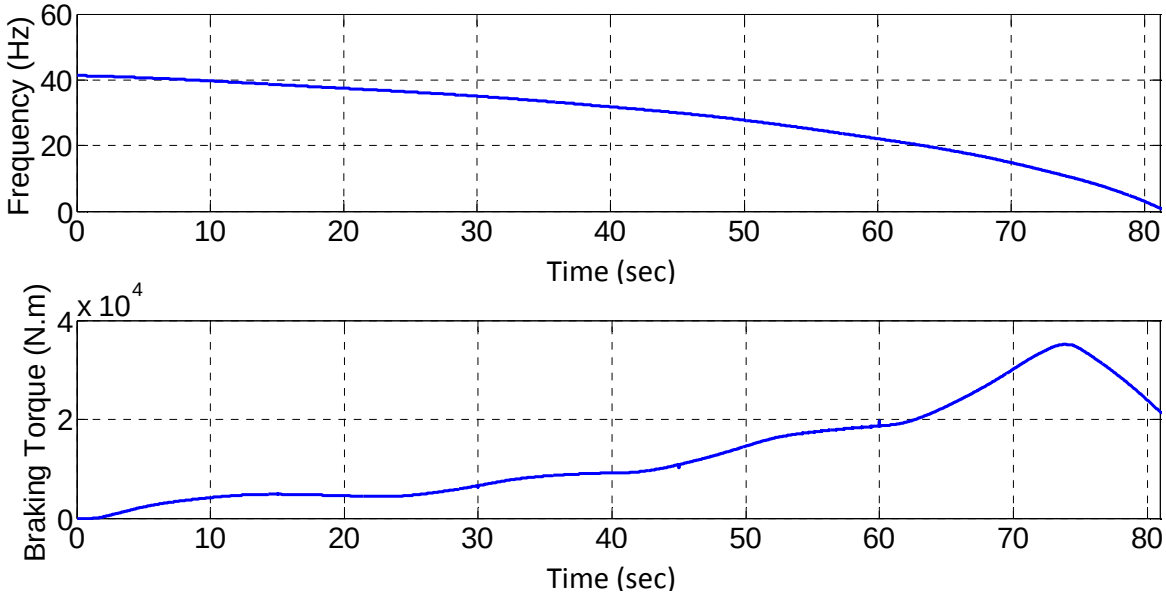

Figure 6.10 Motor excitation frequency and braking torque.

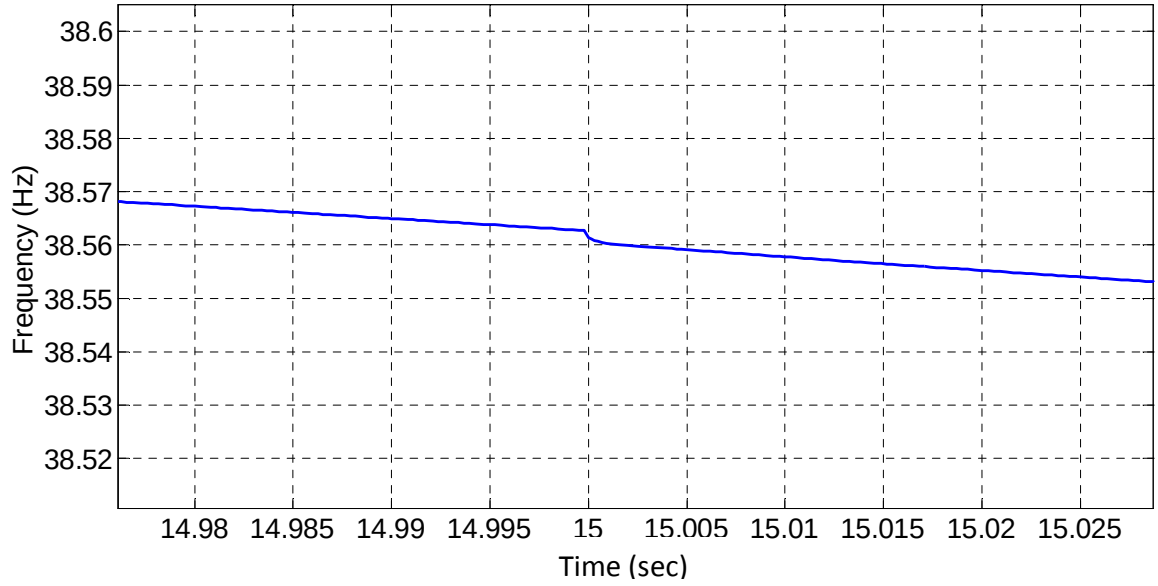

(*a*)

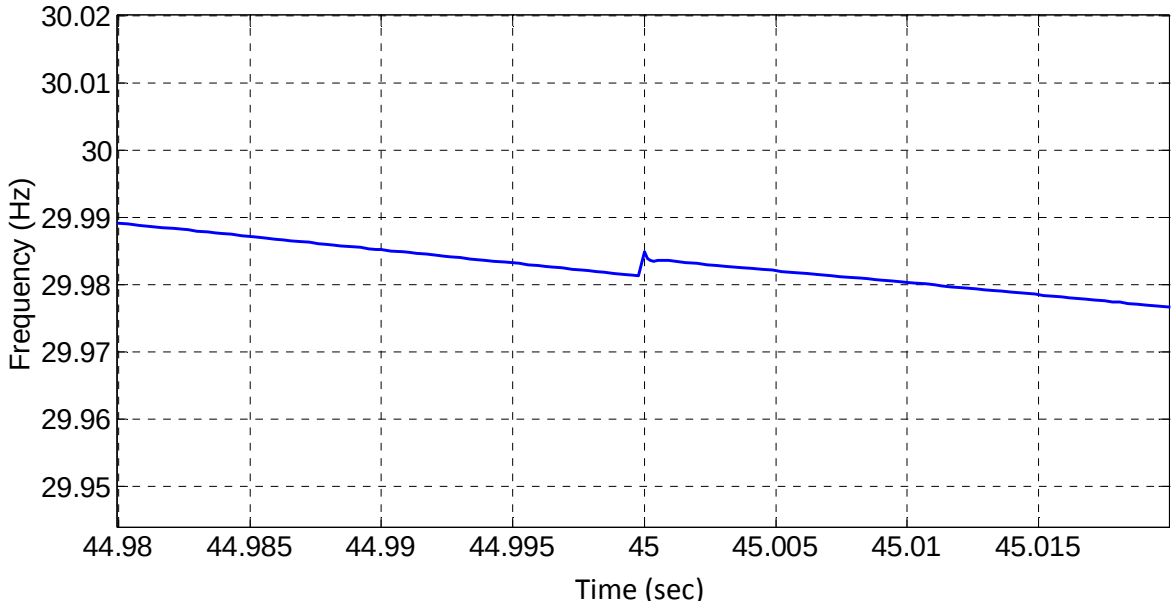

(*b*)

Figure 6.11 Motor excitation frequency at times: (*a*) 15 seconds and (*b*) 45 seconds.

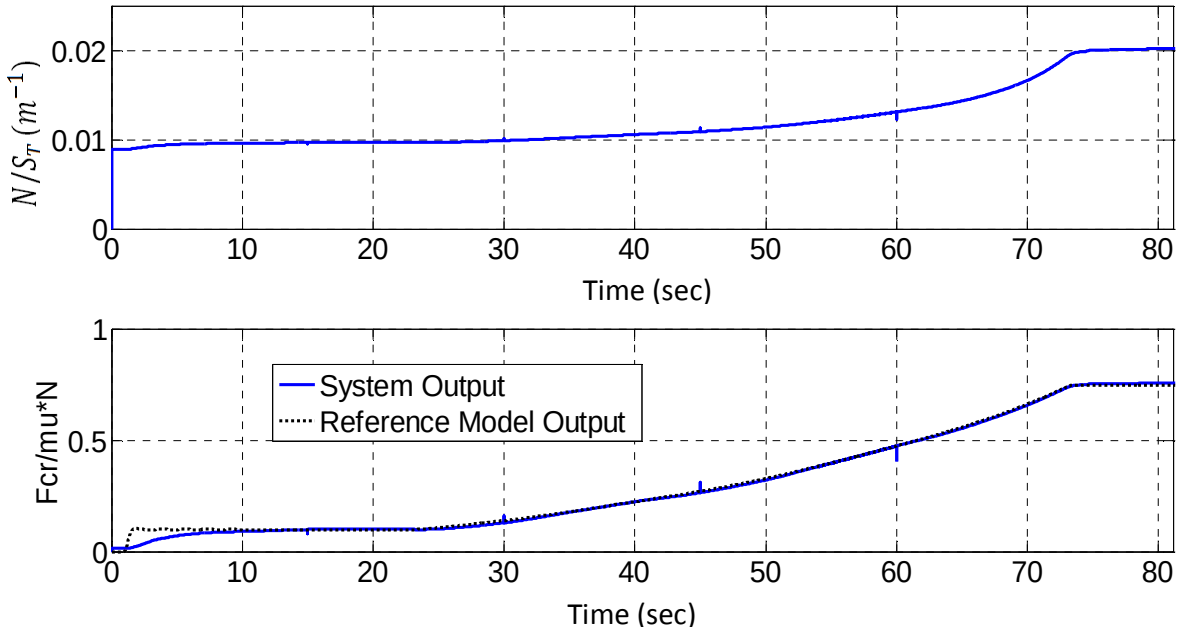

Figure 6.12 Train model outputs.

6.2.4 Wheel Normal Load

Similar to the earlier robustness evaluations, the wheel normal load is suddenly reduced and increased by 20%, as shown in Figure 6.13. In practice, the changes can be caused by track irregularities and suspension force variations. Figure 6.14 shows that the motor frequency and braking torque are slightly affected by the sudden changes in wheel normal load. MRAC is able to adjust to changes in less than one second, as shown in Figure 6.15. The motor frequency plot is magnified at two time positions when the sudden changes occur. The output of the system is slightly affected by the sudden changes as shown in Figure 6.16, and the normalized creep forces, $F_{cr}/\mu N$, closely follow the reference model output.

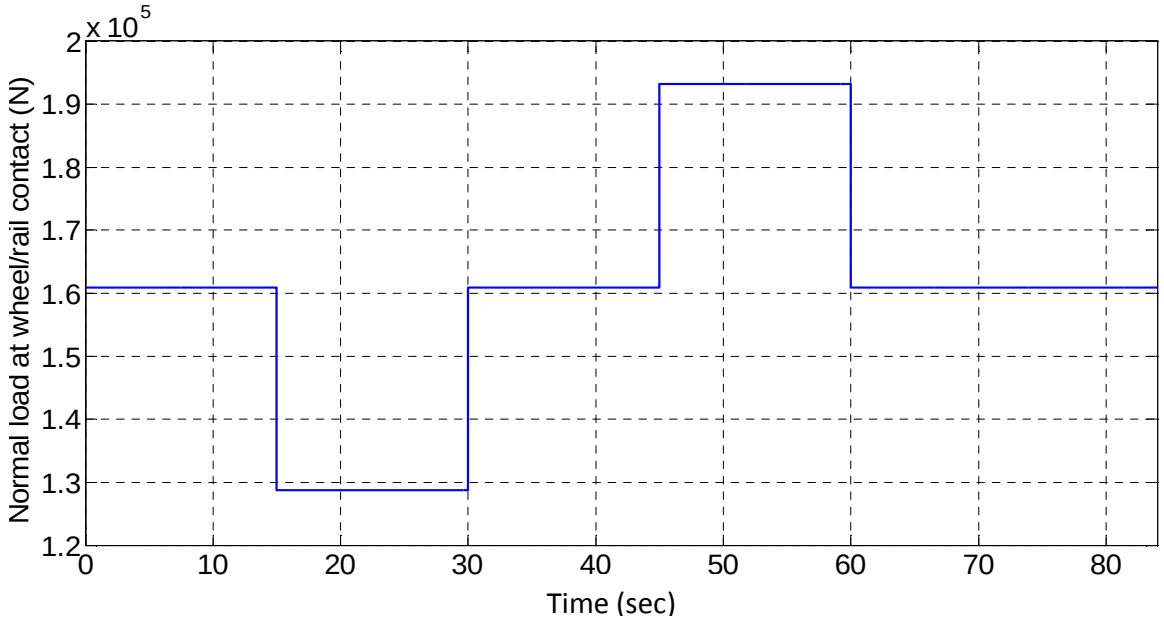

Figure 6.13 Sudden changes in the normal load at the wheel/rail contact.

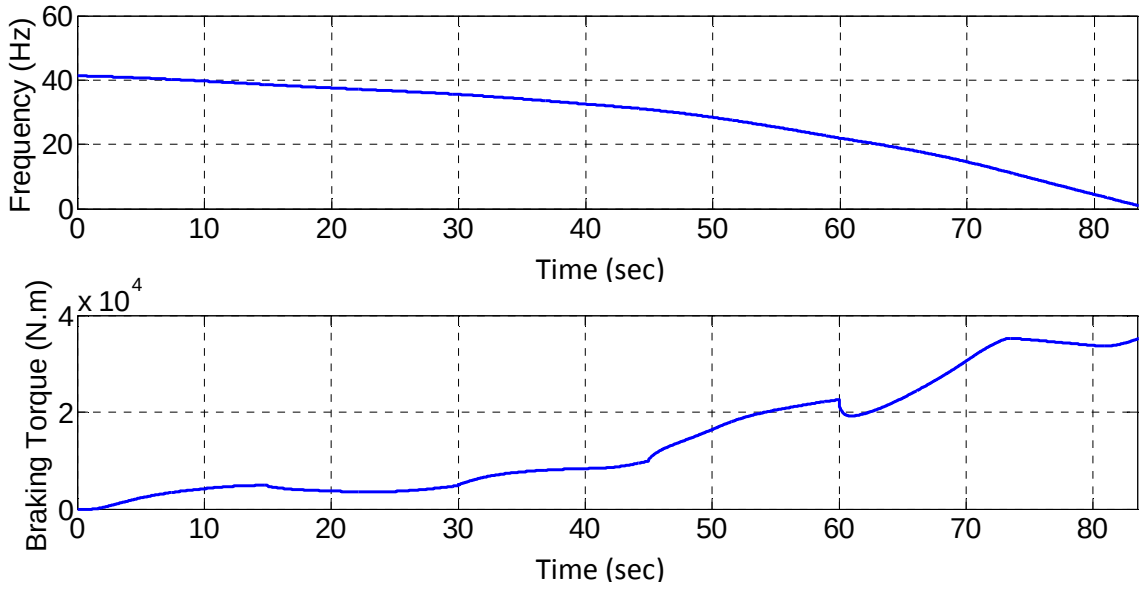

Figure 6.14 Motor excitation frequency and braking torque.

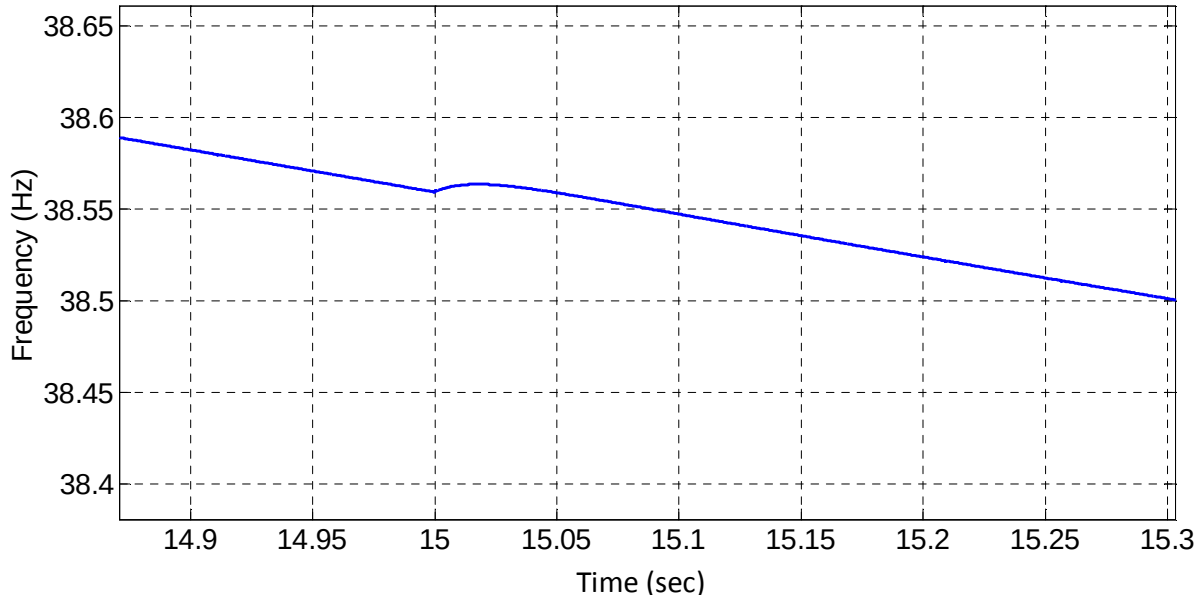

(*a*)

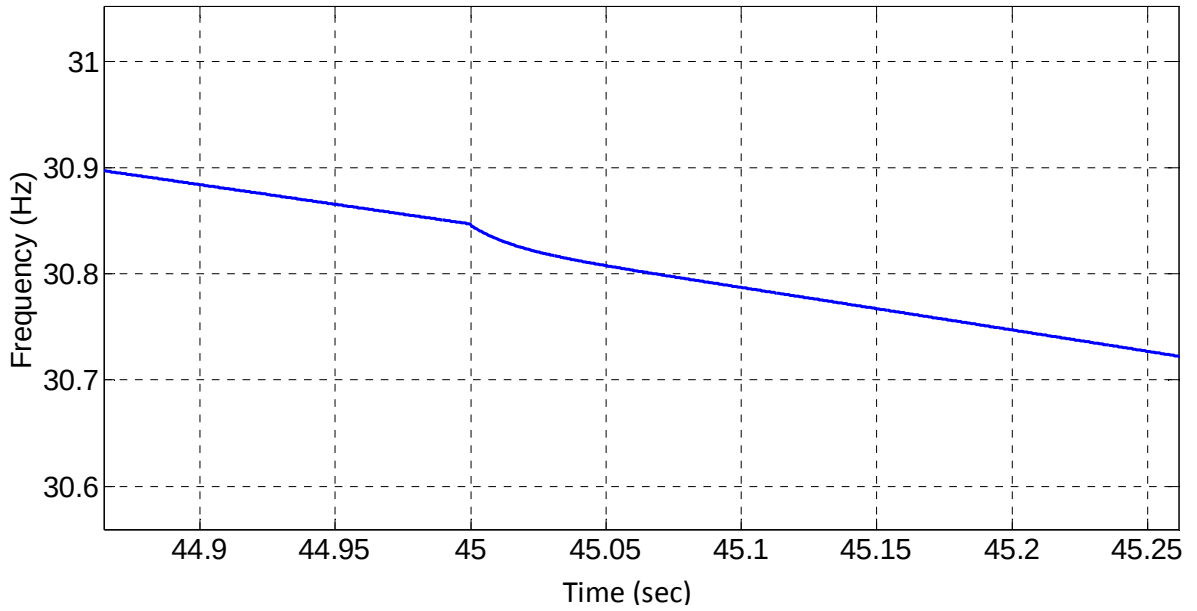

(*b*)

Figure 6.15 Motor excitation frequency at times: (*a*) 15 seconds and (*b*) 45 seconds.

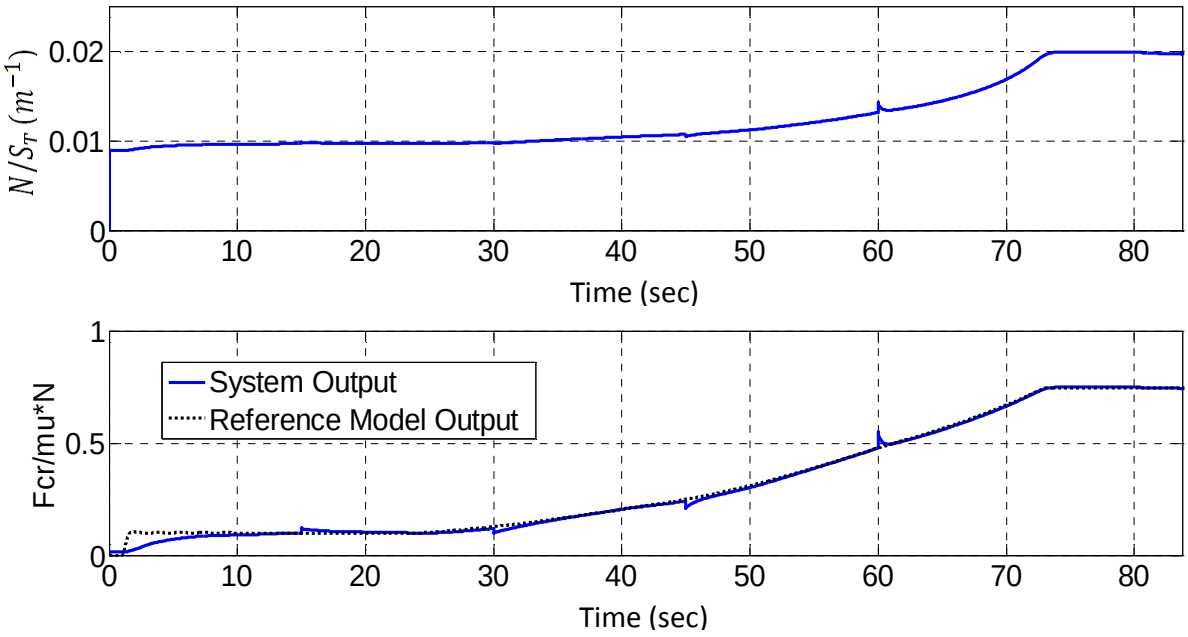

Figure 6.16 Train model outputs.

6.2.5 Braking Torque

The dynamic braking torque is suddenly reduced and increased by 20%, as shown in Figure 6.17, representing sudden changes in motor excitation frequency and motor torque. In addition, changes in track gauge can cause the wheels to run closer to the flange (larger wheel rolling radius), or farther from the flange (smaller wheel rolling radius), resulting in a decrease or increase in wheel rotational speed, respectively. This variation in track gauge may affect the motor braking torque since it depends on the speed slip ratio. The sudden changes are reflected in the rotational speed of the wheel as shown in Figure 6.18. MRAC is able to adapt to the changes in less than one second, and braking torque resumes normally. Figure 6.19 shows a magnified motor frequency plot at two time positions when the sudden changes occur. The system output is slightly affected by the changes, and the normalized creep forces, $F_{cr}/\mu N$, closely follow the reference model output, as shown in Figure 6.20.

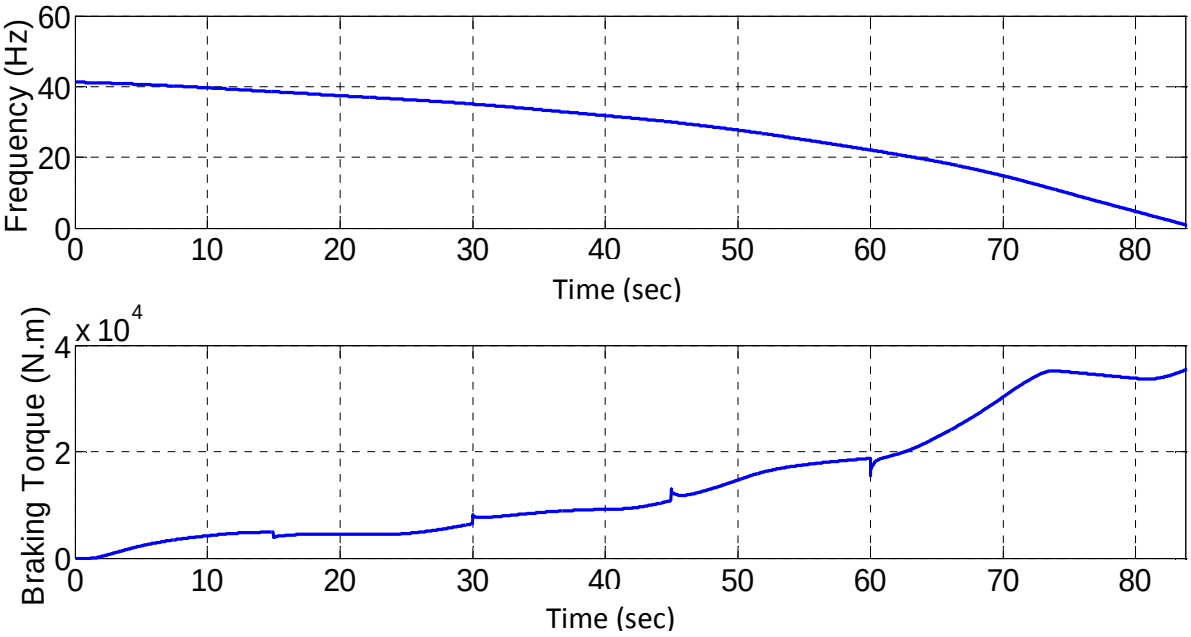

Figure 6.17 Motor excitation frequency and braking torque.

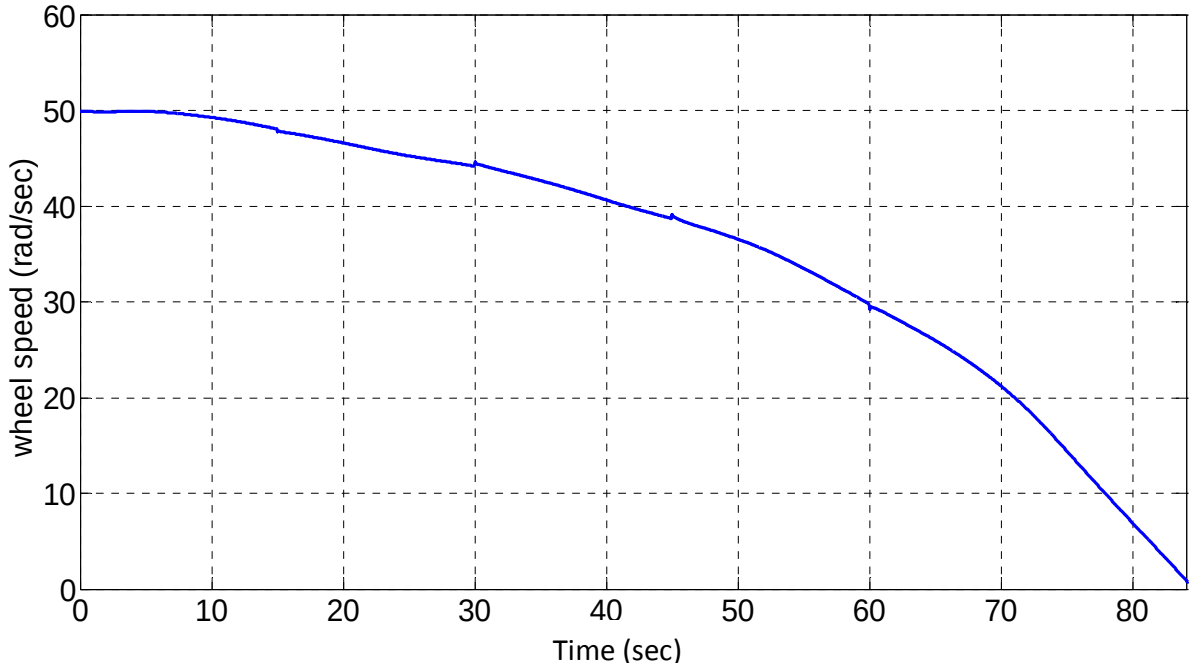

Figure 6.18 Wheel rotational speed versus time.

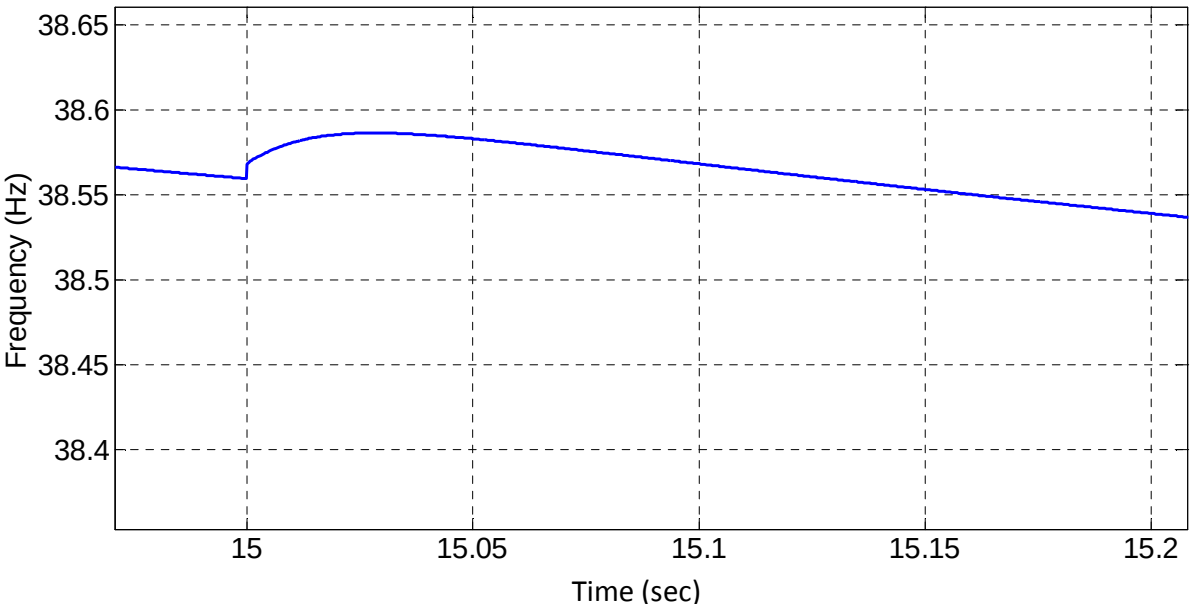

(*a*)

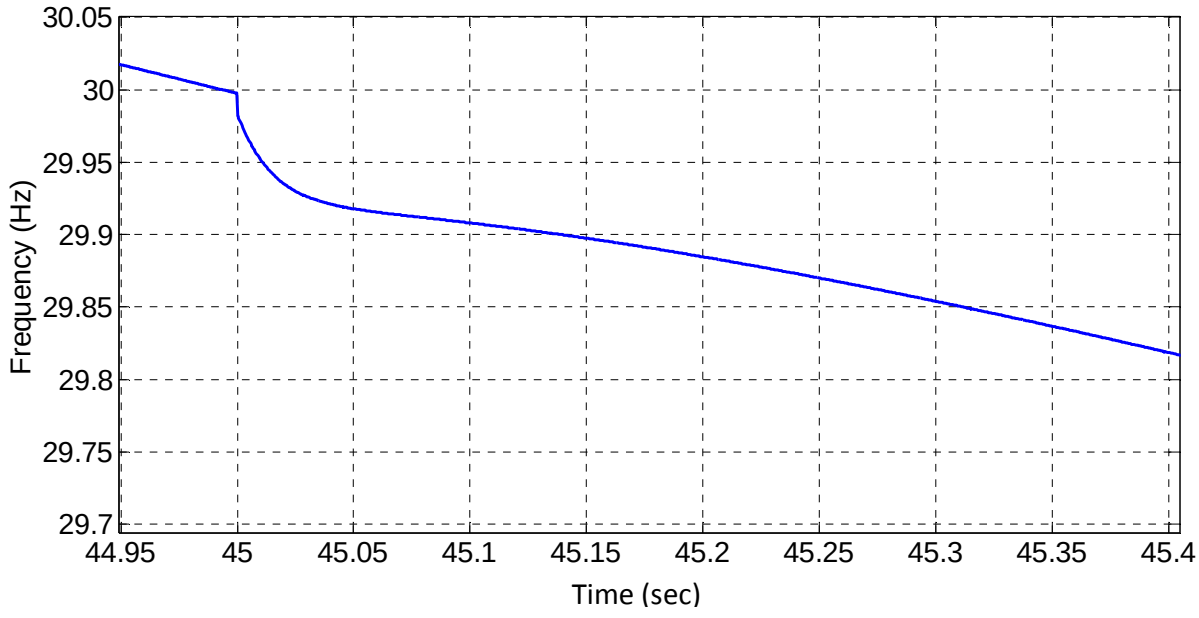

(*b*)

Figure 6.19 Motor excitation frequency at times: (*a*) 15 seconds and (*b*) 45 seconds.

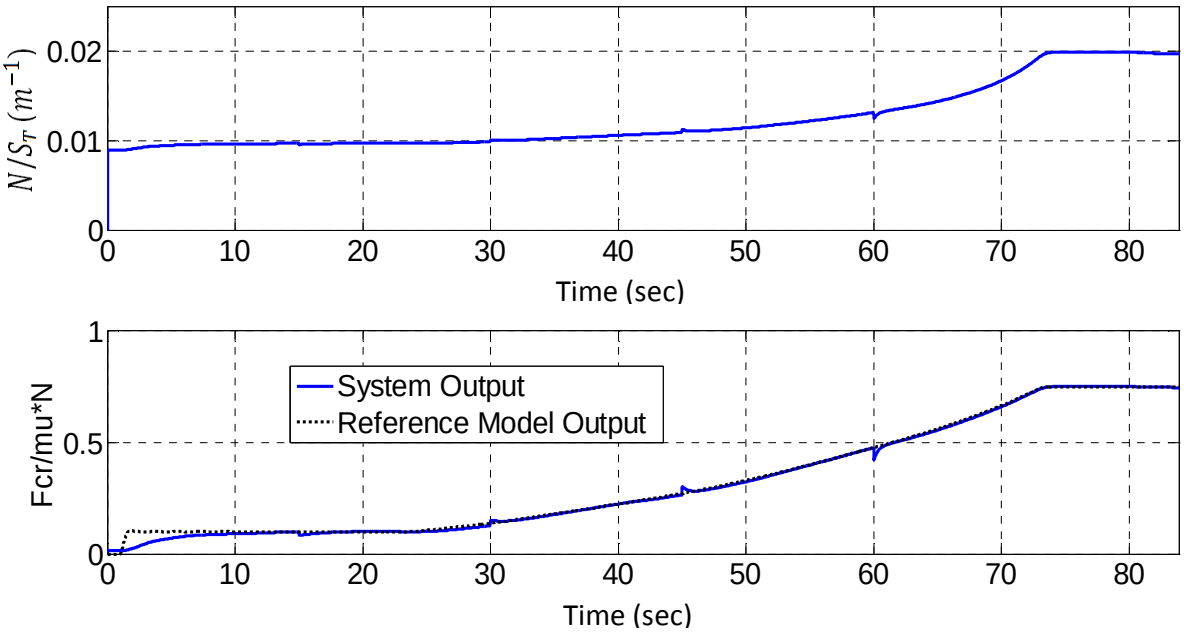

Figure 6.20 Train model outputs.

Chapter 7

Final Discussion and Conclusions

7.1 Summary

Longitudinal train dynamics were modeled using a multibody dynamics formulation, including train braking dynamics. A parametric study was performed to better understand how various elements affect the train braking distance. The application of Model Reference Adaptive Control (MRAC) for train dynamic braking was investigated, which may reduce train braking distance (and time to stop) by achieving maximum allowable dynamic braking while remaining within the maximum allowable adhesion and coupler forces. The MRAC system was developed to control the amount of current through the traction motors under various wheel/rail adhesion condition while braking. For DC traction motors, the MRAC system was used to control the current supplied to the traction motors. This motor current is directly proportional to the dynamic braking force. In addition, the MRAC system was also used to control the train speed by controlling the synchronous speed of the AC traction motors. The goal of both control systems of DC and AC traction motors was to maximize dynamic braking while avoiding wheel lockup and high coupler forces. The results indicated that the MRAC system significantly improves train braking while maintaining better wheel/rail adhesion and coupler dynamics during braking. Furthermore, the braking distance can be estimated when MRAC is used. The robustness of the MRAC system with respect to different parameters was investigated and the results showed an acceptable robust response behavior.

7.2 Final Discussion

In this study, the grade and curving resistances were not included in the simulations, because they depend on the track geometry. If the track geometry is known, track resistance can easily be implemented in the model. The developed train model can be used for any number of railcars. Based on the developed dynamic model, the train braking distance can be estimated if the weights, initial speed, number of railcars, wheel/rail condition, and braking forces are known. The MRAC enables estimation of the train braking distance, thereby using maximum track line

capacity while avoiding train-to-train accidents. According to this study, the critical factors that contributes to increasing train braking distance is poor wheel/rail adhesion. If wheel/rail adhesion conditions are different on both rails (known as *split* μ), then the effective adhesion coefficient is the average of the two rails. The proposed control method can accommodate split μ conditions since the established parameter, normal-load-torque-creep ratio (N/S_T), is independent of the adhesion conditions.

There are different ways of improving wheel/rail adhesion. The most common way to enhance adhesion is to apply sand at the leading edge of the wheel-rail interface in order to increase the coefficient of friction at the wheel. During autumn, accumulation of dirt and pressed leaves on top of the rail can also significantly reduce wheel-rail adhesion. High-pressure water-jet blasting with sand, or high-power laser burning is often used to remove any hard layer buildup on the rail [4].

MRAC can adapt to changes in locomotive operating conditions, available dynamic braking effort, coupler design, and available wheel/rail adhesion conditions in real time to provide better braking performance than non-adaptive controllers, such as PID control. Implementing the MRAC allows the braking output to closely follow the designed reference model. Consequently, estimating train braking distance can be a priori, enabling trains equipped with PTC to be spaced closer together with more confidence in order to maximize track capacity.

7.3 Conclusions

The main findings of this study are:

1. Model Reference Adaptive Control (MRAC) can easily be implemented in locomotives to significantly improve dynamic braking in terms of taking advantage of the maximum available braking from the traction motors without exceeding wheel-rail adhesion (locking up the wheels) and allowable coupler forces.
2. A parametric study of a train shows that MRAC can be used to accurately determine, a priori, train braking distance under different operating conditions, such as weights, initial speed, and number of railcars, thereby, enabling closer train spacing for applications such as Positive Train Control (PTC).

3. The established relationship between the normalized creep force and normal-load-torque-creep ratio (N/S_T) is independent of the wheel-rail adhesion condition, which is usually unknown. This indicates that the performance of MRAC is independent of any changes in wheel load that may be occur because of weight transfer during braking or fuel weight reduction.
4. MRAC is able to perform robustly in cases where the train parameters cannot be estimated accurately, or are changed during train operation by events such as a change in the wheel-rail traction condition, wheel load, motor torque, or wheel diameter.

Future work is suggested to include improvement of the reference model design depending on actual field data, as well as to include experiments to verify the proposed control method. Additionally, it may include comparison with other adaptive control methods.

References

[1] Garg, V. K., & Dukkipati, R. V. *Dynamics of Railway Vehicle Systems*. Ontario, Canada: Academic Press, 1984.

[2] Dukkipati, R. V. *Vehicle Dynamics*. Boca Raton, Florida: CRC Press, 2000.

[3] Lee, H. A Polynomial Chaos Approach for Stochastic Modeling of Dynamic Wheel-Rail Friction. PhD. Thesis. Virginia Tech, USA. Aug. 2010.

[4] Iwnicki, S. *Handbook of Railway Vehicle Dynamics*. Boca Raton, Florida: Taylor & Francis Group, 2006.

[5] Railway Technical Web Pages, http://www.railway-technical.com/

[6] Manual for Railway Engineering, America Railway Engineering and Maintenance-of-Way Association (AREMA), *Systems Management*. Vol.4, 2010.

[7] Astrom, K. J. & Wittenmark, B. *Adaptive Control*. Ontario, Canada: Addison-Wesley Publishing Company, Inc. Second Edition, 1995.

[8] Model Reference Adaptive Control. Drexel University tutorials, http://www.pages.drexel.edu/~kws23/tutorials/MRAC/MRAC.html

[9] Federal Railroad Administration Website, http://www.fra.dot.gov.

[10] Polach, O., "Creep Forces in Simulations of Traction Vehicles Running on Adhesion Limit," Elsevier, *Wear* 258, 2005, pp. 992 – 1000.

[11] Chen, H., Ishida, M., Namura, A., Baek, K. S., Nakahara, T., Leban, B. & Pau, M. "Estimation of wheel/rail adhesion coefficient under wet condition with measured boundary friction coefficient and real contact area." Elsevier, *Wear*, 2010.10.022.

[12] Zhang, W., Chen, J., Wu, X. & Jin, X. "Wheel/rail adhesion and analysis by using full scale roller rig." Elsevier, Wear 253, 2002, pp. 82 – 88.

[13] Kung, C., Kim, H., Kim, M. & Goo, B., "Simulations on Creep Forces Acting on the Wheel of a Rolling Stock." International Conference on Control, Automation and Systems, Seoul, Korea. Oct. 14 – 17, 2008.

[14] Piechowiak, T., "Verification of Pneumatic Railway Brake Models." *Vehicle System Dynamics*, Vol. 48, No. 3, Mar. 2010, pp. 283 – 299.

[15] Piechowiak, T., "Pneumatic Train Brake Simulation Method." *Vehicle System Dynamics*, Vol. 47, No. 12, Dec. 2009, pp. 1473 – 1492.

[16] Dhanasekar, M., Cole, C. & Handoko, Y. "Experimental evaluation of the braking torque on bogie dynamics." *International Journal of Heavy Vehicle Systems*, Vol. 14, No. 3, 2007.

[17] Pugi, L., Fioravanti, D., & Rindi, A. "Modelling the longitudinal dynamics of long freight trains during the braking phase." 12th IFToMM World Congress, France. Jun. 18 – 21, 2007.

[18] Zhang, Z. & Dhanasekar, M. "Dynamics of railway wagons subjected to braking/traction torque." *Vehicle System Dynamics*, Vol. 47, No. 3, Mar. 2009, pp. 285 – 307.

[19] Ansari, M., Esmailzadeh, E., & Younesian, D. "Longitudinal dynamics of freight trains." *International Journal of Heavy Vehicle Systems*, Vol. 16, Nos. 1/2, 2009.

[20] Barney, D., Haley, D., & Nikandros, G. "Calculating Train Braking Distance." The 6th Australian Workshop on Safety Critical Systems and Software, Brisbane. *Conferences in Research and Practice in Information Technology*, 2001, Vol. 3.

[21] Kang, C. "Analysis of the Braking System of the Korean High-Speed Train Using Real-Time Simulations." *Journal of Mechanical Science and Technology*. 2007, Vol. 21, pp. 1048-1057.

[22] Kang, C., Kim, H., Kim, M., & Goo, B. C. "Real-time simulations of a railroad brake system using a dSPACE board." ICROS-SICE International Joint Conference. Japan, Aug 18-21, 2009, pp. 4073- 4078.

[23] Esfandiari, R. S. & Lu, B. *Modeling and Analysis of Dynamic Systems*. Boca Raton, FL: CRC Press, Taylor & Francis Group, 2010.

[24] Ahmad, H. & Ahmadian, M. "Train Braking Distance Estimation Under Different Operating Conditions." Proceedings of the ASME Rail Transportation Division Fall Conference, Minneapolis, Minnesota. Sep. 21 – 22, 2011.

[25] Ahmad, H. & Ahmadian, M. "Model Reference Adaptive Control of Train Dynamic Braking." Proceedings of the ASME Joint Rail Conference, Philadelphia, PA, Apr. 17-19, 2012.

[26] Association of American Railroads website, www.aar.org.

[27] Fitzgerald, A. E., Kingsley, C. Jr., & Ummans, S. D. *Electric Machinery*. Sixth Edition. New York, NY: McGraw-Hill Higher Education, 2003.

[28] "Diesel-Electric Locomotive SD90MAC with Three-Phase Drive." Siemens, Technical Information.

[29] Zhao, Y., Liang, B. & Iwnicki, S. "Estimation of Friction Coefficient Between Wheel and Rail Surface using Traction Motor Behaviour." 25th International Congress on Condition Monitoring and Diagnostic Engineering. *Journal of Physics*: Conference Series 364, 2012.

[30] Gaspar, P., Szabo, Z. & Bokor, J. "Observer Based Estimation of the Wheel-Rail Friction Coefficient." Proceedings of the 2006 IEEE International Conference on Control Applications. Munich, Germany, Oct. 4 – 6, 2006.

[31] Adrian, C., Corneliu, A., & Mercea, B. "The Simulation of the Adaptive Systems Using the MIT Rule." The 10th International Conference on Mathematical Methods and Computational Techniques in Electrical Engineering. Sofia, Bulgaria, May 2 – 4, 2008.

[32] Xiong, A. & Yongkun, F. "Application of PID Controller using MRAC Techniques for Control of the DC Electromotor Drive." Proceedings of the IEEE International Conference on Mechatronics and Automation. Harbin, China, Aug. 5 – 8, 2007.

[33] Nankyo, M., Ishihara, T., & Inooka, H. "Feedback Control of Braking Deceleration on Railway Vehicle." *Journal of Dynamic Systems, Measurement, and Control*, Jun. 2006, Vol. 128, pp. 244 – 250.

[34] Zhiwu, H., Haitao, T. & Yanfen, F. "The Longitudinal Dynamics of Heavy-haul Trains in the Asynchronous Brake Control System." 2010 International Conference on Measuring Technology and Mechatronics Automation. Changsha City, China, 2010, pp. 900 – 903.

[35] Wu, M., Chen, T., Lu, Y. & Cheng, M. "Modeling and Simulation of Deceleration-oriented Braking Control on Freight Train." *Applied Mechanics and Material*. Trans Tech Publications. 2011, Vols. 88-89, pp. 77 – 81.

[36] Yamazaki, H., Nagai, M. & Kamada, T. "A Study of Adhesion Force Model for Wheel Slip Prevention Control." *JSME International Journal*, 2004, Series C, Vol. 47, No. 2., pp. 496 – 501.

[37] Yamazaki, H., Karino, Y., Nagai, M., & Kamada, T. “Wheel Slip Prevention Control by Sliding Mode Control for Railway Vehicle (Experiments Using Real Size Test Equipment).” Proceedings of the 2005 IEEE/ASME International Conference on Advanced Intelligent Mechatronics, Monterey, California, USA, Jul. 24 – 28, 2005.

[38] Cheok, A. D. & Shiomi, S. “Combined Heuristic Knowledge and Limited Measurement Based Fuzzy Logic Antiskid Control for Railway Application.” IEEE *Transaction on Systems, Man, and Cybernetics*, Part C, 2000, Vol. 30, No. 4, pp. 557 – 568.

[39] Gissl, C., Glasl, M., & Ove, A. “Adhesion Control in Railroad Traction.” *Elektrotechnik und Informationstechnik*, Springer-Verlag, Austria, 2004, Vol. 121, Isse. 7 – 8, pp. 263 – 267.

[40] Matsumoto, Y., Eguchi, N., & Kawamura, A. “Novel Re-adhesion Control for Train Traction Systems of the “Shinkansen” with the Estimation of Wheel-to-Rail Adhesive Force.” The 27th Annual Conference of the IEEE Industrial Electronics Society. 2001, Vol. 2, pp. 1207 – 1212.

[41] Liudvinavičius, L. & Bureika, G. “Theoretical and Practical Perspectives of Diesel Locomotive with DC Traction Motors Wheel-Sets’ Slipping and Sliding Control.” Taylor & Francis Group. 2011, Vol. 26(4), pp. 335 – 343.

[42] Hwang, D., Kim, M., Park, D., Kim, Y. & Kim, D. “Re-adhesion Control for High-Speed Electric Railway with Parallel Motor Control System.” Proceedings of 5th International Conference, ISIE, IEEE International Symposium, 2001, Vol. 2, pp. 1024 – 1029.

[43] Hwang, D., Kim, M., Park, D., Kim, Y. & Lee, J. “Hybrid Re-adhesion Control Method for Traction System of High-Speed Railway.” Proceedings of 5th International Conference, ISIE, IEEE International Symposium, Aug. 2001, Vol. 2, pp. 739 – 742.

[44] Watanabe, T. & Yamashita, M. “Basic Study of Anti-slip Control without Speed Sensor for Multiple Drive of Electric Railway Vehicles.” Proceedings of Power Conversion Conference, Osaka, IEEE 2002, Vol. 3, pp. 1026 – 1032.

[45] Mei, T., Yu, J. & Wilson, D. “A Mechatronic Approach for Effective Wheel Slip Control in Railway Traction.” Proceedings of the Institute of Mechanical Engineers, *Journal of Rail and Rapid Transit*, 2009, Vol. 223, Part. F, pp. 295 – 304.

[46] Mei, T., Yu, J. & Wilson, D. “Re-Adhesion Control Based on Wheelset Dynamics in Railway Traction System.” In the UKACC2006, Glasgow, UK, 2006.

[47] Wei, K., Zhao, J., You, X. & Zheng, T. “Development of a Slip and Slide Simulator for Electric Locomotive Based on Inverter-Controlled Induction Motor.” Industrial Electronics and Applications, ICIEA, 4th IEEE Conference. May 25 – 27, 2009.

[48] Shabana, A. & Sany, J. “A Survey of Rail Vehicle Track Simulations and Flexible Multibody Dynamics.” *Journal of Nonlinear Dynamics*, 2001, Vol. 26, pp. 170 – 210.

Appendices

1. Main Simulink block diagram for the parametric study.

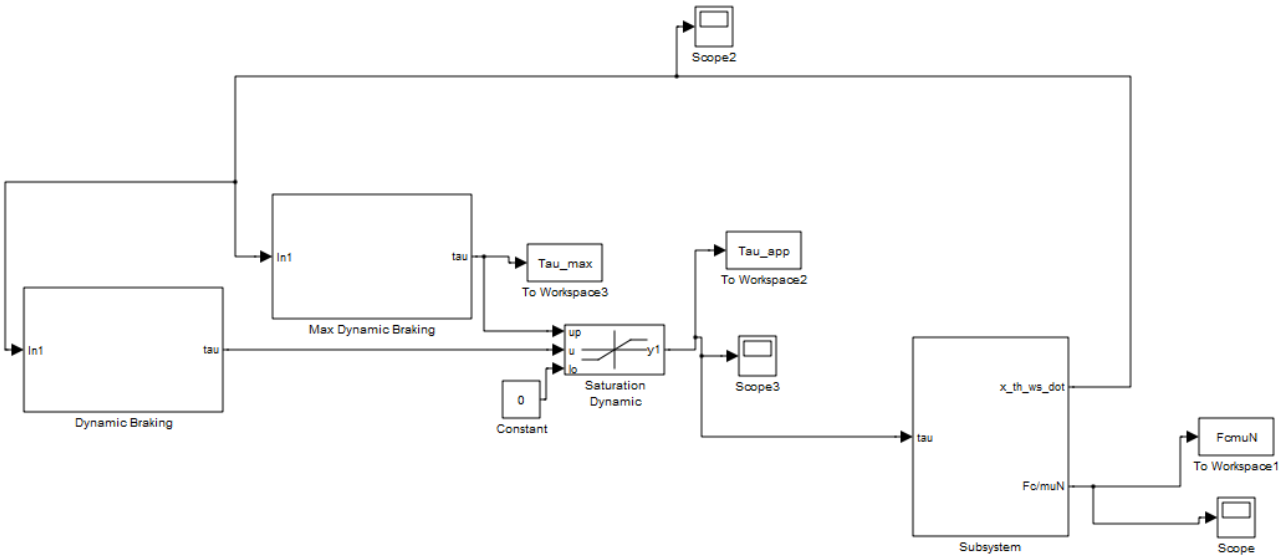

2. Simulink block diagram for 3-car model in the parametric study.

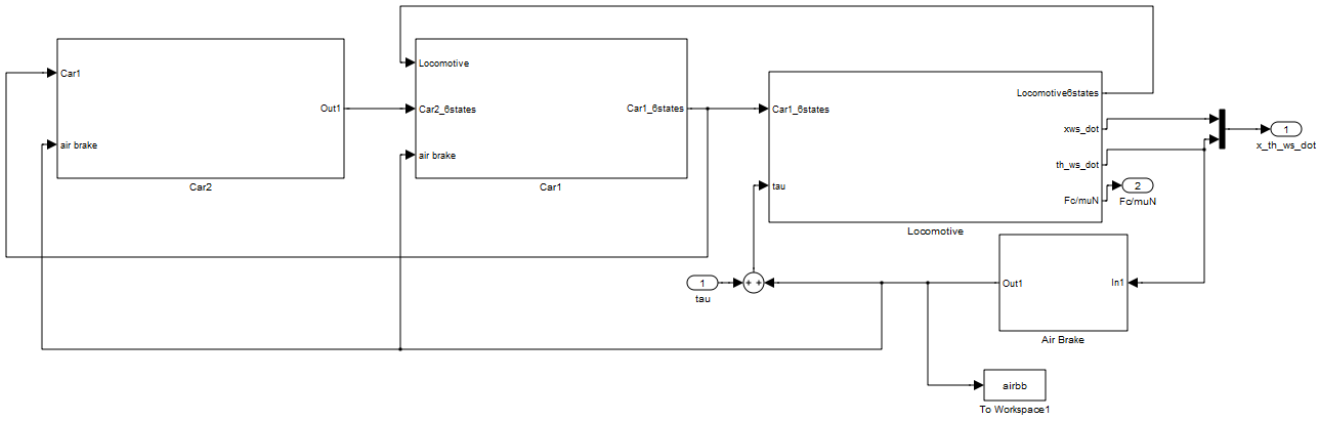

3. Simulink locomotive block diagram (carbody, front & rear bogies, and six wheelsets).

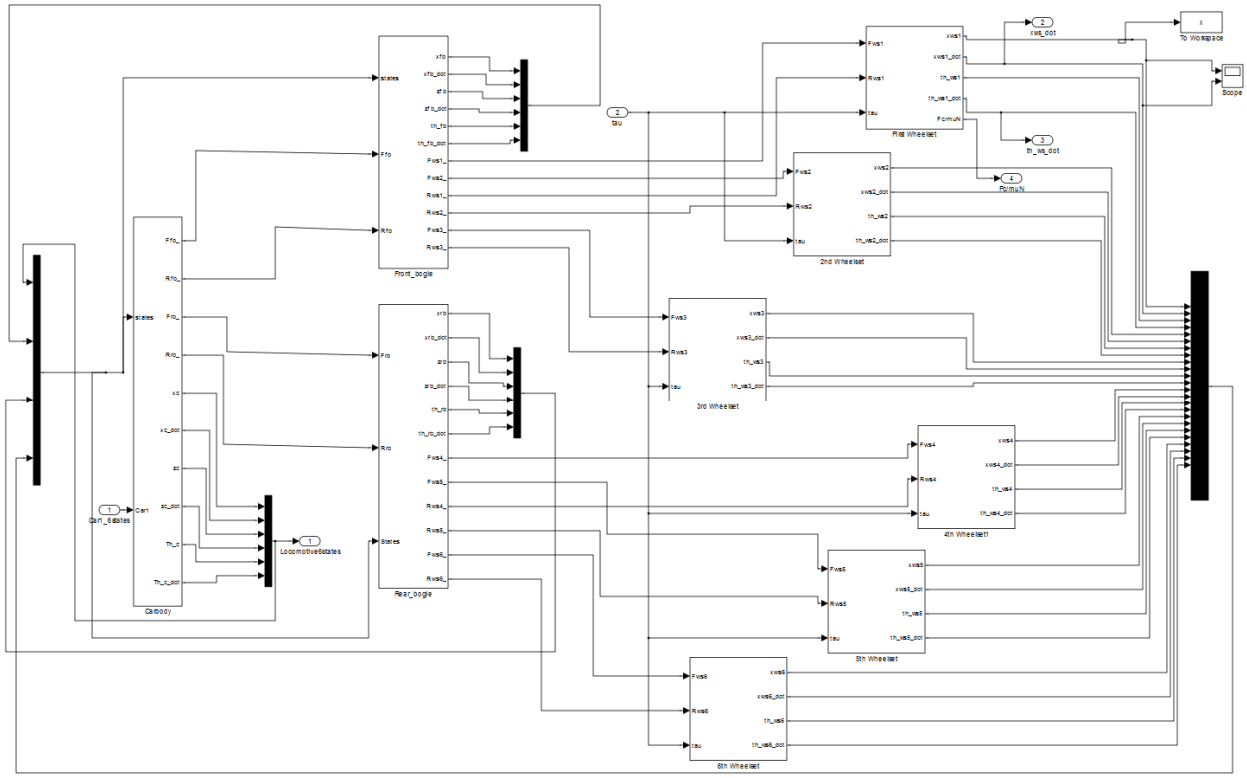

4. Simulink block diagram of the powered wheelset at the locomotive.

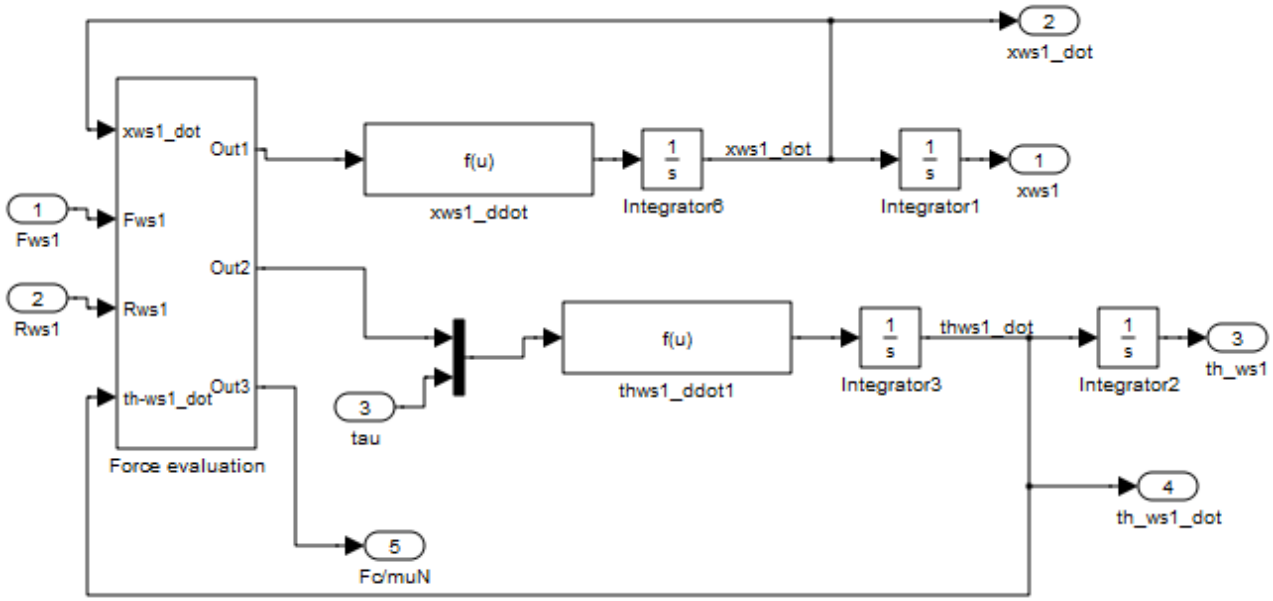

5. Simulink block diagram of the force evaluation at the powered wheelset.

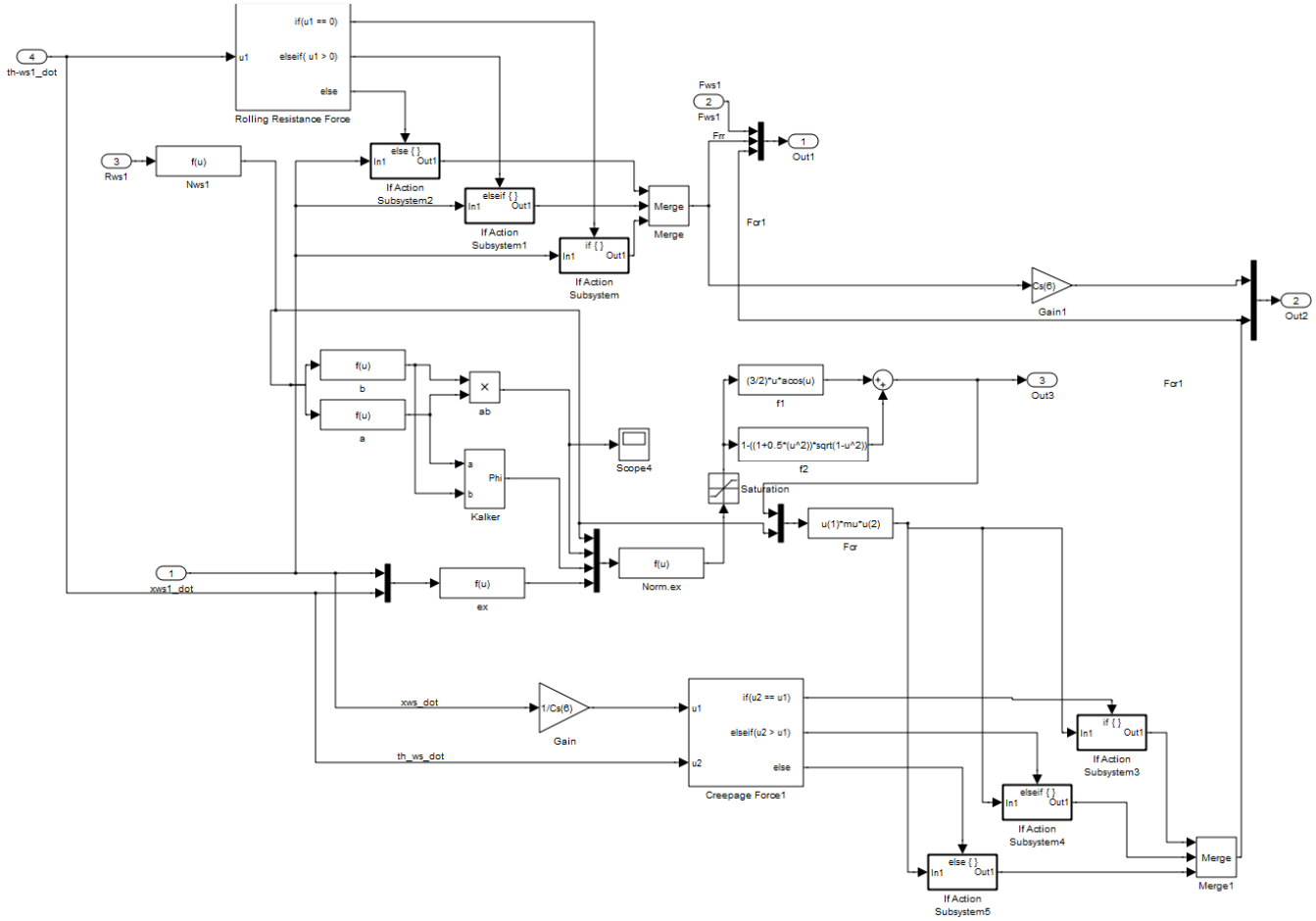

6. Main Simulink block diagram of the MRAC system with DC traction motors.

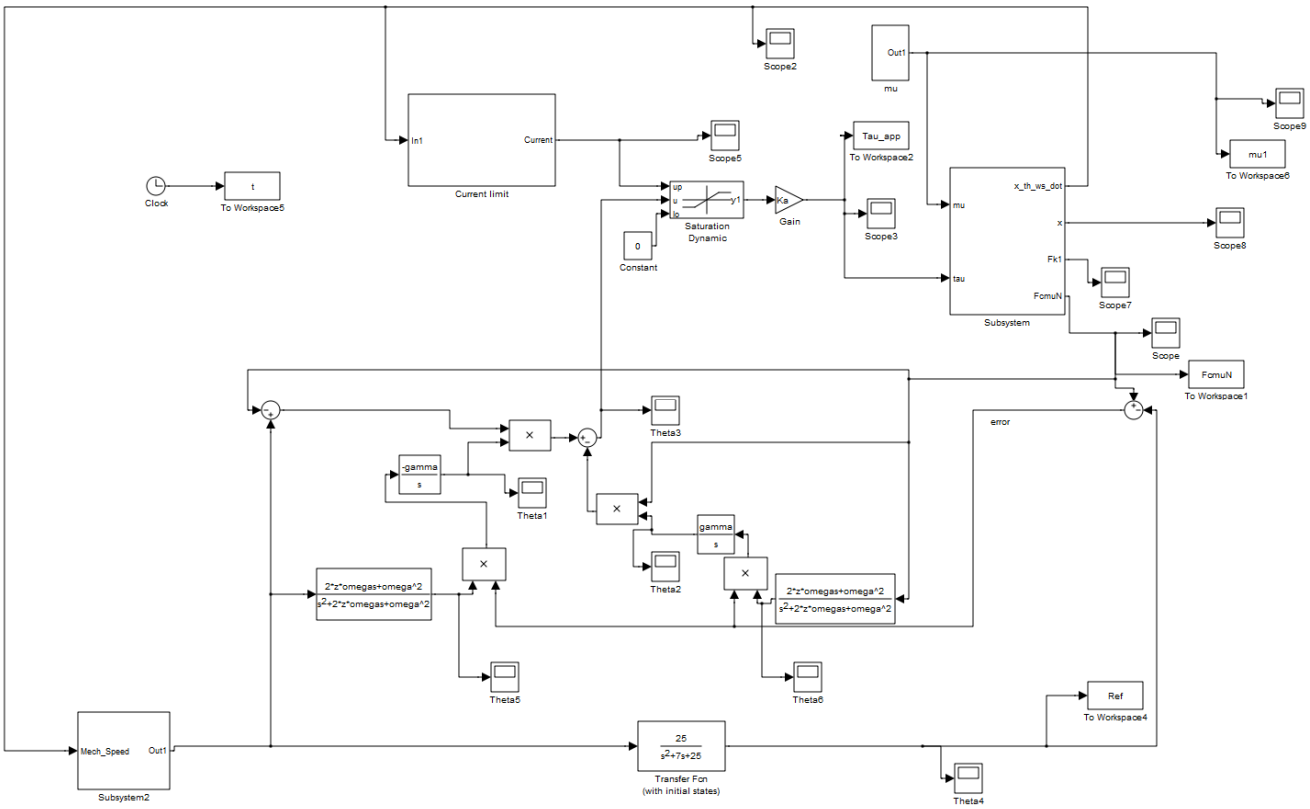

7. Main Simulink block diagram of the MRAC system with AC traction motors.